Spring 2021

Analysis of turbulence model uncertainty for canonical flow problems including shock wave boundary layer interaction simulations

Aaron James Erb

Department: Mechanical and Aerospace Engineering

ANALYSIS OF TURBULENCE MODEL UNCERTAINTY FOR CANONICAL FLOW PROBLEMS INCLUDING SHOCK WAVE BOUNDARY LAYER INTERACTION SIMULATIONS

by

AARON JAMES ERB

A DISSERTATION

Presented to the Graduate Faculty of the

MISSOURI UNIVERSITY OF SCIENCE AND TECHNOLOGY

In Partial Fulfillment of the Requirements for the Degree

DOCTOR OF PHILOSOPHY

in

AEROSPACE ENGINEERING

2021

Approved by:

Dr. Serhat Hosder, Advisor
Dr. David Riggins
Dr. Kakkattukuzhy Isaac
Dr. Daoru Han
Dr. Leifur Leifsson

ABSTRACT

The purpose of this research is to present results of an uncertainty and sensitivity analysis study of commonly used turbulence models in Reynolds-Averaged Navier-Stokes (RANS) codes due to the epistemic uncertainty in closure coefficients for a set of turbulence model validation cases that represent the structure of several canonical flow problems. The study focuses on the analysis of a 2D zero pressure gradient flat plate, a 2D wall mounted hump, and an axisymmetric shock wave boundary layer interaction, all of which are well documented on the NASA Langley Research Center Turbulence Modeling Resource website. The Spalart-Allmaras (SA), the Wilcox (2006) k-ω (W2006), and the Menter Shear-Stress Transport (SST) turbulence models are considered in the stochastic analyses of these flow problems and the FUN3D Code of NASA was utilized as the flow solver. The uncertainty quantification approach involves stochastic expansions based on non-intrusive polynomial chaos to efficiently propagate the uncertainty. Sensitivity analysis is performed with Sobol indices to rank the relative contribution of each closure coefficient to the total uncertainty for several output flow quantities. The results generalize a set of closure coefficients which have been identified as contributing most to the various output uncertainty for the problems considered in this study. Mainly, the SA turbulence model is most sensitive to the uncertainties in the diffusion constant, the log layer calibration constant, and the turbulent destruction constant. The predictive capability of the W2006 model is most sensitive to the uncertainties in a dissipation rate constant, the shear stress limiter, and a turbulence-kinetic energy constant. Likewise, the SST turbulence model was found to be most sensitive to a diffusion constants, the log layer calibration constant, and the shear stress limiter. The results of this study are expected to guide the efforts on improving the accuracy of RANS predictions through validation experiments and data-driven modeling approaches for various flow problems by identifying the coefficients for refinement.

ACKNOWLEDGMENTS

To Dr. Hosder, thank you for all of your guidance and encouragement through my graduate career. You taught me so much and I value everything you've done for me. You would often provide me with a necessary push when I needed it and I will always be grateful for your steadfast dedication to my education and career.

I would also like to thank my committee members, Dr. David Riggins, Dr. Kakkattukuzhy Isaac, Dr. Daoru Han, and Dr. Leifur Leifsson for providing their time, expertise, and dedication during my graduate career. I especially thank Dr. Riggins and Dr. Isaac. I enjoyed every class I took with you and I continue to benefit from your teaching.

I am thankful for the overall education provided to me by the Missouri University of Science and Technology. I am grateful for the Missouri S&T Chancellor's Fellowship Program for providing me with the funding support to pursue my graduate research.

I would also like to thank the NASA Grant NNX14AN17A for additional funding.

To my labmates, John, Andrew B., Aslihan, Mario, Martin, and Andrew H. Thank you for your camaraderie as fellow labmates and as helpful distractions from school.

Furthermore, I would like to thank the NASA Pathways program and specifically Dr. Tom West. I've benefited greatly under your mentorship and will always be grateful for the opportunities you helped provide.

To my mom and dad, Celeste and Jim. Thank you for your unwavering support throughout my life. I know I could be a handful at times so I'm eternally thankful for always being there and for everything you've done for me. Dad, I wish you were still here but I know you would be proud of me.

And finally to my wife, Elcke. Thank you for always believing in me and encouraging me to do my best, both professionally and otherwise. You are my best friend and I look forward to a fun and happy future with you.

TABLE OF CONTENTS

Page

LIST OF ILLUSTRATIONS

LIST OF TABLES

Table Page

NOMENCLATURE

Symbol	Description
	Roman
C_{D_p}	Drag coefficient due to pressure
$C_{D_{sf}}$	Drag coefficient due to skin friction
C_f	Skin friction coefficient
D	Total variance
d	Distance to wall
M	Mach number
n	Number of uncertain variables
n_p	Oversampling ratio
N_s	Total number of samples
P	Pressure
p	Order of response surface polynomial
Q	Heat flux
Re	Reynolds number
S	Coordinate measured along the surface
$S_{i_1 \ldots i_s}$	Sobol indices

$\hat{\nu}$	Transport quantity for SA model
f_w	SA model parameter
T	Temperature
u	Velocity
U_∞	Freestream velocity
u^+	Dimensionless log-law velocity
$\boldsymbol{x}$	Deterministic vector
y	Spatial variable
y^+	Dimensionless log-law wall coordinate

Greek

α^*	Stochastic response function
α_i	Deterministic component of α^*
χ	Ratio of turbulent eddy to kinematic
ϵ	Epistemic bound
μ	Molecular dynamic viscosity
μ_t	Turbulent eddy viscosity
ν	Molecular kinematic viscosity
ν_t	Turbulent kinematic viscosity
Ω	Vorticity magnitude

Ψ_i	Random variable basis functions of α^*
ρ	Density
θ	Variable of integration
$\boldsymbol{\xi}$	Random variable vector

Subscripts

c	Chord
∞	Freestream
L	Unit length
ref	Reference
t	Total
w	Value at the wall

Turbulence model closure coefficients

c_{b1}, c_{b2}, c_{t3} c_{t4}, c_{v1}, c_{w2} c_{w3}, κ, σ	Spalart-Allmaras closure coefficients
β^*, β^*/β_0 C_{lim}, κ σ_k, σ_ω	Wilcox-2006 k-ω closure coefficients
a_1, β^*, β^*/β_1 β^*/β_2, κ, σ_{k1} σ_{k2}, $\sigma_{\omega1}$, $\sigma_{\omega2}$	Menter SST closure coefficients

1. INTRODUCTION

The purpose of the study presented in this dissertation is to present and analyze the results of an uncertainty and sensitivity analysis study of commonly used turbulence models in Reynolds-Averaged Navier-Stokes (RANS) codes due to the epistemic uncertainty in closure coefficients for a set of turbulence model validation cases that represent the structure of several canonical flow problems. This introductory section is organized as follows: Section 1.1 present the some background information behind this study and includes the motivation as to why this study was conducted. Section 1.2 presents the objectives of this dissertation in terms of the cases studied, the turbulence models used in the study, and the contributions that this study will provide to the community at large. Section 1.3 provides a review of the current literature based on previous work with regard to uncertainty quantification (UQ) in the field of computational fluid dynamic (CFD) simulations and includes several studies of turbulence modeling UQ. Finally, Section 1.4 provides the reader with an outline of this dissertation.

1.1. MOTIVATION

Turbulence is still an unsolved problem in the study of fluid mechanics. The highly complex turbulent flow is uncertain in nature and thereby poses a difficult problem to solve. As such, comprehensive understanding of the phenomena has yet to be developed. Turbulence modelers have worked diligently in the creation of realizable predictive methods through the use of CFD; however, a lack of the complete understanding of turbulence has forced these modelers to use dimensional analysis in an effort to close this open problem. Resulting from the dimensional analysis, groups of constants, called closure coefficients, are introduced to balance the model equations. The values of these constants are gleaned from a combination of heuristic methods and empirical studies. Due to their formation, current

turbulence models used in RANS simulations and used in sub-grid scale modeling of Large-Eddy Simulations are not guaranteed to perform well for any arbitrary flow, and can often fail in flow regimes significantly dissimilar to the experiment used in their formulation.

To help facilitate the advancement of turbulence model development, implementation, application, and validation/verification, the NASA Turbulence Modeling Resource (TMR) website [1] was developed to provide a centralized location to document RANS turbulence models. The objective of this website is to provide CFD developers accurate and current information regarding commonly used RANS turbulence models and a strategy to verify correct implementation of the models. Additionally, the TMR provides a validation process to compare CFD results against data in an effort to establish a model's ability to reproduce important flow physics whereby a set of test cases are provided that incorporate fundamental fluid dynamics phenomena.

For the particular case of the the shock wave boundary layer interaction problem presented in this dissertation, documents reveal that mitigating the effects of uncertainty in hypersonic flow is a goal of the NASA Hypersonics Project [2]. The assessment of state-of-the-art CFD code uncertainties for the prediction shock wave turbulent boundary layer interactions on a compression corner is of primary concern. Under hypersonic flight conditions, when a turbulent boundary layer encounters a compression corner, unfavorable processes such as flow separation and localized pressure and heat spikes, can occur. Additionally, different flow physics are activated as functions of total enthalpy, atmospheric composition, vehicle size, and vehicle shape [3]. The methods in which a specific turbulence model treats these phenomenon introduce uncertainties into the predictions. Quantities of interest to a hypersonic vehicle designer, such as vehicle drag, control surface effectiveness, and inlet mass capture are significantly impacted as a direct result of model predictions and associated uncertainties. Understanding the uncertainties from the model predictions can lead to more robust designs that are not susceptible to these impacts.

1.2. OBJECTIVES AND CONTRIBUTIONS

The purpose of this dissertation is to present uncertainty quantification and sensitivity analyses of commonly used turbulence models in RANS codes due to the epistemic uncertainty in closure coefficients for a number of validation cases documented on the TMR website [1]. These cases include a 2D Zero Pressure Gradient Flat Plate (2DZP), a 2D NASA Wall-Mounted Hump Separated Flow (2DWMH), and an Axisymmetric Shock Wave Boundary Layer Interaction at $M = 7$ (ASWBLI). Three turbulence models are considered in this study: the Spalart-Allmaras One Equation Model (SA) [4], the Wilcox (2006) κ-ω Two-Equation Model (W2006) [5], and the Menter Shear-Stress Transport Two-Equation Model (SST) [6]. This research also includes the refinement and implementation of stochastic expansion techniques based on polynomial chaos for efficient uncertainty propagation and sensitivity metrics derived from non-linear global sensitivity analysis based on Sobol indices.

It is well-known that RANS models are not designed for strongly separated flows including shock induced separation. In fact, turbulence models in RANS simulations are derived and calibrated mostly for low speed attached and mildly separated flows. Because of this fact, this inherent deficiency would fall under the category of model form uncertainty and is not the subject of this dissertation. Despite this innate deficiency, RANS simulations are still used as one of the main analysis and design tools in aerospace industry for various flow regimes and problems due to its relatively low computational cost compared to Large-Eddy Simulations (LES) and Direct Numerical Simulations (DNS). This study aims to support the validation and improvement of RANS turbulence models by identifying a set of closure coefficients for each model that contribute to the output uncertainty most for different flow problems so that the future validation and experimental efforts can be prioritized to focus on the improvement of the accuracy of these coefficients (i.e., reduction of the epistemic uncertainty of the closure coefficients). The sensitivity information provided in this study will help the design of the validation experiments that will focus on the refinement of

the values of coefficients with the highest contribution to the output uncertainty. The main contribution of the current work to the literature is that this is the first to study and generalize the impact of the uncertainty in turbulence model closure coefficients on various quantities of interest (QoIs) for a set of important canonical flow problems with different flow structures. The objective is to investigate and identify a common set of coefficients for each turbulence model which contribute most to the uncertainty for all the flow problems studied towards making general conclusions and suggestions for potential refinement and improvement of the turbulence models. Results of the current study are also compared with previous studies, when appropriate, to generalize the important findings.

1.3. LITERATURE REVIEW

During the engineering design process, it is imperative to understand the uncertainty embedded within. Whenever a mathematical model is employed to simulate an aerodynamic system, nearly all parameters that are investigated are assumed to be in their idealized form. However, despite these idealized assumptions, the real world application of these studies comprise many uncertainties. In a collaborative effort between NASA, Boeing, and others, Slotnick et al. [7] document the results of a study to address a strategic plan required by NASA's Revolutionary Computational Aerosciences (RCA) program in the area of CFD. One of the main takeaways from this study is their acknowledgment that the predictive capabilities of CFD to accurately predict turbulent flows in regions of high separability is severely limited. Their vision for the CFD of the future should include physics-based predictive modeling of turbulence and should have methods in place to manage errors and uncertainties from all possible sources, including epistemic uncertainties that arise due to lack of knowledge.

To reduce the computational expense of performing an uncertainty quantification and sensitivity analysis of real world engineering problems, an efficient method is required. As such, a number of previous studies on uncertainty quantification [8, 9, 10, 11] concentrated

on developing the process of nonintrusive uncertainty quantification to efficiently propagate uncertainties though the system. The current work employs these nonintrusive methods and applies them to a set of canonical flow simulations that represent real world aerodynamic applications.

Previous studies on turbulence model closure coefficient uncertainty focused on transonic wall-bounded flow problems and hypersonic internal and external flow. Schaefer et al. [12] investigated turbulence model closure coefficient uncertainty for a transonic bump problem and an RAE 2822 airfoil. Di Stefano et al. [13] investigated turbulence model closure coefficients for a scramjet isolator and scramjet strut flow field. Erb and Hosder [14] performed an in-depth anaylsis of the Axisymmetric Shock Wave Boundary Layer Interaction problem where the flow field QoIs included density, Mach number, and pressure, while surface and point QoIs included pressure, heat flux, and skin friction distribution and separation bubble size and drag coefficient. These previous work employed stochastic expansions to efficiently propagate the uncertainty. Similarly, some aerothermodynamic studies employed the use of stochastic expansions to perform a uncertainty quantification and sensitivity analyses. In particular, West et al. [15, 16] studied the uncertainty in convective and radiative heating in hypersonic entry flows. Brune et al. [17, 18] investigated the uncertainty in the hypersonic flow field, fluid structure interaction, and the thermal response of a flexible thermal protection system due to uncertainties in flowfield modeling and TPS properties. Godfrey and Cliff [19] used the sensitivity-equation method to quantify the sensitivities of the Baldwin–Lomax algebraic, the Spalart–Allmaras one-equation, and the Wilcox k-ω two-equation turbulence models due to closure coefficients but they stopped short of quantifying the uncertainty in the results. Han and Hosder [20] performed a mixed uncertainty quantification for the 2DWMH with flow control where they included a scaling factor on the turbulent eddy viscosity definition in the Spalart–Allmaras model.

Turgeon et al. [21, 22] developed a general formulation of the continuous sensitivity equations for use in an uncertainty study of the closure coefficients in the k-ϵ turbulence model with wall functions on a flat plate simulation. In their study, the uncertainty intervals over which the turbulence model coefficients were arbitrarily taken. Platteeuw et al. [23] builds upon this work by utilizing experimental data and direct numerical simulation results to obtain physically accurate input distributions for the different coefficients. They then use the probabilistic collocation method to quantify the uncertainty in the solution due to uncertainties in the standard k-ϵ turbulence model closure coefficients for a flat plate test case. Further investigation into the k-ϵ turbulence model with wall functions was carried out by Dunn et al. [24] where they used the Latin hypercube sampling technique to propagate distributions of the closure coefficients from estimates obtained from experimental data of a backward-facing step from Pope [25]. Margheri et al. [26] gathered large amounts of of experimental and numerical data in an effort to characterize the closure coefficient distributions of the Launder–Sharma low-Reynolds number k-ϵ and Wilcox k-ω models. They show that uncertainties in the experimental data or simulated flow properties leads to uncertainties in these RANS model coefficients. Xiao and Cinnella [27] recently published a review paper where they examine both the parametric and structural uncertainties in turbulence models by investigating the fundamentals of uncertainty propagation and Bayesian inference as they pertain to RANS turbulence model uncertainty quantification.

A number of previous studies have investigated the turbulence model uncertainties in the particular cases of hypersonic shock wave and turbulent boundary layer interactions. Holden et al. [28] documented a series of experimental studies aimed at assessing the efficacy of CFD codes for shock wave turbulent boundary layer interactions using cone/flare and cylinder/flare configurations in high Reynolds number hypersonic flow. They found agreement between the CFD and the cone/flare configuration only after modifying the stress-limiter coefficient in the shear stress production equation for the SST turbulence model. DeBonis et al. [29], presented a turbulence model comparison from a workshop

focused on CFD predictions of oblique shocks impinging on a turbulent boundary layer. They noted that because RANS turbulence models are developed and adapted for well-behaved boundary layers and shear layers, their predictive capabilities for the complex flow associated with shock boundary layer interactions is unclear and should be the focus of further research. Gnoffo et al. [3] presented work they conducted as part of the NASA Fundamental Aeronautics Program in the Hypersonics Project where they assessed the model form uncertainty of several popular turbulence models. Their study was conducted on a 2D compression corner configuration at Mach 7 and 14. Three ramp angles were investigated: a 5.5° ramp which was intended to not induce separation, and 30° and 35° ramps that were designed to induce separation and engage the more complicated flow physics. Georgiadis et al. [30] found that the turbulent Prandlt number can have significant effect on the post-compression corner heating for all turbulence models they considered but could not define a single value for their high Mach number case. While these past studies provide significant insight on a model-to-model uncertainty assessment, what is lacking is a thorough investigation into the model parameters themselves. The current study aims to provide this by investigating the uncertainty within each model by treating the turbulence model closure coefficients as uncertain parameters in rigorous uncertainty and sensitivity analyses. The results are then compared with previous studies when appropriate.

1.4. OUTLINE

This dissertation is organized as follows: In Section 2, an overview of the test cases included in this study are presented. Section 3 provides a brief description of the flow solver used in this study as well as the three turbulence models; including a description of closure coefficients for each model. In Section 4, the uncertainty quantification (UQ) and sensitivity analysis methodologies are presented. In Section 5, the results of the UQ study

is discussed along with a comparison to previous UQ work focusing on relevant turbulence model closure coefficient uncertainty problems to generalize the findings of the current study. Finally, in Section 6, major conclusions of the study are presented.

2. CASE OVERVIEW

This section outlines the flow cases selected for this study. All cases are taken from the NASA TMR [1] where the applicable boundary conditions are available as well as a series of refined grids. Section 2.1 discusses the 2D Zero Pressure Gradient Flat Plate case. Section 2.2 discusses the 2D NASA Wall-Mounted Hump Separated Flow case and Section 2.3 discusses the Axisymmetric Shock Wave Boundary Layer Interaction case. All of the cases are validation cases where the CFD results are meant to compare against experimental data to investigate the model's ability to reproduce physics. To that end, the flow cases studied in this dissertation were selected to span an array of representative flow physics that will potentially be found in typical aerospace engineering applications. Section 2.4 presents the flow physics that are included in this study and in what cases they can occur.

2.1. 2D ZERO PRESSURE GRADIENT FLAT PLATE (2DZP)

This CFD problem is a 2D zero pressure gradient flat plate validation case taken from the NASA TMR [1]. A graphical overview of the computational domain for the 2D zero pressure gradient flat plate can be seen in Figure 2.1. The chord has a length of two units starting from $x = 0$ while the grid height is one unit which is far enough away to have little influence on the final solution. The freestream flow is defined by the following quantities: $M_{ref} = 0.2$, $T_{ref} = 40°R$, and $Re_L = 5 \times 10^6$ (based on a length of "1" grid unit). All flow solutions were obtained using the finest grid available on the NASA TMR [1] which is a 545×385 grid with 449 points on the solid plate and a minimum wall spacing of $y = 5{\times}10^{-7}$, giving an approximate average $y^+ = 0.1$ over the plate at the Reynolds number of the flow. The inlet total pressure and temperature ratio are $P_t/P_{ref} = 1.02828$ and $T_t/T_{ref} = 1.008$ respectively while the exit has a static pressure ratio of $P/P_{ref} = 1.0$. The surface of the

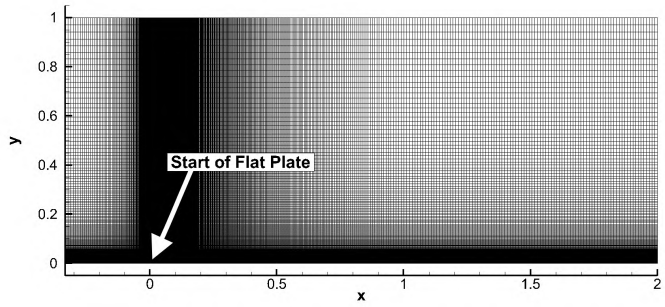

Figure 2.1. Computational grid for the 2D zero pressure gradient flat plate case.

flat plate was set to adiabatic solid wall boundary condition while the farfield Riemann boundary condition is imposed for the top boundary. The inlet extends approximately 0.3 units upstream from the leading edge of the plate. The symmetry boundary condition is imposed at $y = 0$ between the inlet and the leading edge of the flat plate.

2.2. 2D NASA WALL-MOUNTED HUMP SEPARATED FLOW (2DWMH)

This CFD problem is a 2D wall-mounted hump separated flow validation case for which experimental data is taken from Greenblatt et al [31, 32, 33]. A graphical overview of the computational domain for the 2D hump problem can be seen in Figure 2.2a while contours of the velocity flow field can be seen in Figure 2.2b. This validation test case is used to evaluate the ability of a turbulence model to predict the 2D flow separation from a smooth body in the presence of adverse pressure gradients and to gauge how well it predicts the flow's subsequent reattachment. The chord of the bump is 420 mm in length and the upstream "run" length is chosen to allow a naturally developed fully turbulent flow. The freestream flow is defined by the following quantities: $M_{ref} = 0.1$, $T_{ref} = 537°$, and $Re_c = 936,000$ (based on hump chord). All flow solutions were obtained using the finest available grid from the NASA TMR [1]. This grid contained 210,060 grid points and has a minimum spacing at the wall of approximately $y = 8 \times 10^{-6}$ grid units giving a y^+

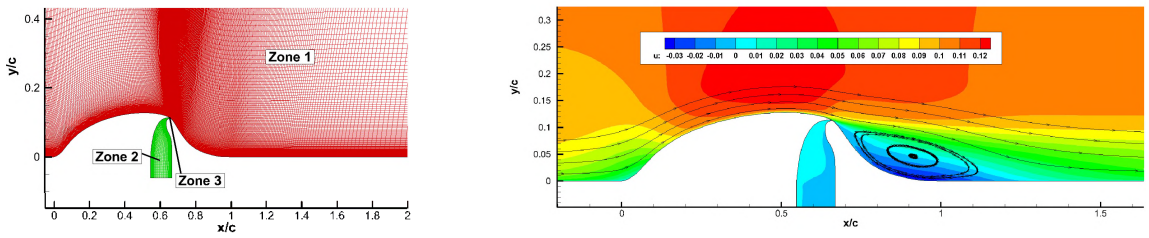

(a) Computational grid (hump region). (b) Scaled u-velocity contours obtained with SA model.

Figure 2.2. 2D NASA wall-mounted hump case overview.

average between 0.1 and 0.2 at the Reynolds number of the flow. The inlet total pressure and temperature ratio are $P_t/P_{ref} = 1.007$ and $T_t/T_{ref} = 1.002$ respectively while the exit has a static pressure ratio of $P/P_{ref} = 0.99962$. The surface of the body is set to adiabatic solid wall boundary condition while the top grid boundary and plenum floor are modeled as inviscid walls.

2.3. AXISYMMETRIC SHOCK WAVE BOUNDARY LAYER INTERACTION NEAR M=7 (ASWBLI)

The last CFD problem in this study is modeled after a hypersonic shock wave and turbulent boundary layer experiment performed by Kussoy and Horstman [34]. The test apparatus employed in the experiments were composed of a 10 cm diameter cylinder with an ogive nose and a 20° flare located 139 cm downstream of the leading edge and can be seen in Figure 2.3. The experiment was conducted in the NASA Ames 3.5-Foot Hypersonic Wind Tunnel. Test conditions were set such that the freestream had a total temperature of 900 K, a total pressure of 34 atm, a unit Reynolds number of 7×10^6 m^{-1}, and a Mach number of 7.2. This experiment has become a model for testing the efficacy of a turbulence model in predicting hypersonic shock wave and turbulent boundary layer interactions. In an effort to ease the computational expense associated with the full experimental geometry,

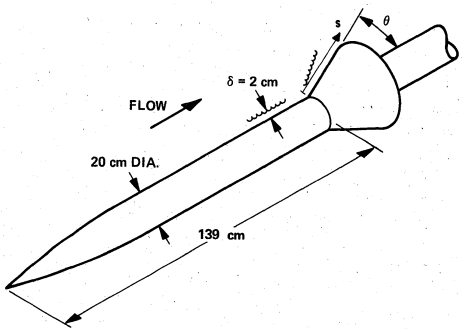

Figure 2.3. Experimental apparatus for hypersonic shock wave and turbulent boundary layer experiment.

Georgiadis et al. [30] compared the CFD results from a full geometry configuration to one where the nose cone was removed. They concluded that the no-cone solution provides identical results contingent upon an adjustment of the freestream conditions. These recommended adjustments (outlined below) were employed in this study of the no-cone geometry. While the focus of this study is on the quantification of uncertainty due to the variation of turbulence model coefficients, a comprehensive uncertainty analysis should also include other uncertainty sources including the uncertainty in geometry and freestream conditions. However, the ranking of the most significant coefficients in terms of their contribution to output uncertainty are expected to remain the same in the presence of other uncertainty sources.

The CFD problem is an axisymmetric shock wave boundary layer interaction validation case taken from the NASA TMR [1]. A graphical overview of the axisymmetric cylinder and 20 degree flare geometry can be seen in Figure 2.4a. The cylinder, with a radius of 10 cm, begins approximately 80 cm upstream of the 20 degree flare while the grid height is approximately 50 cm from the centerline of the cylinder. The freestream flow is defined by the following quantities: $M_{ref} = 7.11$, $T_{ref} = 80K$, and $Re_L = 57060$ per cm. The walls of both the cylinder and the flare are imposed with no-slip boundary conditions and maintain a constant temperature of 311 K. The remaining boundary conditions can be seen in Figure 2.4a. Contour lines of P/P_∞ can be seen in Figure 2.4b with labeled details

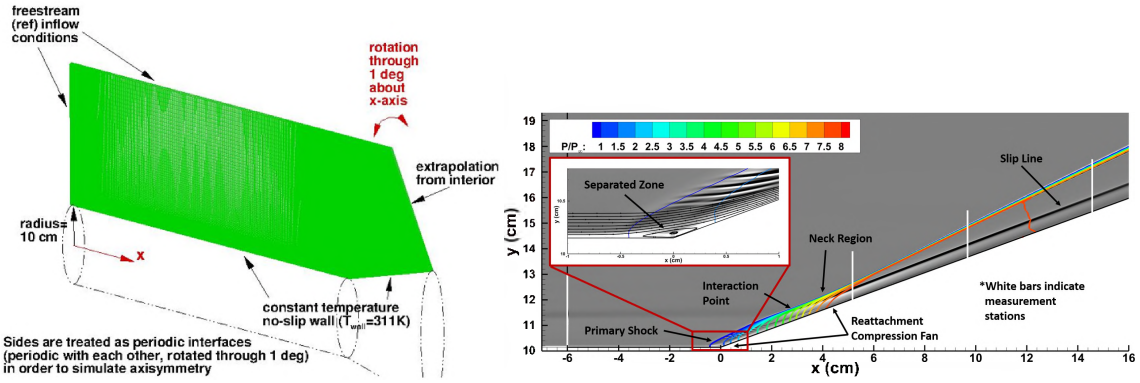

(a) Overview of the shock wave turbulent boundary layer interaction problem [1].

(b) Baseline solution showing contours of P/P_∞ with shock structure details and compression corner inset.

Figure 2.4. Axisymmetric shock wave boundary layer interaction case overview.

of the shock structure and flow regions. A zoomed in view of the compression corner where shock wave turbulent boundary layer interaction occurs along with the separated flow region is also included in the same figure. All solutions were obtained using a '1-level down' grid from the finest grid available and utilized a dual zone configuration. Each zone is 161×201 grid points in the axial and normal directions, respectively. A $y^+ < 1$ is enforced on all surfaces. The first zone begins at the start of the cylinder and continues upstream to a plane six centimeters aft of the flare. The second zone begins at the plane six centimeters aft of the flare and continues to the end of the flare.

To further decrease the computational expense of an uncertainty quantification study, an optimum grid size with an acceptable level of accuracy is desired. As such, a grid convergence study was performed for each turbulence model using the series of available grids on the NASA TMR [1] website. The wall heating results in Figure 2.5 shows that the 'Grid Level 1' (161x201 points) used in the current study provides nearly identical results compared to the fine grid ('Grid Level 0') solution for all of the turbulence models considered. Each level down from 'Grid Level 0' is obtained by reducing the previous grid level size by a factor of two in each direction (i.e., deleting the every other grid point in each direction).

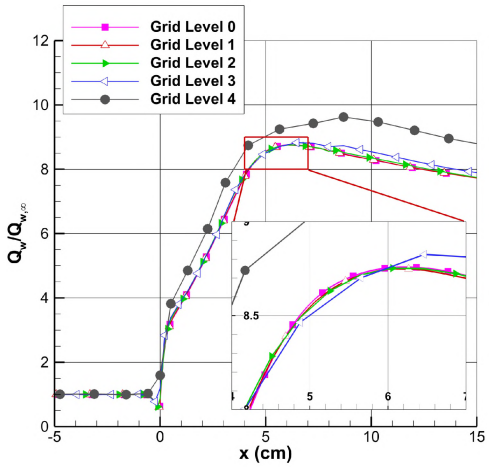

(a) Wall heating for SA turbulence model.

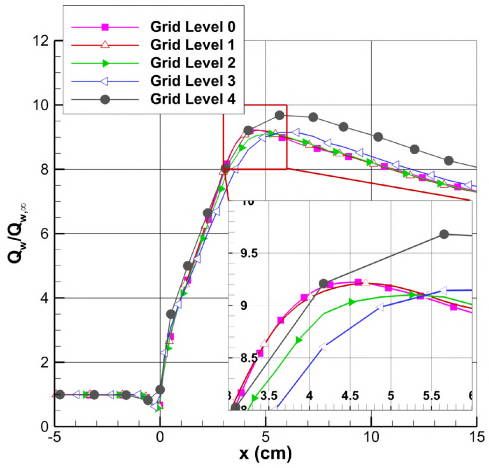

(b) Wall heating for W2006 turbulence model.

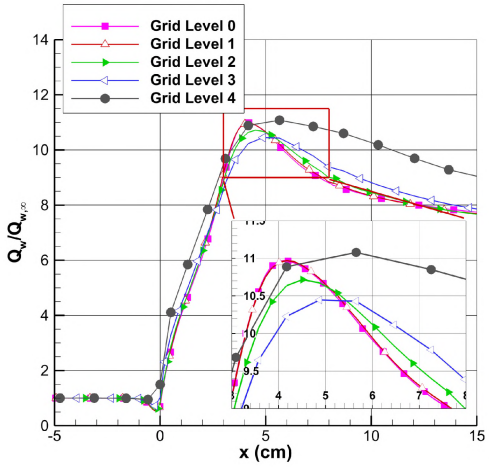

(c) Wall heating for SST turbulence model.

Figure 2.5. Grid convergence results for each turbulence model (ASWBLI).

2.4. FLOW PHYSICS

One of the main objectives of this study is to quantify the uncertainty and sensitivity of turbulence models due to the variation (or ambiguity) in closure coefficients using a series of canonical wall bounded CFD cases that span the gamut of flow physics potentially found in typical aerospace engineering applications to generalize the findings over different flow regimes. The cases are documented on the NASA TMR [1] as turbulence model validation cases. Slotnick et al. [7] state there is insufficient use of validation datasets to drive physics-based improvements to turbulence predictions and so this work aims to help fill the gap in understanding how the uncertainty in turbulence model closure coefficients affect the prediction of important QoIs in canonical CFD validation cases. Table 2.1 lists the three CFD test cases used in this study along with the observed flow physics in each simulation. There is an expectation that, with the results obtained in this study, each turbulence model studied will likely exhibit similar uncertainty and sensitivity behavior for flow problems which contain the physics outlined in this table. As presented in the conclusion, one important observation resulting from this study is that certain coefficients for each turbulence model are found be the most significant contributors to the output uncertainty regardless of the flow type studied.

The cases in Table 2.1 were chosen such that a wide range of flow physics could be investigated with some overlap from case to case. The 2DZP is a fundamental incompressible aerospace problem that demonstrates the log-law, where either the wall or BL edge properties are used to characterize the velocity profile. It is often used as a verification test bed of turbulence models in CFD. The fully attached flow and lack of complicated flow physics should allow the turbulence model to predict the flow with a high level of accuracy. The 2DWMH continues in the incompressible regime but introduces a large region of separated flow. The primary focus of this case is to assess the ability of turbulence models to predict separation on a 2D smooth body (caused by adverse pressure gradient) as well as subsequent reattachment and boundary layer recovery. The ASWBLI case rounds

Table 2.1. Test cases by flow physics (NASA TMR website).

		Wall Flows						
		Law of the Wall	Law of the Wake	Pressure Gradients	Turbulent Heat Flux	Higher Mach	Shock	Separation
Boundary Layers	2DZP	X	X					
Bump Flows	2DWMH			X				X
Shock/BL Interaction Flow	ASWBLI			X	X	X	X	X

out the selection by retaining a region of separated flow but introduces compressibility to the physics as well as shock wave prediction. This case is studied to assess the efficacy of RANS simulations to recreate the physics of higher Mach number flows including surface heat flux (aerodynamic heating) and shock induced turbulent boundary layer separation.

3. COMPUTATIONAL APPROACH

The purpose of this section is to give a brief description of the numerical methods employed in this dissertation. Outlining the numerical methodology is important for a study such as this where individual results are to be compared with each other and from results of previous work. A brief description of the flow solver including the numerical parameters used in each case is given first in Section 3.1. Following this, Section 3.2 provides details of the turbulence models employed in this study.

3.1. FUN3D

The CFD code employed for this study was FUN3D [35], a fully unstructured Navier-Stokes code developed by NASA Langley Research Center (LaRC). FUN3D is a RANS code capable of solving steady and unsteady laminar or turbulent flows from subsonic to hypersonic speeds using a node-based, three-dimensional, finite volume approach. Modified forms of FUN3D were employed for this study that made it possible to change the values of the closure coefficients.

The 2D Zero Pressure Gradient Flat Plate and 2D NASA Wall-Mounted Hump Separated Flow cases used a similar solution strategy. Both used a modified form of FUN3D version 12.4, and all solutions used a Roe, second-order flux differencing scheme with no flux limiter and second-order spatial accuracy for the viscous terms. The Courant-Friedrich-Lewy (CFL) numbers for the mean flow and turbulent model equations were increased from 1 to 50 and from 5 to 30, respectfully, during the first 500 iterations. The CFL values were subsequently fixed at their maximum value for the remaining simulation until steady state convergence was achieved.

Due to the different flow physics encountered in the Axisymmetric Shock Wave Boundary Layer Interaction problem, a slightly modified solution strategy was employed; an updated version of FUN3D (13.1) was also used for this problem. All solutions use the second-order modified Reimann solver of Harten, Lax, and van Leer (HLLC) [36] as the flux construction scheme and a stencil-based min-mod flux limiter augmented with a heuristic pressure limiter. Second-order spatial accuracy is used for the viscous terms. The Mach numbers of the mean flow are systematically ramped from 3.00 to 7.11 with an intermediate Mach number of 6.00. Before each ramping, the simulation was allowed to converge to a solution before restarting at a higher Mach number. This ramping allowed for faster convergence at the desired Mach number when compared to initializing the simulation at such a high speed. The CFL number for the mean flow and turbulent model was systematically increased from 0.1 to 10.0 and from 0.01 to 1.0, respectively, during the first 10,000 iterations of each restarted simulation. Upon reaching a desired solution convergence and a steady residual level, the flux limiter was frozen to allow the solver to reach a residual of machine zero which mitigated the oscillation of the solution and the residuals.

3.2. TURBULENCE MODELS

This section details the turbulence models as used in this study. In Section 3.2.1, the SA model, as implemented in the flow solver, is presented and the standard values of the closure coefficients are tabulated along with the bounded interval over which each coefficient was varied. A description of the function of each closure coefficient is also presented. In Section 3.2.2, the same treatment is preformed for the W2006 model; the model equations are presented followed by the values of the closure coefficients with accompanying descriptions. Likewise, Section 3.2.3 presents the description of the Menter

SST model with the values and descriptions of the closure coefficients. Note that the two-equation models (W2006 and SST) are presented in conservative form despite FUN3D [35] calculating the flow solutions using the primitive variable form.

3.2.1. Spalart-Allmaras. The Spalart-Allmaras (SA) turbulence model is a one equation model commonly used in engineering applications for aerodynamic flows. The origin of the model was motivated by Baldwin and Barth [37] as they attempted to generate a one equation model from the k-ϵ model, but it is more an evolution of the Nee-Kovasznay [38] with added near-wall and compressibility corrections [4]. The model, due in part to its single equation nature, is simpler and less computationally expensive than the multi-equation models while maintaining a robustness required for plausible results. The SA model is given by

$$\begin{aligned}\frac{\partial \hat{\nu}}{\partial t} + u_j \frac{\partial \hat{\nu}}{\partial x_j} = c_{b1}\left(1 - f_{t2}\right)\hat{S}\hat{\nu} - \left[c_{w1} f_w - \frac{c_{b1}}{\kappa^2} f_{t2}\right]\left(\frac{\hat{\nu}}{d}\right)^2 \\ + \frac{1}{\sigma}\left[\frac{\partial}{\partial x_j}\left(\left(\nu + \hat{\nu}\right)\frac{\partial \hat{\nu}}{\partial x_j}\right) + c_{b2}\frac{\partial \hat{\nu}}{\partial x_i}\frac{\partial \hat{\nu}}{\partial x_i}\right]\end{aligned} \tag{3.1}$$

The full formulation of the model is given by Spalart and Allmaras [4]. The closure coefficient descriptions are given in Table 3.1 and their suggested values are given in Table 3.2. The closure coefficients also include

$$c_{w1} = \frac{c_{b1}}{\kappa^2} + \frac{1 + c_{b2}}{\sigma} \tag{3.2}$$

The turbulent eddy viscosity is computed from:

$$\mu_t = \rho \hat{\nu} f_{v1} \tag{3.3}$$

where

$$f_{v1} = \frac{\chi^3}{\chi^3 + c_{v1}^3}, \quad \chi = \frac{\hat{\nu}}{\nu} \tag{3.4}$$

and ρ is the density, $\nu = \mu/\rho$ is the molecular kinematic viscosity, and μ is the molecular dynamic viscosity. Additional definitions are given by the following equations:

$$\hat{S} = \Omega + \frac{\hat{\nu}}{\kappa^2 d^2} f_{v2} \tag{3.5}$$

where $\Omega = \sqrt{2W_{ij}W_{ij}}$ is the magnitude of the vorticity, d is the distance from the field point to the nearest wall, and

$$\begin{aligned} f_{v2} &= 1 - \frac{\chi}{1 + \chi f_{v1}}, \qquad f_w = g\left[\frac{1 + c_{w3}^6}{g^6 + c_{w3}^6}\right]^{1/6}, \qquad g = r + c_{w2}\left(r^6 - r\right) \\ r &= \min\left[\frac{\hat{\nu}}{\hat{S}\kappa^2 d^2}, 10\right], \quad f_{t2} = c_{t3}\exp\left(-c_{t4}\chi^2\right), \quad W_{ij} = \frac{1}{2}\left(\frac{\partial u_i}{\partial x_j} - \frac{\partial u_j}{\partial x_i}\right) \end{aligned} \tag{3.6}$$

Table 3.1 provides a complete listing of the closure coefficients contained within the SA turbulence model along with a brief explanation of the function of each coefficient. In Table 3.2, the standard value of each coefficient along with its upper and lower bounds used in the uncertainty analysis is given. The intervals over which the coefficients are bounded are taken from a previous work by Schaefer et al. [39], who determined these values by consulting with the author of this turbulence model (expert opinion) and based on the available data in the literature. The table also lists whether the coefficient is varied in the specific CFD case considered. All the coefficients were initially considered as uncertain variables in a preliminary sensitivity analysis study; the reduced dimension UQ analysis presented in this dissertaion is performed on the closure coefficients providing at least 95% of the uncertainty to any of the output quantities of interest identified with the preliminary sensitivity analysis.

Table 3.1. SA closure coefficient descriptions.

Coefficient	Description
σ	Turbulent Prandtl number, part of diffusion term
κ	Von Kármán's constant; calibrates the log layer slope $\rightarrow \chi = \kappa y^+$
c_{v1}	Used in turbulent eddy viscosity calculation and production term. Helps control the log law intercept
c_{w3}	Part of the f_w function (in destruction term), which speeds up the decay rate of the destruction term in the outer region of the boundary layer.
c_{t3}	Part of f_{t2} function (in production and destruction terms), which helps transition prediction by attracting $\hat{\nu} = 0$ as a solution
c_{t4}	Part of f_{t2} function (in production and destruction terms), which helps transition prediction by attracting $\hat{\nu} = 0$ as a solution
c_{b1}	Calibrates the growth of ν_t, which grows as $\exp(c_{b1}St)$
c_{b2}	Ensures that the integral of $\nu_t^{1+c_{b2}}$ can only increase, and smooths out velocity profile if $(1 + c_{b2})/\sigma > 2$
c_{w2}	Part of g function, which controls the slope of f_w in destruction. Calibrated to match skin friction coefficient of flat plate

The SA model used in the Axisymmetric Shock Wave Boundary Layer Interaction analysis employs a variant of the model in which the f_{t2} term is set to zero. Rumsey and Spalart [40] found that, particularly for hypersonic simulations, the flow can often remain laminar and posit that the culprit for this behavior is possibly the f_{t2} term. The term is found in the production and destruction terms as seen in Eqs. (3.7) and (3.8), respectively.

$$c_{b1}\left(1 - f_{t2}\right)\hat{S}\hat{\nu} \tag{3.7}$$

$$-\left[c_{w1}f_w - \frac{c_{b1}}{\kappa^2}f_{t2}\right]\left(\frac{\hat{\nu}}{d}\right)^2 \tag{3.8}$$

where

$$\hat{S} = \Omega + \frac{\hat{\nu}}{\kappa^2 d^2}f_{v2} \tag{3.9}$$

$$f_{t2} = c_{t3}\exp\left(-c_{t4}\chi^2\right) \tag{3.10}$$

Table 3.2. SA closure coefficient epistemic bounds used in UQ study.

Coefficient	Standard Value	Lower Bound	Upper Bound
σ	2/3‡	0.6	1.0
κ	0.41‡	0.38	0.42
c_{v1}	7.1‡	6.9	7.3
c_{w3}	2.0	1.75	2.5
c_{t3}	1.2	1.0	2.0
c_{t4}	0.5	0.3	0.7
c_{b1}	0.1355‡	0.12893	0.13700
c_{b2}	0.622	0.60983	0.68750
c_{w2}	0.3‡	0.05500	0.35250

‡ denotes Closure Coefficient varied in current work

Both Eqs. (3.7) and (3.8) contain a $(1/d)^2$ term that becomes very large as d, or the normal wall distance, becomes very small near the wall, especially for fine grids. Toward the edges of the epistemic intervals, particularly when c_{t3} is large and c_{t4} is small, coupled with an increasing χ (ratio between the turbulence field variable to the molecular kinematic viscosity, $\hat{\nu}/\nu$) as it grows in the boundary layer, the f_{t2} term can grow prohibitively large. The product of the large $(1/d)^2$ and f_{t2} terms are particularly damaging to the model's ability to represent the physics. These non-physical results are represented in Figures 3.1a and 3.1b, which show the results when c_{t3} and c_{t4} are at the extremes of their epistemic bounds. These figures show that the case of a large c_{t3} and a small c_{t4} produces an abnormally small turbulent parameter response and results in flow separation. The presence of the f_{t2} term is to attract $\hat{\nu} = 0$ as a solution to the model equation; however, when f_{t2} is large and d is small, the model will tend to artificially laminarize the flow inside an otherwise turbulent boundary layer. As such, the analysis performed in this study sets f_{t2} to zero, effectively eliminating c_{t3} and c_{t4} from the list of uncertain variables.

3.2.2. Wilcox-2006 k-ω. The Wilcox k-ω model is a popular two equation model for modeling the turbulent kinetic energy of the flow and the length scale of the turbulent eddies. The first equation, k, transports the turbulent kinetic energy, while the second

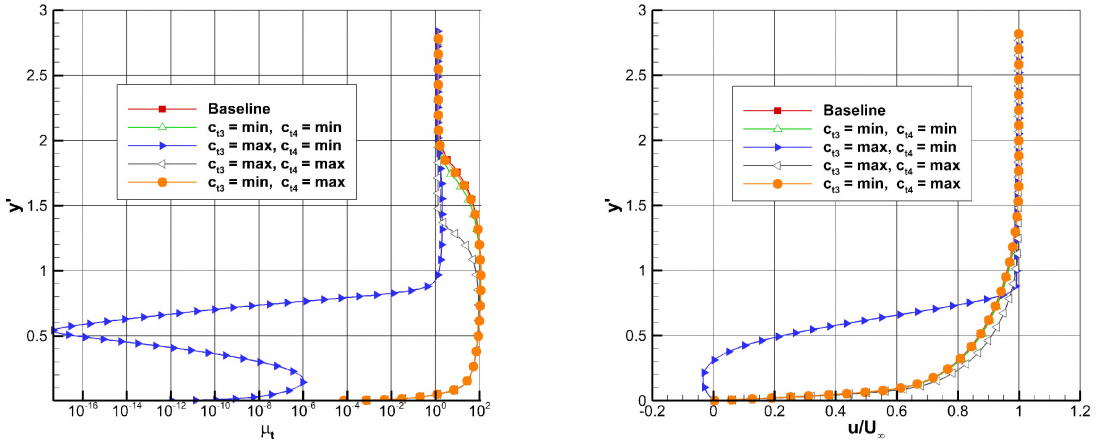

(a) Turbulent eddy viscosity.

(b) Nomalized velocity.

Figure 3.1. Investigation of the f_{t2} term in the SA model upstream of the shock wave ($S = -6$ cm) (ASWBLI).

equation, ω, is for the specific dissipation of turbulent kinetic energy. The 2006 Wilcox k-ω model updates the original formulation by introducing a cross-diffusion term and built-in stress limiter [41]. These additions greatly improved the accuracy for free shear flows and strongly separated flows. The W2006 model is given by

$$\frac{\partial(\rho k)}{\partial t} + \frac{\partial(\rho u_j k)}{\partial x_j} = P - \beta^* \rho \omega k + \frac{\partial}{\partial x_j}\left[\left(\mu + \sigma_k \frac{\rho k}{\omega}\right)\frac{\partial k}{\partial x_j}\right] \tag{3.11}$$

$$\frac{\partial(\rho \omega)}{\partial t} + \frac{\partial(\rho u_j \omega)}{\partial x_j} = \frac{\gamma \omega}{k} P - \beta \rho \omega^2 + \frac{\partial}{\partial x_j}\left[\left(\mu + \sigma_w \frac{\rho k}{\omega}\right)\frac{\partial \omega}{\partial x_j}\right] + \frac{\rho \sigma_d}{\omega}\frac{\partial k}{\partial x_j}\frac{\partial \omega}{\partial x_j} \tag{3.12}$$

The full formulation of the model is given by Wilcox [41]. The closure coefficient descriptions are given in Table 3.3 and their suggested values are given in Table 3.4. The closure coefficients also include

$$\gamma = \frac{\beta_0}{\beta^*} - \sigma_w \frac{\kappa^2}{\sqrt{\beta^*}} \tag{3.13}$$

Definitions of the terms in the model include:

$$P = \tau_{ij}\frac{\partial u_i}{\partial x_j} \tag{3.14}$$

$$\tau_{ij} = \mu_t\left(2S_{ij} - \frac{2}{3}\frac{\partial u_k}{\partial x_k}\delta_{ij}\right) - \frac{2}{3}\rho k\delta_{ij} \tag{3.15}$$

$$S_{ij} = \frac{1}{2}\left(\frac{\partial u_i}{\partial x_j} + \frac{\partial u_j}{\partial x_i}\right) \tag{3.16}$$

and the turbulent eddy viscosity is computed from:

$$\mu_t = \frac{\rho k}{\hat{\omega}} \tag{3.17}$$

where:

$$\hat{\omega} = \max\left[\omega,\ C_{lim}\sqrt{\frac{2\bar{S}_{ij}\bar{S}_{ij}}{\beta^*}}\right] \tag{3.18}$$

$$\bar{S}_{ij} = S_{ij} - \frac{1}{3}\frac{\partial u_k}{\partial x_k}\delta_{ij} \tag{3.19}$$

The auxiliary functions are

$$\begin{aligned} \chi_\omega &= \left|\frac{\Omega_{ij}\Omega_{jk}\hat{S}_{ki}}{(\beta^*\omega)^3}\right|, \qquad f_\beta = \frac{1+85\chi_\omega}{1+100\chi_\omega} \\ \hat{S}_{ki} &= S_{ki} - \frac{1}{2}\frac{\partial u_m}{\partial x_m}\delta_{ki}, \quad \Omega_{ij} = \frac{1}{2}\left(\frac{\partial u_i}{\partial x_j} - \frac{\partial u_j}{\partial x_i}\right) \\ \beta &= \beta_0 f_\beta, \quad \sigma_d = \begin{cases} 0, & \dfrac{\partial k}{\partial x_j}\dfrac{\partial \omega}{\partial x_j} \le 0 \\ \sigma_{do}, & \dfrac{\partial k}{\partial x_j}\dfrac{\partial \omega}{\partial x_j} > 0 \end{cases} \end{aligned} \tag{3.20}$$

Table 3.3 provides a complete listing the closure coefficients contained within the W2006 turbulence model along with a brief explanation of the function of each coefficient. Table 3.4 gives the standard value of each coefficient along with its upper and lower bounds

Table 3.3. W2006 closure coefficient descriptions.

Coefficient	Description
β^*	Relates (τ_{xy}/k), which equals ≈ 0.3 in the log layer; multiplies $k\omega$ in k-equation of the model
C_{lim}	Stress-limiter which improves model accuracy for shear flows and strongly separated flows
κ	Von Kármán's constant; involved in log layer calibration
β^*/β_0	β_0 used in the calculation of β for ω-equation; ratio approximates the time decay of homogeneous isotropic turbulence experiments
σ_w	Multiplies (k/ω) in ω-equation; value chosen to match empirical decay rate behavior of k and ν_T as wall distance increases
σ_k	Multiplies (k/ω) in k-equation; value chosen to match empirical decay rate behavior of k and ν_T as wall distance increases

Table 3.4. W2006 closure coefficient epistemic bounds used in UQ study.

Coefficient	Standard Value	Lower Bound	Upper Bound
β^*	$0.09^{\ddagger}$	0.0784	0.1024
C_{lim}	$0.875^{\ddagger}$	0.75	1.0
κ	$0.40^{\ddagger}$	0.38	0.42
β^*/β_0	1.2712	1.19	1.31
σ_w	$0.5^{\ddagger}$	0.5	0.7
σ_k	$0.6^{\ddagger}$	0.5	0.6

‡ denotes Closure Coefficient varied in current work

used in the uncertainty analysis. Similar to the SA model, the intervals over which the coefficients are bounded are from the previous work by Schaefer et al. [39], who determined these values by consulting with the author of this turbulence model (expert opinion) and based on the available data in the literature. Likewise, an initial full dimensional sensitivity analysis of the CFD case was performed and the closure coefficients contributing at least 95% accumulated uncertainty to any output quantity of interest was retained in this reduced dimension UQ study.

3.2.3. Menter-SST. The Menter SST model employs a blending technique to functionally combine the k-ω and k-ϵ models [6]. The intention of this blending is to use the turbulence models where they are most effective. The SST model utilizes the k-ω model near the wall where it is most accurate then transitions to the k-ϵ in the outer boundary layer. The SST model is given by

$$\frac{\partial(\rho k)}{\partial t} + \frac{\partial(\rho u_j k)}{\partial x_j} = P - \beta^* \rho \omega k + \frac{\partial}{\partial x_j}\left[(\mu + \sigma_k \mu_t)\frac{\partial k}{\partial x_j}\right] \tag{3.21}$$

$$\begin{aligned}\frac{\partial(\rho \omega)}{\partial t} + \frac{\partial(\rho u_j \omega)}{\partial x_j} = {} & \frac{\gamma}{\nu_t} P - \beta \rho \omega^2 + \frac{\partial}{\partial x_j}\left[(\mu + \sigma_w \mu_t)\frac{\partial \omega}{\partial x_j}\right] \\ & + 2(1 - F_1)\frac{\rho \sigma_{w2}}{\omega}\frac{\partial k}{\partial x_j}\frac{\partial \omega}{\partial x_j}\end{aligned} \tag{3.22}$$

The full formulation of the model is given by Menter [6]. The closure coefficient descriptions are given in Table 3.5 and their suggested values are given in Table 3.6. The closure coefficients also include

$$\gamma_1 = \frac{\beta_1}{\beta^*} - \sigma_{w1}\frac{\kappa^2}{\sqrt{\beta^*}} \tag{3.23}$$

$$\gamma_2 = \frac{\beta_2}{\beta^*} - \sigma_{w2}\frac{\kappa^2}{\sqrt{\beta^*}} \tag{3.24}$$

As in the W2006 model, P, τ_{ij}, and S_{ij} are given by:

$$P = \tau_{ij}\frac{\partial u_i}{\partial x_j} \tag{3.25}$$

$$\tau_{ij} = \mu_t\left(2S_{ij} - \frac{2}{3}\frac{\partial u_k}{\partial x_k}\delta_{ij}\right) - \frac{2}{3}\rho k \delta_{ij} \tag{3.26}$$

$$S_{ij} = \frac{1}{2}\left(\frac{\partial u_i}{\partial x_j} + \frac{\partial u_j}{\partial x_i}\right) \tag{3.27}$$

but the turbulent eddy viscosity is computed from:

$$\mu_t = \frac{\rho a_1 k}{\max(a_1\omega,\ \Omega F_2)} \tag{3.28}$$

Each of the constants is a blend of an inner (1) and outer (2) constant, blended via

$$\phi = F_1\phi_1 + (1 - F_1)\phi_2 \tag{3.29}$$

where ϕ_1 represents constant 1 and ϕ_2 represents constant 2. Additional functions are given by

$$\begin{aligned}
F_1 &= \tanh(arg_1^4), \quad & arg_1 &= \min\left[\max\left(\frac{\sqrt{k}}{\beta^*\omega d}, \frac{500\nu}{d^2\omega}\right), \frac{4\rho\sigma_{\omega 2}k}{CD_{k\omega}d^2}\right] \\
\nu_t &= \frac{\mu_t}{\rho}, & CD_{k\omega} &= \max\left(2\rho\sigma_{\omega 2}\frac{1}{\omega}\frac{\partial k}{\partial x_j}\frac{\partial \omega}{\partial x_j},\ 10^{-20}\right) \\
F_2 &= \tanh(arg_2^2), \quad & arg_2 &= \max\left(2\frac{\sqrt{k}}{\beta^*\omega d}, \frac{500\nu}{d^2\omega}\right) \\
\Omega &= \sqrt{2W_{ij}W_{ij}}, & W_{ij} &= \frac{1}{2}\left(\frac{\partial u_i}{\partial x_j} - \frac{\partial u_j}{\partial x_i}\right)
\end{aligned} \tag{3.30}$$

where ρ is the density, ν_t is the turbulent kinematic viscosity, μ is the dynamic viscosity, d is the distance from the field point to the nearest wall, and Ω is the vorticity magnitude.

Table 3.5 provides a complete listing the closure coefficients contained within the Menter SST turbulence model along with a brief explanation of the function of each coefficient. Table 3.6 gives the standard value of each coefficient along with its upper and lower bounds used in the uncertainty analysis. Similar to the SA and W2006 models, the intervals over which the coefficients are bounded are taken from the previous work by Schaefer et al. [39], who determined these values by consulting with the author of this turbulence model (expert opinion) and based on the available data in the literature.

Table 3.5. SST closure coefficient descriptions.

Coefficient	Description
σ_{k1}, σ_{k2}	Blended and multiplied by (k/ω) in k-equation; values chosen to match empirical decay rate of k and ν_T as wall distance increases
σ_{w1}, σ_{w2}	Blended and multiplied by (k/ω) in ω-equation; values chosen to match empirical decay rate of k and ν_T as wall distance increases
$\beta^*/\beta_1, \beta^*/\beta_2$	Blend of β_1 and β_2 used in the calculation of β for ω-equation; The blended ratio approximates the time decay of homogeneous isotropic turbulence experiments
β^*	Relates (τ_{xy}/k), which equals ≈ 0.3 in the log layer. Multiplies $k\omega$ in k-equation of the model
κ	Von Kármán's constant; involved in log layer calibration
a_1	Shear stress limiter used in turbulent eddy viscosity definition

Table 3.6. SST closure coefficient epistemic bounds used in UQ study.

Coefficient	Standard Value	Lower Bound	Upper Bound
σ_{k1}	0.85	0.7	1.0
σ_{k2}	1.0	0.8	1.2
σ_{w1}	$0.5^{\ddagger}$	0.3	0.7
σ_{w2}	$0.856^{\ddagger}$	0.7	1.0
β^*/β_1	$1.20^{\ddagger}$	1.19	1.31
β^*/β_2	$1.0870^{\ddagger}$	1.05	1.45
β^*	$0.09^{\ddagger}$	0.0784	0.1024
κ	$0.41^{\ddagger}$	0.38	0.42
a_1	$0.31^{\ddagger}$	0.31	0.40

‡ denotes Closure Coefficient varied in current work

Likewise, an initial full dimension sensitivity analysis of the CFD case was performed and the set of closure coefficients contributing at least 95% uncertainty to any output quantity of interest was retained in this reduced dimension UQ study.

4. UNCERTAINTY QUANTIFICATION APPROACH

Uncertainties in computational models fall into two categories: aleatory and epistemic. Aleatory uncertainties represent inherent variations in a system, whereas epistemic uncertainties arise due to lack of knowledge. In this work, all closure coefficients are treated as epistemic uncertain variables due to the lack of knowledge in identifying their values for each particular flow problem. As emphasized in the Introduction, this study is not an investigation into the model form uncertainty that is due to the fundamental RANS-based modeling assumptions including missing terms and unmodeled effects (spatial and temporal turbulent scales). In this dissertation, the parametric uncertainty within each turbulence model is investigated without actually changing the form of the model. Any reduction in the uncertainty of the closure coefficients with more knowledge gained via validation experiments are expected to improve the prediction capability of RANS models for the simulation of canonical flow problems considered in this study. Section 4.1 describes the point-collocation non-intrusive polynomial chaos method utilized to propagate these epistemic uncertainties through the model. Sobol indices are employed as a measure of sensitivity and are described in Section 4.2. Lastly, a normalized weighted Sobol index is introduced in Section 4.3 which provides a measure for the overall contribution of uncertainty from each uncertain variable to the QoI based on the sensitivity of that variable and the magnitude of uncertainty in the solution.

4.1. POINT-COLLOCATION NONINTRUSIVE POLYNOMIAL CHAOS

Rather than resorting to Monte Carlo simulations for uncertainty quantification, stochastic expansions based on point-collocation non-intrusive polynomial chaos (NIPC) were employed to reduce computational expense. The strategy of point-collocation NIPC is to create a surrogate model via least squares approach (i.e., polynomial response surface)

by using the CFD output obtained at a number of Latin Hypercube sample points for the propagation of uncertainty. An explanation of point-collocation NIPC given by West et al.[15] follows. With the polynomial chaos approach, a stochastic response function α^* (e.g., drag coefficient, pressure or skin friction coefficient at a given point in the flow field) can be decomposed into separable deterministic and stochastic components within a series expansion:

$$\alpha^*(\boldsymbol{x}, \boldsymbol{\xi}) \approx \sum_{i=0}^{P} \Psi_i(\boldsymbol{\xi}) \alpha_i(\boldsymbol{x}) \tag{4.1}$$

where α_i is the deterministic component and Ψ_i is the random variable basis functions corresponding to the i^{th} mode. α^* is assumed to be a function of a deterministic vector x, which includes the spatial coordinates and deterministic parameters of the problem, and of the n-dimensional standard random variable vector ξ. In theory, the series in Eq. (4.1) is infinite, but for practical implementation of the polynomial chaos expansions it is truncated and a discrete sum is taken over a number of output modes, $(P + 1)$. Further details on polynomial chaos theory are given by Ghanem [42] and Eldred [43]. There are three parameters that determine the number of samples required to generate the response surface: the number of uncertain variables, n; the order of the response surface polynomial, p; and the oversampling ratio, n_p. The total number of samples, N_s, is then given by

$$N_s = n_p \cdot (P + 1) = n_p \left[\frac{(n + p)!}{n!p!} \right] \tag{4.2}$$

The point-collocation NIPC method starts with replacing a stochastic response or random function with its polynomial chaos expansion in Eq. (4.1). Then, N_s vectors are chosen in random space and the deterministic code (the CFD flow solver in this case) is evaluated at these points; this is the left-hand side of Eq. (4.1). Finally a linear system of N_s equations is formulated and solved for the spectral modes of the random variables. This system is

given by:

$$\begin{pmatrix} \alpha^*(\boldsymbol{x},\boldsymbol{\xi}_0) \\ \alpha^*(\boldsymbol{x},\boldsymbol{\xi}_1) \\ \vdots \\ \alpha^*(\boldsymbol{x},\boldsymbol{\xi}_{(N_s-1)}) \end{pmatrix} = \begin{pmatrix} \Psi_0(\boldsymbol{\xi}_0) & \Psi_1(\boldsymbol{\xi}_0) & \dots & \Psi_P(\boldsymbol{\xi}_0) \\ \Psi_0(\boldsymbol{\xi}_1) & \Psi_1(\boldsymbol{\xi}_1) & \dots & \Psi_P(\boldsymbol{\xi}_1) \\ \vdots & \vdots & \ddots & \vdots \\ \Psi_0(\boldsymbol{\xi}_{(N_s-1)}) & \Psi_1(\boldsymbol{\xi}_{(N_s-1)}) & \dots & \Psi_P(\boldsymbol{\xi}_{(N_s-1)}) \end{pmatrix} \begin{pmatrix} \alpha_0 \\ \alpha_1 \\ \vdots \\ \alpha_P \end{pmatrix} \tag{4.3}$$

An oversampling ratio of 1.0 yields the minimum number of samples required to produce a response surface. Hosder et al. [44] demonstrated that an oversampling ratio of $n_p = 2.0$ gives a better approximation to the statistics at each polynomial degree they considered. For this reason, $n_p = 2.0$ was used for all of the UQ analyses in this work. Given $n_p > 1.0$, Eq. (4.3) is overdetermined and can be solved using a least squares approach. In the current work, a polynomial order of two ($p = 2$) was used for all UQ analyses. A summary of the computational cost for the UQ analysis of each case is included in Table 4.1. A full dimension analysis was first performed for each turbulence model and for each flow case. The closure coeffcients that were found to provide at least 95% of the uncertainty to any of the output quantities of interest were carried forward into the reduced dimension analysis presented here. The purpose for this strategy is to more accurately model the surrogate used in the NIPC method and therefore rank the contribution to QoI uncertainty from the significant closure coefficients with a numerically more accurate surrogate model.

Due to the bounded nature of epistemic input uncertainties, Legendre polynomials are used as the basis functions in this study. Although stochastic response surfaces created with the NIPC approach allow the calculation of confidence intervals along with various statistics of the output for probabilistic (aleatory) input, in this study, since all the uncertain parameters are considered as epistemic uncertain variables, only the maximum and the minimum of the response will be calculated from the response surface to determine the epistemic interval for each uncertain output. An important note that should be mentioned

Table 4.1. Number of CFD evaluations required for full and reduced dimensions UQ analyses.

Turbulence	Full Dimension				RD for 2DZP				RD for 2DWMH				RD for ASWBLI			
Model	n	p	n_p	N_s	n	p	n_p	N_s	n	p	n_p	N_s	n	p	n_p	N_s
SA	9	2	2	110	7	2	2	72	6	2	2	56	5	2	2	42
W2006	6	2	2	56	3	2	2	20	4	2	2	30	5	2	2	42
SST	9	2	2	110	5	2	2	42	6	2	2	56	7	2	2	72

is that as additional information is gathered that could reduce the epistemic uncertainty of the closure coefficients (e.g. experimental data), the uncertainty in the values of the QoIs will also be reduced.

4.2. SOBOL INDEX

Sobol indices (global nonlinear sensitivity indices) were used to rank the relative contributions of each closure coefficient to the total uncertainty in the output quantities of interest. Sobol indices can be derived via Sobol decomposition, which is a variance-based global sensitivity analysis method. This derivation utilizes the polynomial chaos expansion coefficients calculated in Eq. (4.3). First, the total variance, D, can be written in terms of the polynomial chaos expansion as shown in Eq. (4.4).

$$D = \sum_{j=1}^{P} \alpha_j^2(t,\vec{x}) \left\langle \Psi_j^2(\vec{\xi}) \right\rangle \tag{4.4}$$

Then, as shown by Sudret [45] and Crestaux et al. [46], the total variance can be decomposed as:

$$D = \sum_{i=1}^{i=n} D_i + \sum_{1\le i<j\le n}^{i=n-1} D_{i,j} + \sum_{1\le i<j<k\le n}^{i=n-2} D_{i,j,k} + \cdots + D_{1,2,\ldots,n} \tag{4.5}$$

where the partial variances ($D_{i_1,\ldots,i_s}$) are given by:

$$D_{i_1,\ldots,i_s} = \sum_{\beta \in \{i_1,\ldots,i_s\}} \alpha_\beta^2 \left\langle \Psi_\beta^2(\vec{\xi}) \right\rangle, \qquad 1 \le i_1 < \ldots < i_s \le n \tag{4.6}$$

Then the Sobol indices ($S_{i_1 \cdots i_s}$) are defined as,

$$S_{i_1 \cdots i_s} = \frac{D_{i_1,\ldots,i_s}}{D} \tag{4.7}$$

which satisfy the following equation:

$$\sum_{i=1}^{i=n} S_i + \sum_{1 \le i < j \le n}^{i=n-1} S_{i,j} + \sum_{1 \le i < j < k \le n}^{i=n-2} S_{i,j,k} + \cdots + S_{1,2,\ldots,n} = 1.0 \tag{4.8}$$

The Sobol indices provide a sensitivity measure due to individual contribution from each input uncertain variable (S_i), as well as the mixed contributions ($\{S_{i,j}\}, \{S_{i,j,k}\}, \cdots$). As shown by Sudret [45] and Ghaffari et al. [47], the total (combined) effect (S_{T_i}) of an input parameter i is defined as the summation of the partial Sobol indices that include the particular parameter:

$$S_{T_i} = \sum_{L_i} \frac{D_{i_1,\ldots,i_s}}{D}; \quad L_i = \{(i_1, \ldots, i_s) : \exists\ k,\ 1 \le k \le s,\ i_k = i\} \tag{4.9}$$

For example, with $n = 3$, the total contribution to the overall variance from the first uncertain variable ($i = 1$) can be written as:

$$S_{T_1} = S_1 + S_{1,2} + S_{1,3} + S_{1,2,3} \tag{4.10}$$

These formulations show that the Sobol indices can be used to provide a relative ranking of each input uncertainty to the overall variation in the output with the consideration of nonlinear correlation between input variables and output quantities of interest.

4.3. NORMALIZED WEIGHTED SOBOL INDEX

In the numerical modeling of canonical flow problems considered in this dissertation, it is desirable to determine which sources contribute most to the solution uncertainty and their location in the flow field so that appropriate uncertainty mitigation efforts, such as the planning of validation experiments to reduce model form uncertainty, can be established. To that end, an effort was made to couple the output from the point-collocation NIPC and the Sobol index approaches. This new metric shown in Eq. (4.11) is called the normalized weighted Sobol index (NWSI). The NWSI can help identify the location and source for the largest contribution to the solution uncertainty for flow field and surface quantities.

$$NWSI_{m_k} = \frac{S_{m_k}\epsilon_m}{max(S_m\epsilon_m)} \tag{4.11}$$

This metric for the m^{th} QoI is the product of the Sobol index for the k^{th} uncertain variable (S_{m_k}) and the magnitude of the uncertainty (i.e., the epistemic interval) from the point-collocation NIPC result (ϵ_m). This product is then normalized by the maximum value for each of the quantities of interest. The method for determining the NWSI scales the Sobol index results to display by the local uncertainty magnitude.

Additionally, the contribution from each uncertain variable can be condensed into a single quantifiable metric in order to rank the contribution from all the variables over a domain of interest. The following normalized integrated weighted Sobol index (NIWSI) given in Eq. (4.12) does this by evaluating a weighted Sobol index metric along the domain. In this equation, the values in the integrand are a specific uncertain variable's Sobol index at a particular location and are weighted by the magnitude of the uncertainty at that same location. This integral is evaluated numerically and is then normalized by the sum of n

uncertain variable integrals.

$$NIWSI_{m_k} = \frac{\int_D \{S_{m_k}(\theta)\epsilon_m(\theta)\}d\theta}{\sum_{i=1}^{n}\left[\int_D \{S_{m_i}(\theta)\epsilon_m(\theta)\}d\theta\right]} \tag{4.12}$$

where

$NIWSI_{m_k}$ ≡ Normalized integrated weighted Sobol index of the k^{th} uncertain variable for the m^{th} QoI

S_{m_k} ≡ Sobol index of the k^{th} uncertain variable for the m^{th} QoI

ϵ_m ≡ Uncertain bound for the m^{th} QoI

θ ≡ Variable of integration (such as the height of a pitot tube in a pitot rake)

D ≡ Integration domain along θ (such as the full span of a pitot rake)

An approach such as this enables ranking the extent to which an uncertain variable contributes to the output uncertainty over a domain of interest. This ranking can then be compared to similar studies to establish a pattern of contributing uncertain factors.

5. RESULTS AND DISCUSSION

This section will present the results from the uncertainty quantification analysis and discuss the generalization that can be gleaned from comparing this set of canonical flow cases. Section 5.1 will present the results from the individual flow cases by identifying the major sources of uncertainty from each of the SA, W2006, and SST turbulence models. Section 5.2 will then compare the results of the the three cases studied within this dissertation as well as previous work relevant to this study.

5.1. TEST CASE RESULTS

This section will present the results of the three canonical flow cases. Section 5.1.1 will show the 2D Zero Pressure Gradient Flat Plate results. Section 5.1.2 will present the findings from the 2D NASA Wall Mounted Hump case. Finally, Section 5.1.3 will present the results from the Axisymmetric Shock Wave Boundary Layer Interaction case.

5.1.1. 2D Zero Pressure Gradient Flat Plate Case. The first case discussed is the 2DZP case. Stochastic response surfaces were generated at each axial location along the chord of the flat plate from $x/c \in [0, 1]$ to inspect the uncertainty in the skin friction coefficient (C_f) and the momentum thickness Reynolds number (Re_θ). The minimum and maximum values of these quantities were determined from the response surfaces and plotted along with the baseline case and all the UQ training cases. Additionally, the uncertainty and sensitivity of the log-law velocity variable (u^+) is investigated at specific locations along the chord.

The SA model is investigated first. In Figures 5.1a and 5.1b, σ and κ contribute most to the uncertainty in skin friction coefficient. The major contributor alternates near the leading edge, and then κ becomes the dominant contributor for the majority of the chord. The results of the momentum thickness Reynolds number is presented next in Figure 5.2.

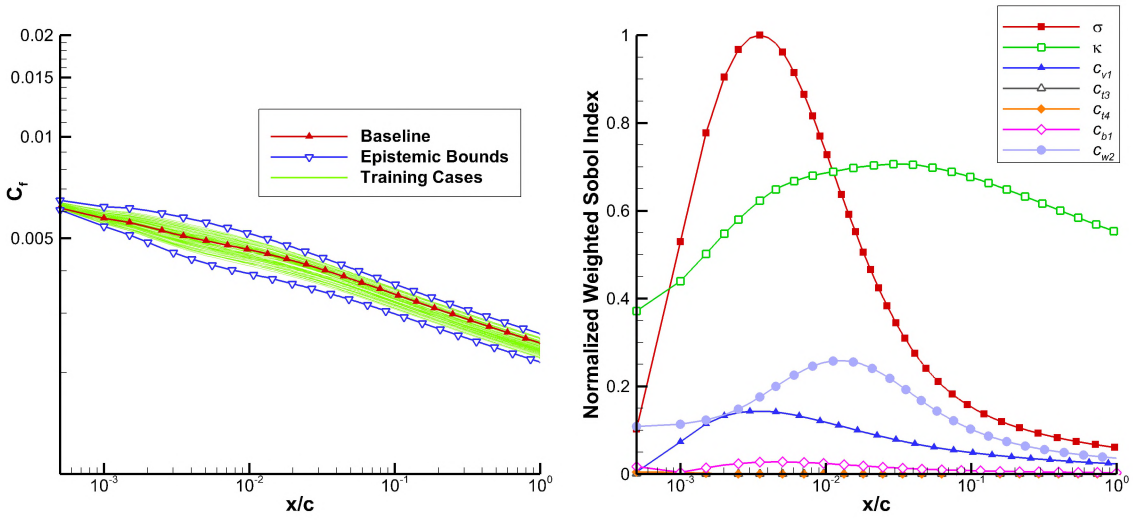

(a) C_f versus x/c. (b) NWSI for C_f versus x/c.

Figure 5.1. Skin friction coefficient results for 2DZP (SA model).

Figure 5.2a shows that the uncertainty in Re_θ grows uniformly from the leading edge of the flat plate to the trailing edge as the boundary layer grows across the chord. Figure 5.2b shows that the largest source of parametric uncertainty in Re_θ is the log-layer constant, κ, and is the largest at the trailing edge. Figures 5.3a and 5.3b present the evolution of u^+ profiles along the length of the chord from the leading edge to the $1/4$ chord, $1/2$ chord, $3/4$ chord, and the trailing edge. The closure coefficient that provides the most significant uncertainty to u^+ is κ. Uncertainties in σ, c_{w2}, and c_{v1} spike near the intersection of the viscous sublayer with the logarithmic region with the uncertainty in c_{v1} extending throughout the logarithmic region. An additional spike in uncertainty for σ and c_{w2} occurs at the boundary layer edge.

Figures 5.4a and 5.4b show that the W2006 model closure coefficients that contribute most to the uncertainty in skin friction coefficient are C_{lim}, β^*, and σ_w. The coefficients C_{lim} and β^* dominate the uncertainty at the plate's leading edge and are responsible for the large underpredictive uncertainty between $x/c = 0.001$ and 0.01. After this region, σ_w provides the majority of the uncertainty throughout the remaining chord. Figure 5.5 shows the results of the momentum thickness Reynolds number using the W2006 turbulence model. The uncertainty in Re_θ is shown in Figure 5.5a where the epistemic bounds grow

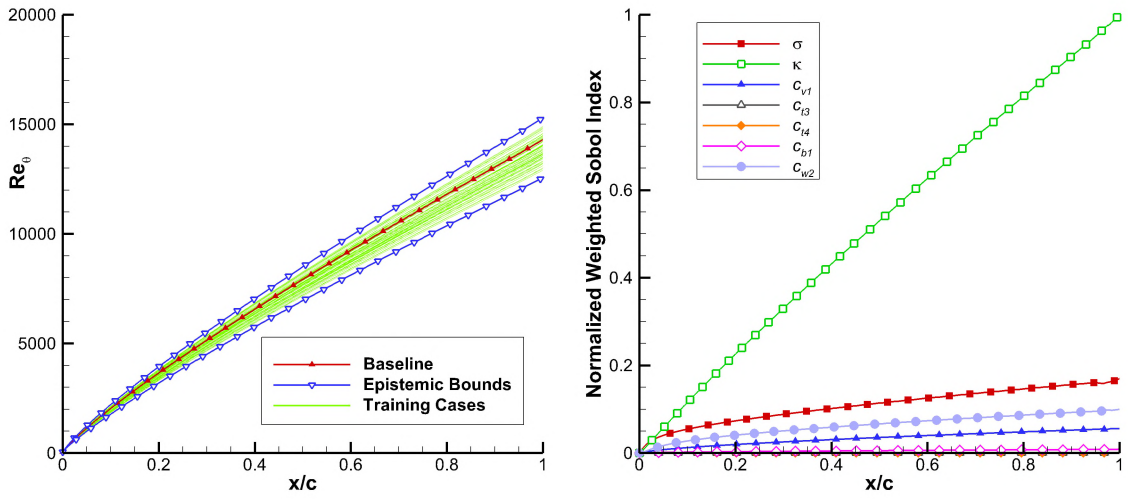

(a) Re_θ versus x/c.

(b) NWSI for Re_θ versus x.

Figure 5.2. Momentum thickness Reynolds number results for 2DZP (SA model).

along the length of the chord, though the magnitude of this uncertainty is less than the SA model. It can also be seen that the uncertainty in the closure coefficients tends to lessen the value of Re_θ. Figure 5.5b shows that uncertainty in Re_θ is dominated by the diffusion constant, σ_w. Figures 5.6a and 5.6b present the evolution of u^+ along the length of the chord starting from the leading edge to the $1/4$ chord, $1/2$ chord, $3/4$ chord, and the trailing edge for the W2006 turbulence model. The closure coefficient contributing most to the u^+ uncertainty at the leading edge of the plate is C_{lim} and begins at the transition from the viscous sublayer to the logarithmic region; β^* also contributes to the uncertainty in this region but to a lesser extent. After the leading edge, the uncertainty is dominated by σ_w where the extent of uncertainty grows throughout the logarithmic region of the boundary layer with maximum uncertainty at each station occurring at the boundary layer edge. C_{lim} and β^* contribute almost equally to the uncertainty with spikes observed at the viscous sublayer to logarithmic region transition location and at the boundary layer edge.

The SST model closure coefficients that contribute the most uncertainty to the skin friction coefficient solution are investigated in Figures 5.7a and 5.7b. Here, β^* dominates the uncertainty contribution while a few of the remaining coefficients play minor roles at either

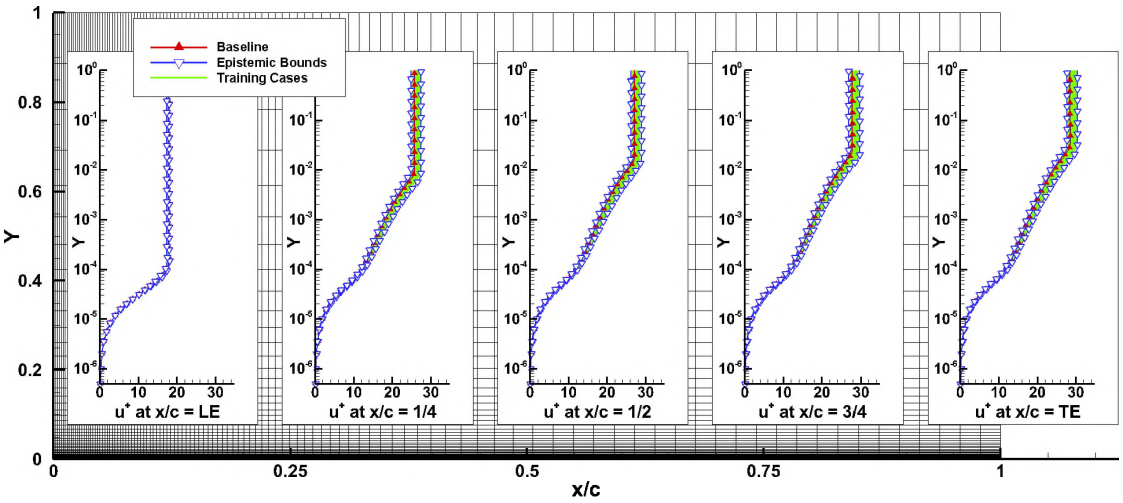

(a) u^+ versus y along the chord.

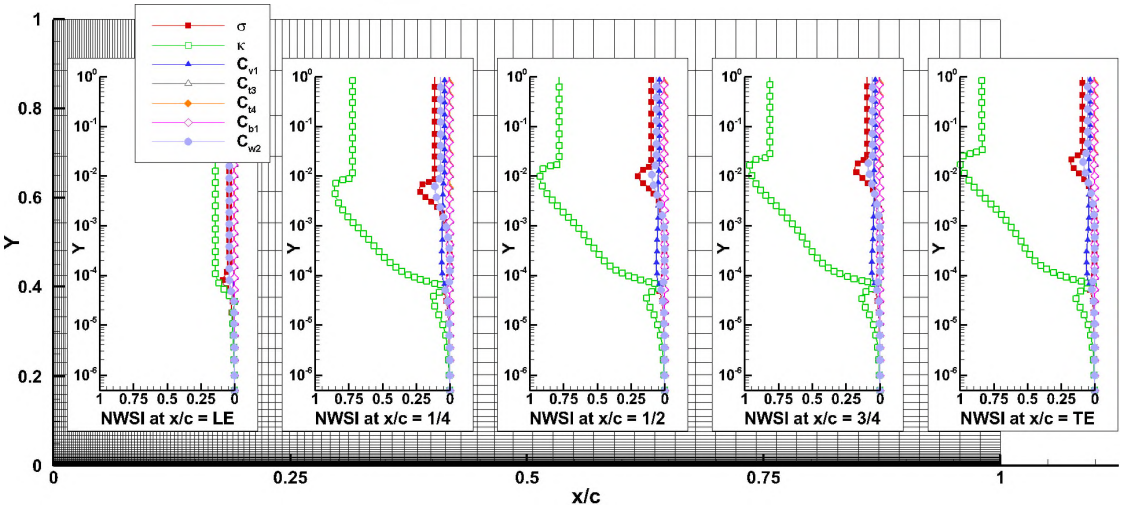

(b) NWSI for u^+ versus y along the chord.

Figure 5.3. $\boldsymbol{u^+}$ results for 2DZP (SA model).

the leading-edge location (a_1 and β^*/β_1) or at the trailing edge (σ_{w1} and β^*/β_1). The SST turbulence model results of the momentum thickness Reynolds number is presented next in Figure 5.8. Figure 5.8a shows that, like the results from the SA and W2006 turbulence models, the uncertainty in Re_θ grows uniformly across the flat plate from the leading edge to the trailing edge. The epistemic bounds are largest in this model compared to the previous two and the closure coefficient uncertainty tends to increase the value of Re_θ. Figure 5.8b shows that the dominate source of Re_θ uncertainty comes from β^* and is largest at the

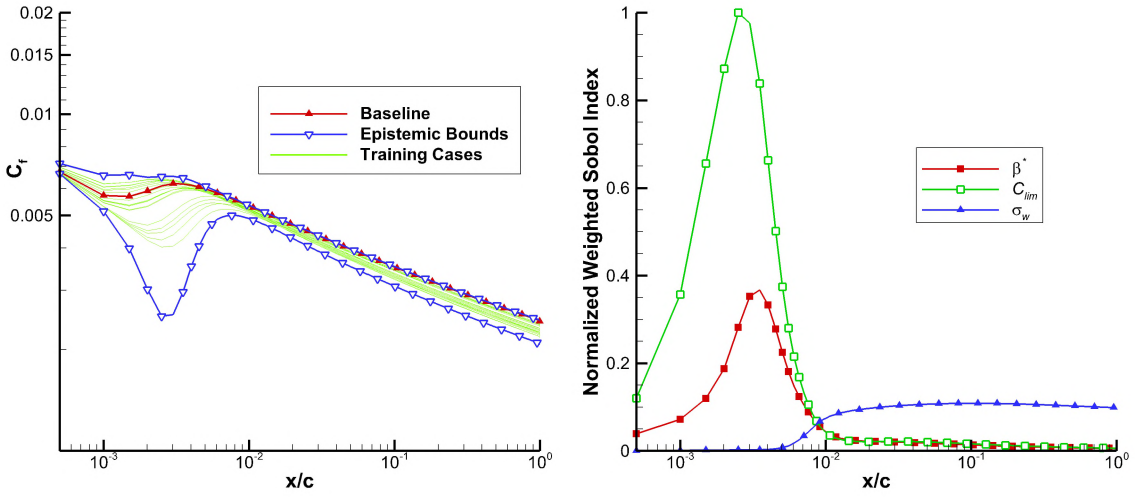

(a) C_f versus x/c. (b) NWSI for C_f versus x/c.

Figure 5.4. Skin friction coefficient results for 2DZP (W2006 model).

trailing edge. Figures 5.9a and 5.9b present the evolution of u^+ uncertainty along the chord from the leading edge to the $1/4$ chord, $1/2$ chord, $3/4$ chord, and the trailing edge for the SST turbulence model. The closure coefficient that contributes most to the uncertainty is β^* at every station. The large contribution to the uncertainty begins at the intersection of the viscous sublayer with the logarithmic layer and continues to grow throughout the logarithmic region. There exists a small spike in the contribution from σ_{w1} at the viscous sublayer to logarithmic transition and an additional spike from both σ_{w1} and β^*/β_1 at the boundary layer edge. An important fact to note is the comparatively large uncertainty band in the c_f, Re_θ, and u^+ prediction from the SST model that is nearly twice as large as the SA and W2006 results. The significantly larger uncertainty intervals indicate the sensitive nature of the SST model to the variation in its closure coefficients.

Following the qualitative analysis, a quantitative assessment of the level of contribution of each coefficient to the overall uncertainty is performed. Table 5.1 lists the NIWSI for the skin friction predictions for the closure coefficients of each model while Table 5.2 does the same for the momentum thickness Reynolds number. Table 5.1 shows that κ and σ are the largest contributors to the output uncertainty using the SA turbulence model. Likewise,

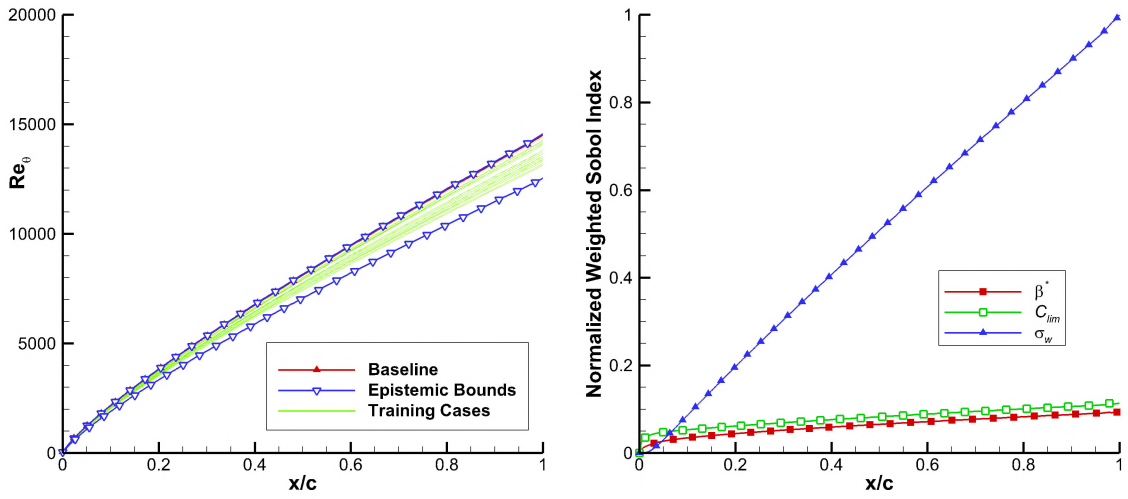

(a) Re_θ versus x/c.

(b) NWSI for Re_θ versus x.

Figure 5.5. Momentum thickness Reynolds number results for 2DZP (W2006 model).

the largest contributor to the W2006 model uncertainty is σ_w because of its contribution over the majority of the chord. The largest source of uncertainty in the SST model for the skin friction prediction is β^* which is clearly evident in Figure 5.7b. Table 5.2 shows that the most significant source of uncertainty in Re_θ using the SA turbulence model is κ. The coefficiant, σ_w, provides the most uncertainty in Re_θ predicted from the W2006 model. Finally, the most significant source of Re_θ uncertainty using the SST turbulence model is β^*. The results from this NIWSI study matches the qualitative assessment which gives validity to this novel approach.

Figure 5.10 shows the NIWSI for the u^+ results from each model. Figure 5.10a shows that the coefficient, κ, from the SA turbulence model is the largest contributor to the uncertainty in u^+. Likewise, Figure 5.10b shows that σ_w provides the most u^+ uncertainty in the W2006 model over the majority of the chord and even shows that uncertainty at the leading edge comes from C_{lim}. Finally, Figure 5.10c shows that the uncertainty in β^* contributes most to the uncertainty in u^+ using the SST turbulence model. Comparison of

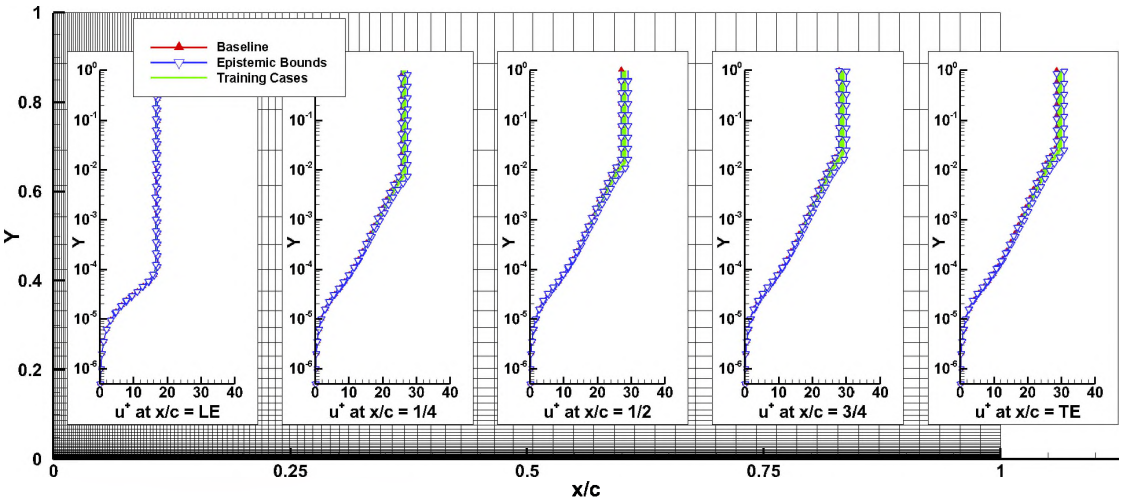

(a) u^+ versus y along the chord.

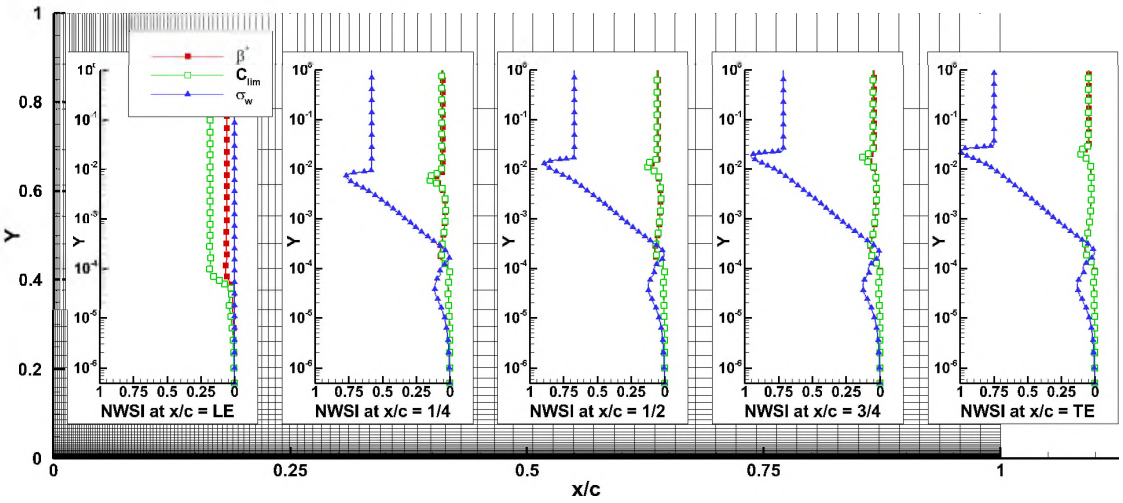

(b) NWSI for u^+ versus y along the chord.

Figure 5.6. $\boldsymbol{u^+}$ results for 2DZP (W2006 model).

these metrics with the qualitative assessments made earlier for the skin friction, momentum thickness Reynolds number, and u^+ finds complete agreement for the coefficients identified as the main sources of output uncertainty.

5.1.2. 2D NASA Wall-Mounted Hump Case. The second case investigated is the 2DWMH case. Polynomial response surfaces were generated at each axial location from $x/c \in [0.6, 2.0]$, and normalized weighted Sobol indices of each of the turbulence model closure coefficients were calculated at each location. The minimum and maximum values

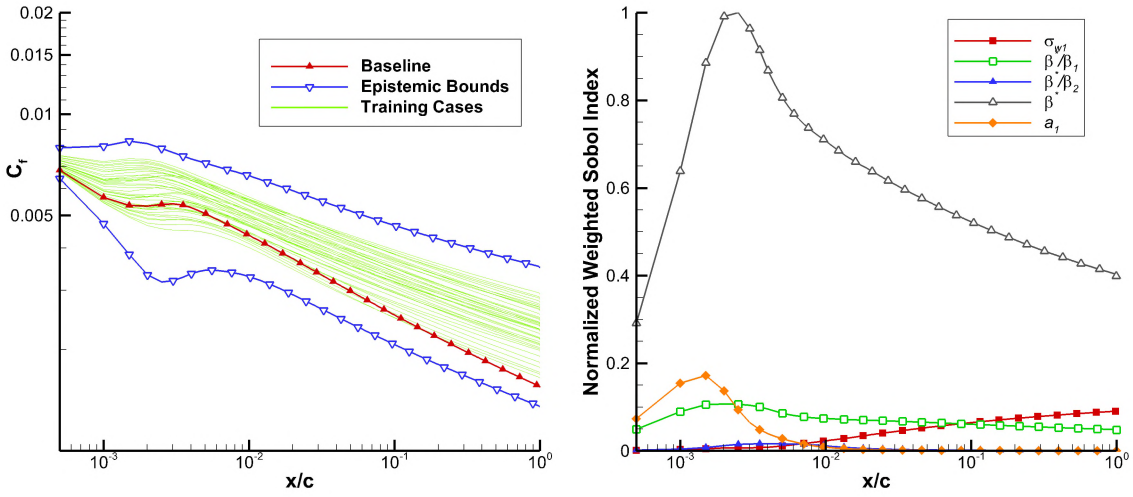

(a) C_f versus x/c. (b) NWSI for C_f versus x/c.

Figure 5.7. Skin friction coefficient results for 2DZP (SST model).

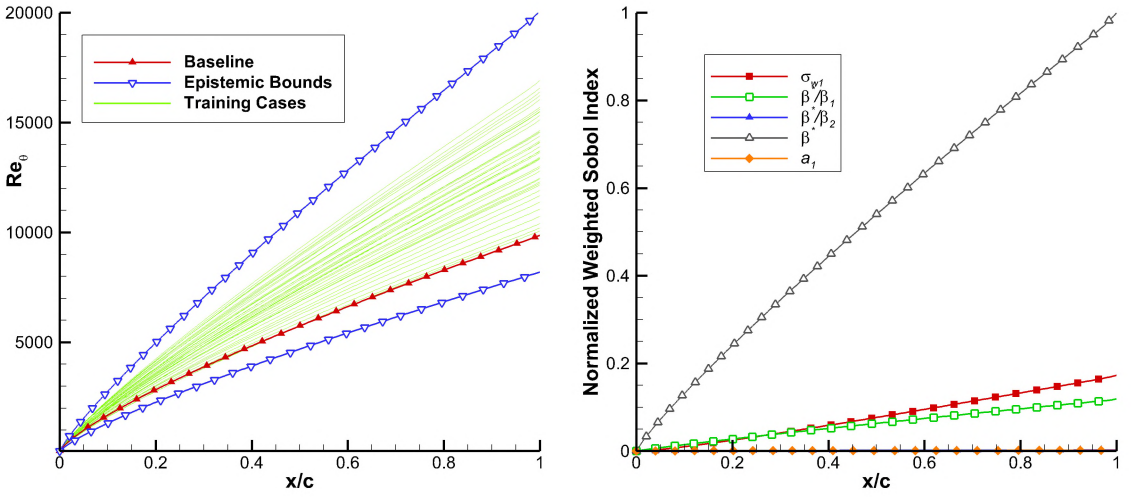

(a) Re_θ versus x/c. (b) NWSI for Re_θ versus x.

Figure 5.8. Momentum thickness Reynolds number results for 2DZP (SST model).

of C_f and C_p were determined from the response surfaces. Plots of C_f and C_p versus x/c contains data for the baseline case, the UQ training cases, the epistemic bounds, and the experimental data from Greenblatt et al [31, 32, 33] in the separated flow region. The analysis of the results for the attached region can be found in Erb and Hosder [48].

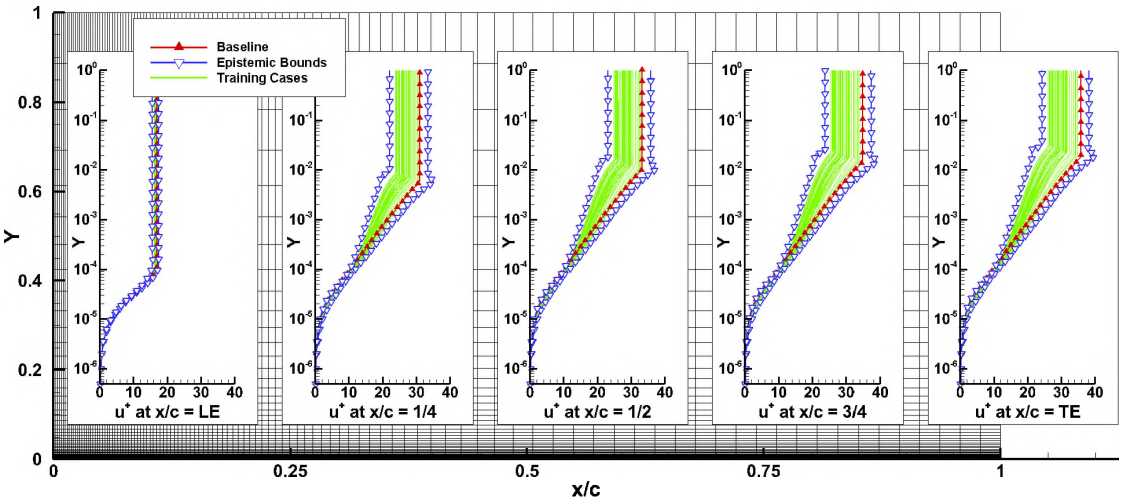

(a) u^+ versus y along the chord.

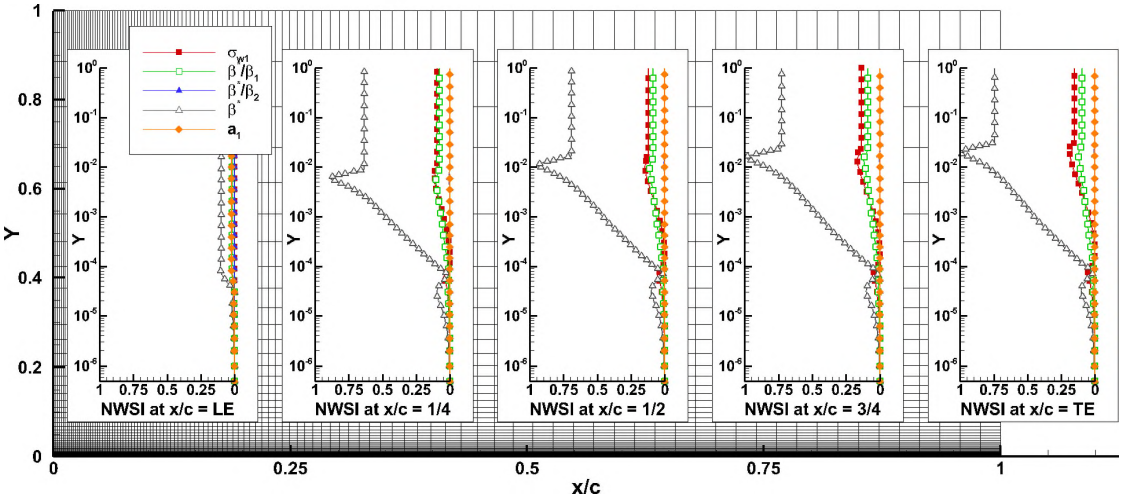

(b) NWSI for u^+ versus y along the chord.

Figure 5.9. $\boldsymbol{u^+}$ results for 2DZP (SST model).

Figures 5.11a and 5.11b present the uncertainty in C_f and the associated NWSI information for the separated region of the flow using the SA turbulence. The model underpredicts the skin friction near the reattachment region, and the uncertainty of the closure coefficients does not adequately capture this behavior. The largest contributions to the uncertainty in this flow region are σ and κ with a spike from c_{w2} at the start of separation and one from c_{w3} near the reattachment region. Figures 5.12a and 5.12b show that the SA model alternates between underpredicting and overpredicting C_p in the separated

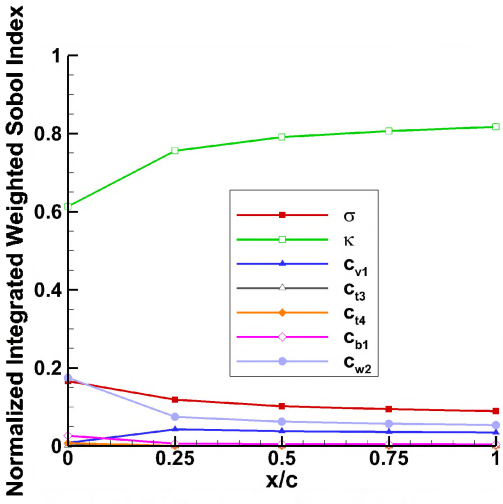

(a) NIWSI for u^+ (SA model).

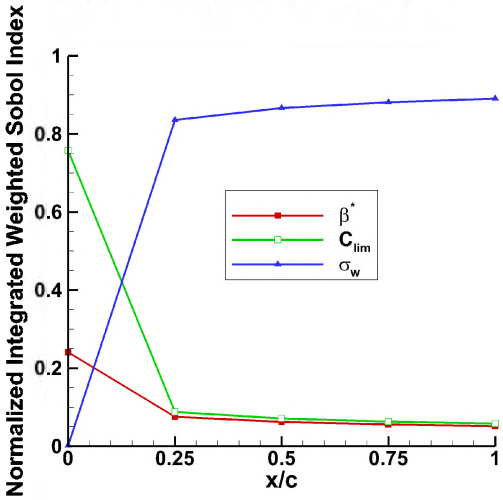

(b) NIWSI for u^+ (W2006 model).

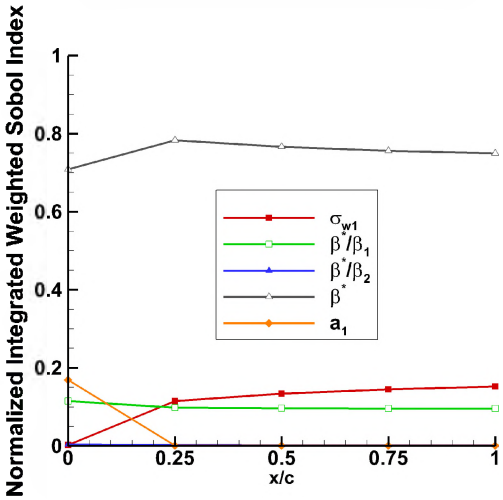

(c) NIWSI for u^+ (SST model).

Figure 5.10. Normalized integrated weighted Sobol index for u^+ results across flat plate.

Table 5.1. Normalized integrated weighted Sobol index for 2DZP skin friction results.

SA Model	NIWSI	W2006 Model	NIWSI	SST Model	NIWSI
σ	0.1305^{II}	β^*	0.0816^{III}	σ_{w1}	0.1355^{II}
κ	0.7441^{I}	C_{lim}	0.1071^{II}	β^*/β_1	0.0913^{III}
c_{v1}	0.0424^{IV}	σ_w	0.8112^{I}	β^*/β_2	0.0019^{IV}
c_{t3}	$3.30\text{E-}05^{VI}$			β^*	0.7692^{I}
c_{t4}	$2.26\text{E-}05^{VII}$			a_1	0.0019^{V}
c_{b1}	0.0066^{V}				
c_{w2}	0.0762^{III}				

I-VII denotes ranking of significance for each model

Table 5.2. Normalized integrated weighted Sobol index for 2DZP momentum thickness Reynolds number results.

SA Model	NIWSI	W2006 Model	NIWSI	SST Model	NIWSI
σ	0.1489^{II}	β^*	0.0980^{III}	σ_{w1}	0.1175^{II}
κ	0.7109^{I}	C_{lim}	0.1256^{II}	β^*/β_1	0.0923^{III}
c_{v1}	0.0464^{IV}	σ_w	0.7764^{I}	β^*/β_2	0.0022^{IV}
c_{t3}	$3.47\text{E-}05^{VI}$			β^*	0.7863^{I}
c_{t4}	$1.62\text{E-}05^{VII}$			a_1	0.0017^{V}
c_{b1}	0.0074^{V}				
c_{w2}	0.0863^{III}				

I-VII denotes ranking of significance for each model

region of the flow. The epistemic bounds of the coefficient uncertainties do not adequately capture the experimental data either. In the separation bubble region, the coefficients that contribute most to the uncertainty are σ, κ, and c_{w2}. The coefficients, c_{b1}, along with the aforementioned c_{w2}, appear to contribute most to the uncertainty in the reattachment region.

The evolution of u/U_∞ uncertainty versus y/c at various x/c locations inside the separation bubble was also investigated. Figure 5.13a presents the experimental data and epistemic uncertainty bounds of u/U_∞ at locations along the separation bubble while Figure 5.13b presents the NWSIs of the closure coefficients at these locations. The closure coefficients that contribute most to the uncertainty are σ, κ, and c_{w2}. The location where

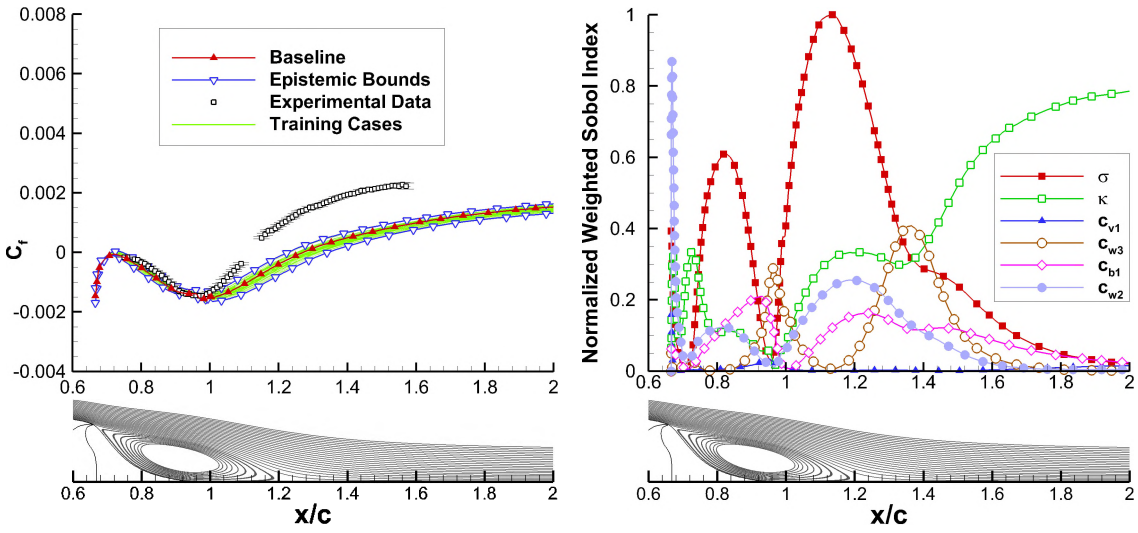

(a) Separated region C_f distribution.

(b) Separated region NWSI for C_f.

Figure 5.11. Skin friction coefficient results for 2DWMH (SA model).

the SA model begins to underpredict u/U_∞ starts with the onset of the separation region. This underprediction can be seen to begin at $x/c = 0.80$, near $y/c = 0.05$ and continues to grow even beyond the reattachment point.

The ranking of SA model closure coefficients' contributions to the uncertainty for the drag coefficient and separation bubble size is shown in Table 5.3. The drag coefficient uncertainty is dominated by κ with σ being the second largest contributing source. The roles are reversed when analyzing the uncertainty in the separation bubble size where σ is the largest contributing source while κ being the second ranked source of uncertainty.

Next, the results for the W2006 model are presented. In Figures 5.14a and 5.14b, the W2006 turbulence model begins to underpredict the skin friction coefficient in the separation bubble region. The largest source of skin friction uncertainty comes from C_{lim} with σ_w and β^* following closely behind. The skin friction results do not appear to be sensitive to the uncertainty in σ_k. In Figures 5.15a and 5.15b, the W2006 model alternates between underpredicting and overpredicting C_p in the separated region of the flow. The epistemic bounds of the coefficient uncertainties do not adequately capture the experimental

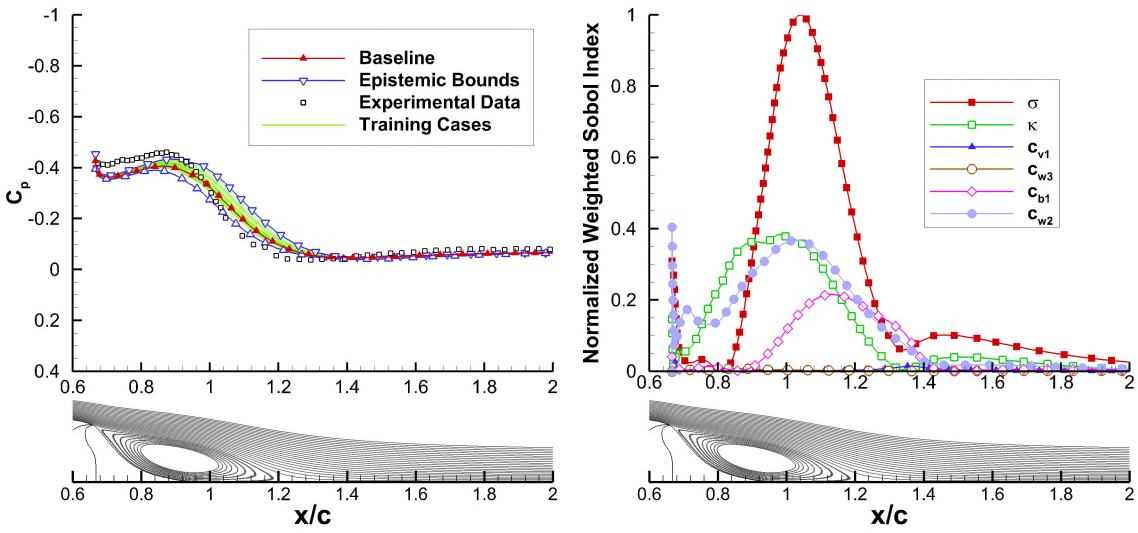

(a) Separated region C_p distribution.

(b) Separated region NWSI for C_p.

Figure 5.12. Pressure coefficient results for 2DWMH (SA model).

Table 5.3. Sobol indices of closure coefficients for C_D and separation bubble size for 2DWMH using the SA model.

Coefficient	C_D	Separation Bubble Size
σ	0.2204^{II}	0.4996^{I}
κ	0.6775^{I}	0.1751^{II}
c_{v1}	0.0617^{III}	0.0370^{VI}
c_{w3}	0.0007^{VI}	0.0915^{V}
c_{b1}	0.0327^{IV}	0.0983^{IV}
c_{w2}	0.0069^{V}	0.0984^{III}

note: I-VI denotes ranking of significance

data. The coefficients that contribute the significant portion of uncertainty are C_{lim}, σ_w and β^*. Much like the skin friction prediction, the pressure coefficient appears to be insensitive to the uncertainty in σ_k.

Figure 5.16a presents the experimental data and epistemic uncertainty bounds of u/U_∞ at locations along the separation bubble while Figure 5.16b presents the NWSIs of the closure coefficients at these locations. As seen in these Figures, the closure coefficients that contribute most to the solution uncertainty inside the separation bubble are C_{lim} and

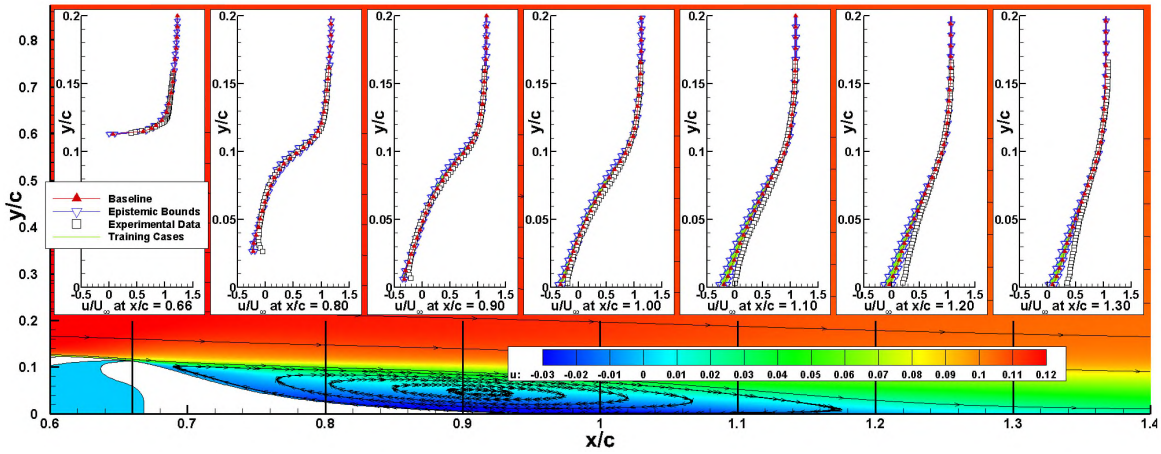

(a) u/U_∞ versus y along separated flow region.

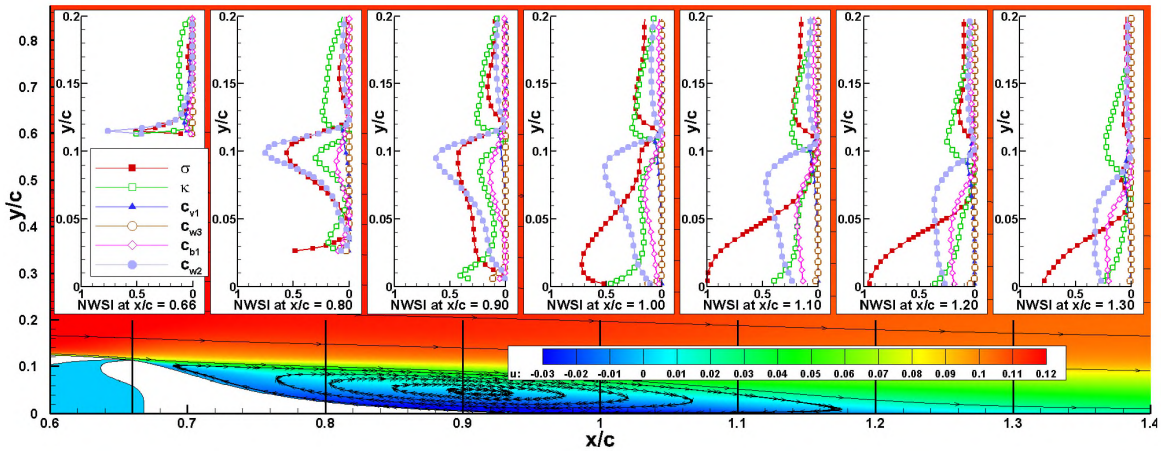

(b) NWSI for u/U_∞ versus y along separated flow region.

Figure 5.13. Evolution of $\boldsymbol{u/U_\infty}$ uncertainty vs. $\boldsymbol{y}$ inside separation bubble for 2DWMH (SA model).

σ_w. The contribution from β^* grows as the flow progresses through the separation bubble. Despite a relatively large epistemic interval for the solution of u/U_∞ the W2006 model fails to bound the experimental data for a large portion of the separated flow region. This is in contrast to the SA model with tighter epistemic uncertainty bounds which is closer to the experimental data.

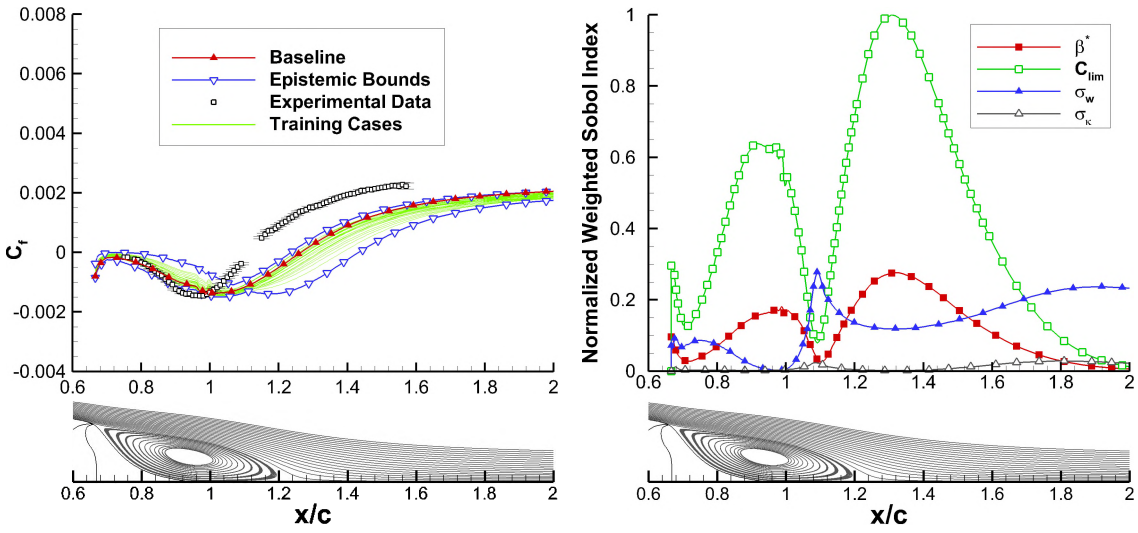

(a) Separated region C_f distribution.

(b) Separated region NWSI for C_f.

Figure 5.14. Skin friction coefficient results for 2DWMH (W2006 model).

Table 5.4 presents the sensitivity results for the drag coefficient and separation bubble size when using the W2006 turbulence model. The table shows that σ_w and C_{lim} share nearly equal contributions as the top sources for drag coefficient uncertainty; the third largest contributor is β^*. The top source of separation bubble size uncertainty is C_{lim} with β^* being the second largest contributor.

The results from the SST model are investigated in a manner similar to the previous models. Figures. 5.17a and 5.17b show that, given the uncertainties in the SST turbulence model, the model captures the experimental skin friction results fairly well. The experi-

Table 5.4. Sobol indices of closure coefficients for C_D and separation bubble size for 2DWMH using the W2006 model.

Coefficient	C_D	Separation Bubble Size
β^*	0.1227^{III}	0.2576^{II}
C_{lim}	0.4374^{II}	0.6645^{I}
σ_w	0.4390^{I}	0.0737^{III}
σ_k	0.0009^{IV}	0.0042^{IV}

note: I-IV denotes ranking of significance

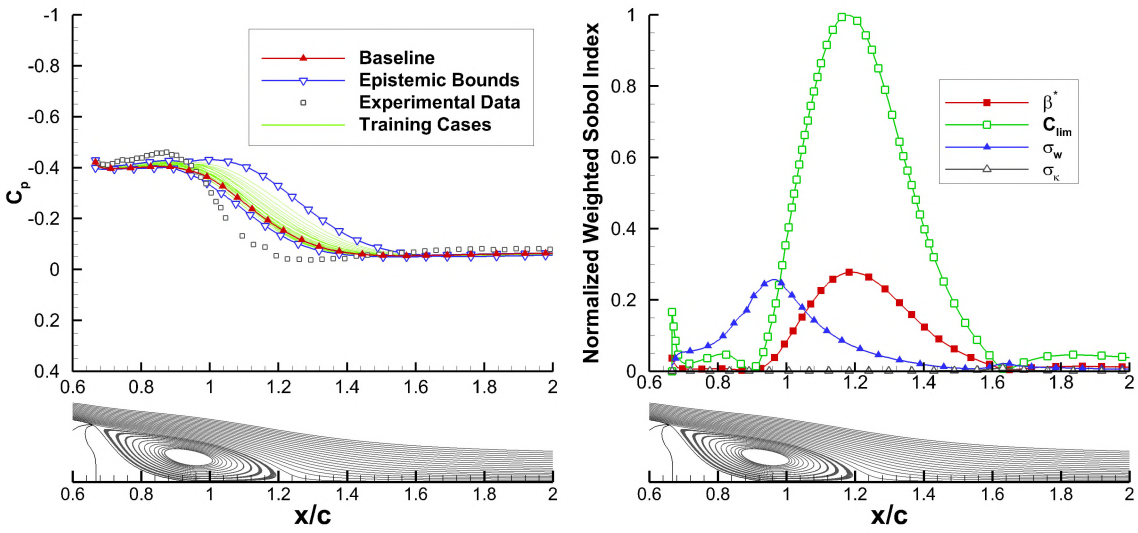

(a) Separated region C_p distribution.

(b) Separated region NWSI for C_p.

Figure 5.15. Pressure coefficient results for 2DWMH (W2006 model).

mental data is bounded by the epistemic uncertainties throughout the domain of interest. These bounds, however, are larger than the bounds from the SA and W2006 models. The coefficients that contribute to these large bounds are σ_{w2}, κ, and a_1. To a lesser extent, β^*/β_1 and σ_{w1} also contribute to the output uncertainty. The pressure coefficient results can be seen in Figures 5.18a and 5.18b. As with the skin friction coefficient, the pressure coefficient results are captured within the epistemic bounds of uncertainty in the domain of interest. Consistent with the uncertainty in skin friction coefficient and the observations made for the 2DZP case, these bounds are larger in magnitude than the results of the SA and W2006 models. The coefficients that contribute to these large bounds are a_1, κ, and σ_{w2}. Like the skin friction results, β^*/β_1 and σ_{w1} also contribute to the output uncertainty but at a reduced level.

Figure 5.19a presents the experimental data and epistemic uncertainty bounds of u/U_∞ at locations along the separation bubble while Figure 5.19b presents the NWSIs of the SST model closure coefficients at these locations. As seen in the figures, the closure coefficients that contribute most to the solution uncertainty inside the separation bubble are

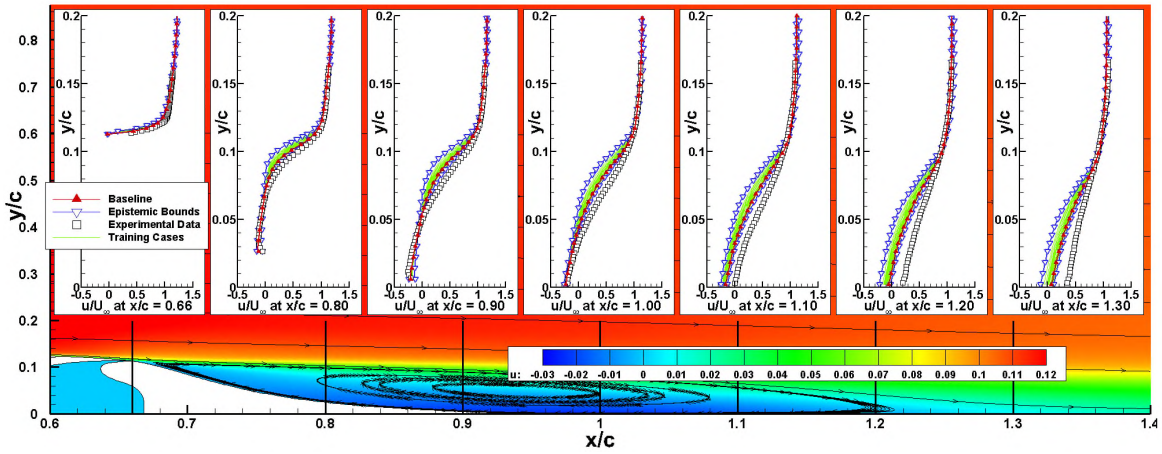

(a) u/U_∞ versus y along separated flow region.

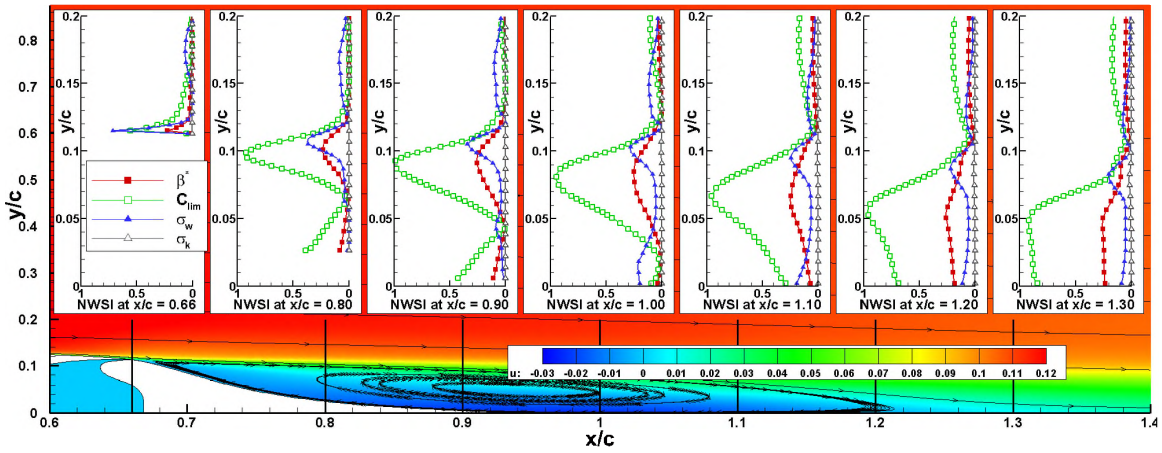

(b) NWSI for u/U_∞ versus y along separated flow region.

Figure 5.16. Evolution of $\boldsymbol{u/U_\infty}$ uncertainty vs. $\boldsymbol{y}$ inside separation bubble for 2DWMH (W2006 model).

a_1, κ, and σ_{w2}. σ_{w1} is seen to be the largest contributor at the start of the separation bubble but its contribution is reduced downstream. The epistemic interval for the solution of u/U_∞ using the SST model bounds the experimental data fairly well inside the separated flow region. The model only slightly underpredicts the data near the wall at the station where $x/c = 1.30$.

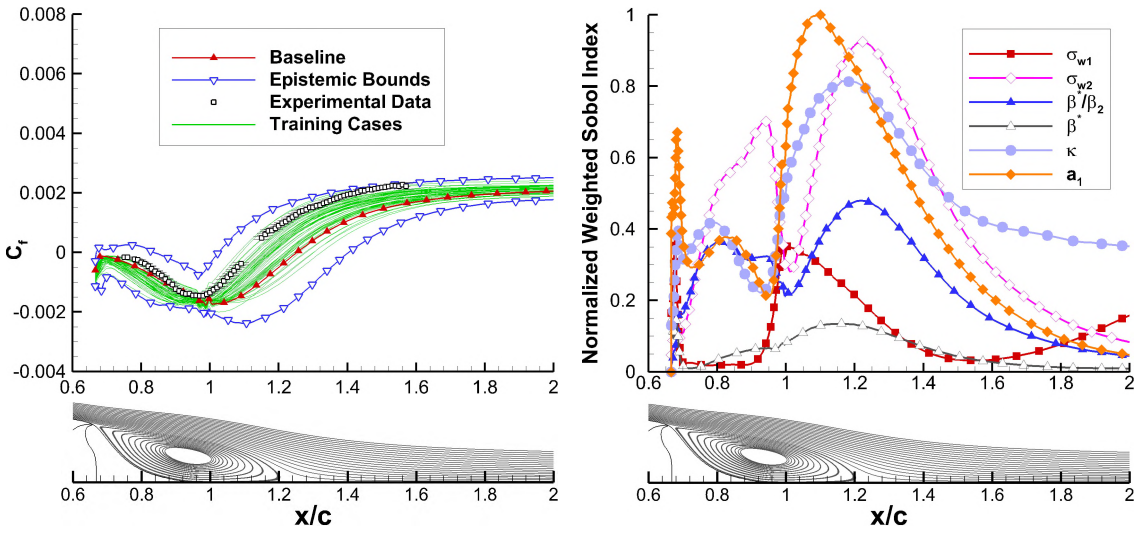

(a) Separated region C_f distribution.

(b) Separated region NWSI for C_f.

Figure 5.17. Skin friction coefficient results for 2DWMH (SST model).

The contribution to the SST model output uncertainty in drag coefficient and separation bubble size measurements are shown in Table 5.5. The largest contributor to drag coefficient uncertainty is σ_{w2} with κ trailing closely behind. The closure coefficients β^*/β_1 and σ_{w1} also provide a notable amount of uncertainty. The top source of uncertainty in the separation bubble size is nearly identical between σ_{w2}, a_1, and κ.

Table 5.5. Sobol indices of closure coefficients for C_D and separation bubble size for 2DWMH using the SST model.

Coefficient	C_D	Separation Bubble Size
σ_{w1}	0.1257^{IV}	0.0829^{V}
σ_{w2}	0.3394^{I}	0.2519^{I}
β^*/β_2	0.2027^{III}	0.1346^{IV}
β^*	0.0033^{VI}	0.0364^{VI}
κ	0.3049^{II}	0.2466^{III}
a_1	0.0239^{V}	0.2476^{II}

note: I-VI denotes ranking of significance

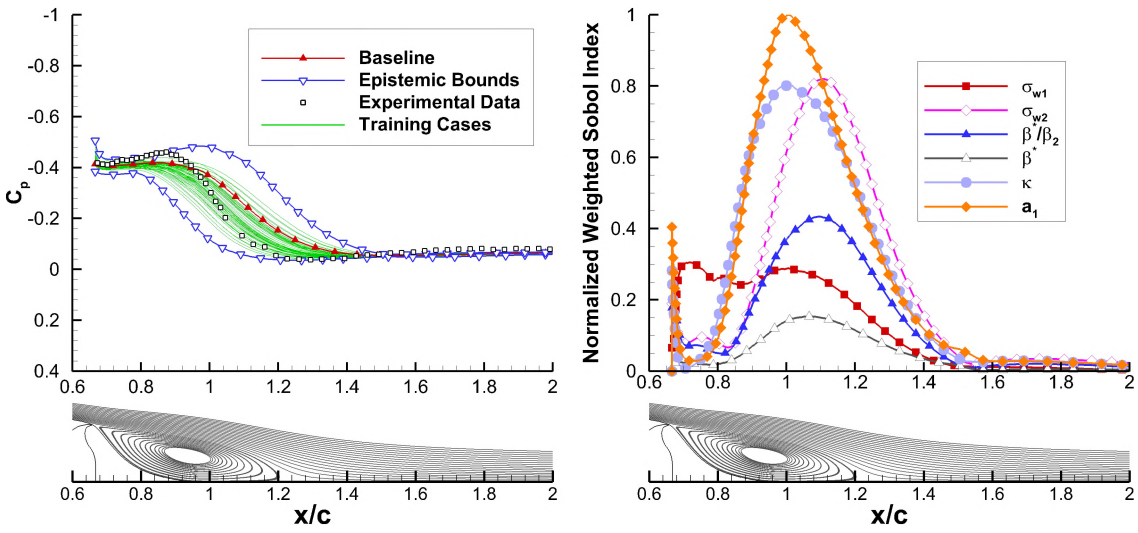

(a) Separated region C_p distribution.

(b) Separated region NWSI for C_p.

Figure 5.18. Pressure coefficient results for 2DWMH (SST model).

Similar to the quantitative analyses made for the 2DZP case, a quantitative assessment of the level of contribution of each coefficient to the output uncertainty was performed for the 2DWMH case. The NIWSI of each coefficient was determined for different QoIs. Tables 5.6 and 5.7 shows the NIWSI for the skin friction and pressure coefficients, respectively. The first set of columns shows the ranking from the SA turbulence model. It can be clearly seen that the κ and σ are the largest sources of skin friction coefficient uncertainty while the pressure coefficient uncertainty adds c_{w2} to the list of significant sources. The main sources of both skin friction and pressure coefficient uncertainty from the W2006 model come from C_{lim}, σ_w, and β^*. Lastly, the uncertainty of the SST model predictions of both skin friction and pressure coefficients come from κ, σ_{w2}, and a_1. The identified sources of uncertainty for the three models using the NIWSI metric is consistent with the qualitative assessment made earlier.

A similar quantitative comparison for the flow field uncertainty is performed by calculating the NIWSI for the coefficients of each turbulence model and is shown in Figure 5.20. Earlier it was determined that σ, κ, and c_{w2} contribute the most to the velocity

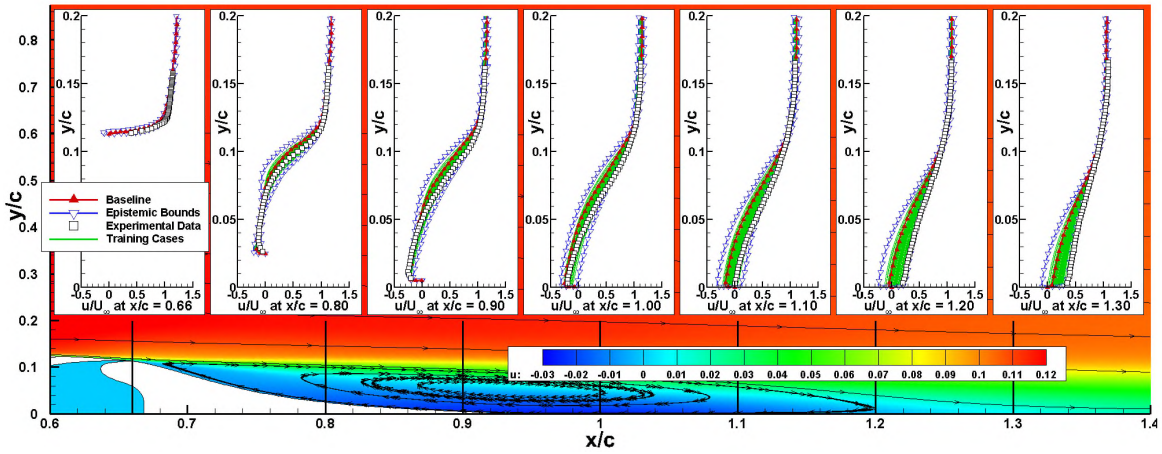

(a) u/U_∞ versus y along separated flow region.

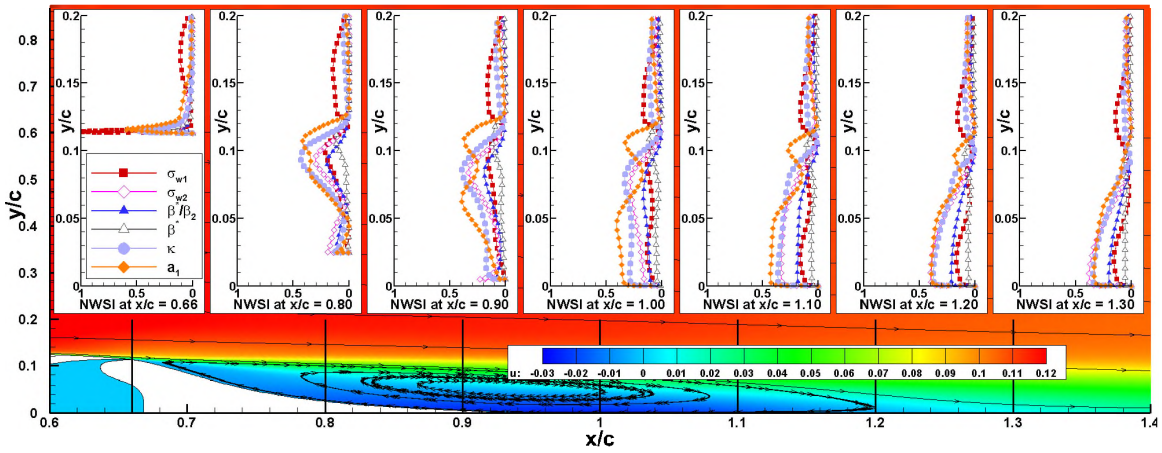

(b) NWSI for u/U_∞ versus y along separated flow region.

Figure 5.19. Evolution of $\boldsymbol{u/U_\infty}$ uncertainty vs. $\boldsymbol{y}$ inside separation bubble for 2DWMH (SST Model).

uncertainty. Figure 5.20a confirms that these three closure coefficients are the top contributors. The W2006 model closure coefficients that are the most significant to the velocity uncertainty are C_{lim}, σ_w, and β^*, as seen in Figure 5.20b. Lastly, Figure 5.20c shows that the uncertainty in the velocity prediction of the SST model is most influenced by a_1, κ, σ_{w1}, and σ_{w2}. These findings confirm the qualitative assessment made earlier.

Table 5.6. Normalized integrated weighted Sobol index for 2DWMH skin friction results.

SA Model	NIWSI	W2006 Model	NIWSI	SST Model	NIWSI
σ	0.3262^{II}	β^*	0.1679^{III}	σ_{w1}	0.0647^{V}
κ	0.4059^{I}	C_{lim}	0.6103^{I}	σ_{w2}	0.2525^{II}
c_{v1}	0.0066^{VI}	σ_w	0.2046^{II}	β^*/β_2	0.1413^{IV}
c_{w3}	0.0850^{V}	σ_k	0.0171^{IV}	β^*	0.0328^{VI}
c_{b1}	0.0880^{IV}			κ	0.2786^{I}
c_{w2}	0.0884^{III}			a_1	0.2301^{III}

I-VI denotes ranking of significance

Table 5.7. Normalized integrated weighted Sobol index for 2DWMH pressure coefficient results.

SA Model	NIWSI	W2006 Model	NIWSI	SST Model	NIWSI
σ	0.4302^{I}	β^*	0.1853^{II}	σ_{w1}	0.1146^{V}
κ	0.2243^{III}	C_{lim}	0.6619^{I}	σ_{w2}	0.2209^{III}
c_{v1}	0.0067^{V}	σ_w	0.1495^{III}	β^*/β_2	0.1281^{IV}
c_{w3}	0.0040^{VI}	σ_k	0.0032^{IV}	β^*	0.0451^{VI}
c_{b1}	0.1054^{IV}			κ	0.2365^{II}
c_{w2}	0.2294^{II}			a_1	0.2548^{I}

I-VI denotes ranking of significance

5.1.3. Axisymmetric Shock Wave Boundary Layer Interaction Case. The third case included in this dissertation is an ASWBLI problem. This section will present selected results of the uncertainty quantification and sensitivity analysis performed on shock wave turbulent boundary layer interaction over the axisymmetric cylinder/flare configuration. Section 5.1.3.1 will present the uncertainty analysis results for selected flow field quantities of interest. Section 5.1.3.2 will discuss the uncertainty on surface quantities of interest along with point and integrated quantities. The CFD results of the selected QoIs are compared to the experimental results from Kussoy and Horstman [34] when available.

5.1.3.1. Flow field uncertainty analysis. Stochastic response surfaces of the flow field quantities interest are generated normal to the cylinder center line at each of the four locations investigated in the experiment. These locations are $S = \{-6, 5.5, 10.3, 15.5\}$ cm

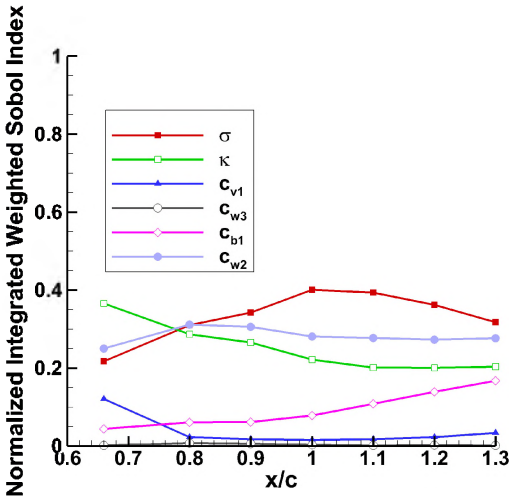

(a) NIWSI for u/U_∞ (SA model).

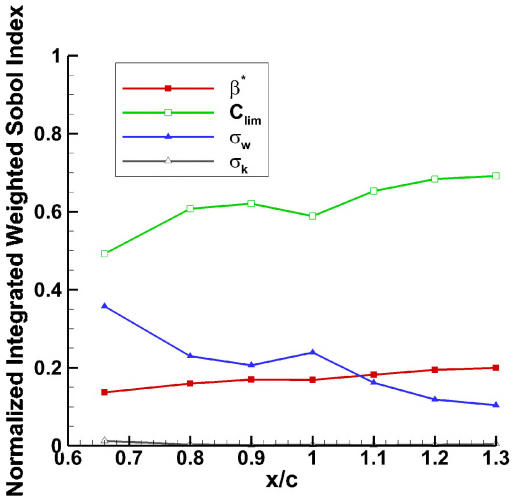

(b) NIWSI for u/U_∞ (W2006 model).

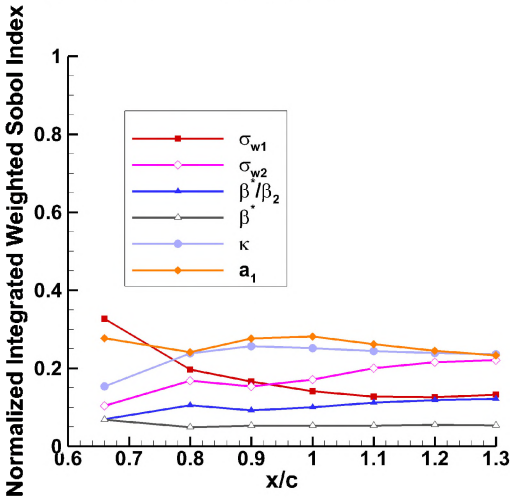

(c) NIWSI for u/U_∞ (SST model).

Figure 5.20. Normalized integrated weighted Sobol index across 2DWMH.

where the location $S = 0$ cm corresponds to the vertex of the flare. The quantity, S, is then measured along the surface of the wall. The normalizing quantity, marked with the subscript ∞ is taken upstream of the flare at $S = -6$ cm and outside of the boundary layer.

The selected quantity of interest presented for the flow station investigation is the static density ratio ρ/ρ_∞. For brevity, only this single QoI is presented in this dissertation. Other QoIs that were examined while studying this problem were the Mach number, the normalized velocity, u/U_∞, the static pressure ratio P/P_∞, and the static temperature ratio T/T_∞. For the results of these QoI please refer to the papers from Erb and Hosder [14, 49, 50].

The ρ/ρ_∞ results for the SA model can be seen in Figure 5.21, which includes the baseline density profiles obtained with the nominal values of the closure coefficients, the epistemic uncertainty bounds, the training data used in the creation of the stochastic response surfaces and the experimental data at each station. The same figure also includes the NWSI profiles showing the contribution of each coefficient to the density ratio uncertainty at each station. The SA turbulence model tends to underpredict the density near the wall in the separated shear region. The model then transitions to overpredicting and back to underpredicting as the density is measured outward from the cylinder centerline and downstream of the compression corner. The NWSI plots show that the location with the most uncertainty in density ratio is the station immediately after the shock in the reattachment compression fan region ($S = 5.5$ cm). The coefficient, σ, contributes most of the uncertainty at this location with κ and c_{w2} contributing approximately 38% and 28% of the uncertainty as σ respectively. A similar trend in the W2006 model results can be seen in Figure 5.22 though the epistemic bounds in the W2006 model are larger when compared to the SA model. The value of C_{lim} at the station immediately after the compression corner and in the reattachment compression fan region provides the largest source of uncertainty while β^* provides approximately 38% as much uncertainty. The coefficient, σ_w, can also be seen providing a significant amount of uncertainty especially in the downstream stations and inside the shear layer. Like the SA and W2006 model predictions, the SST model

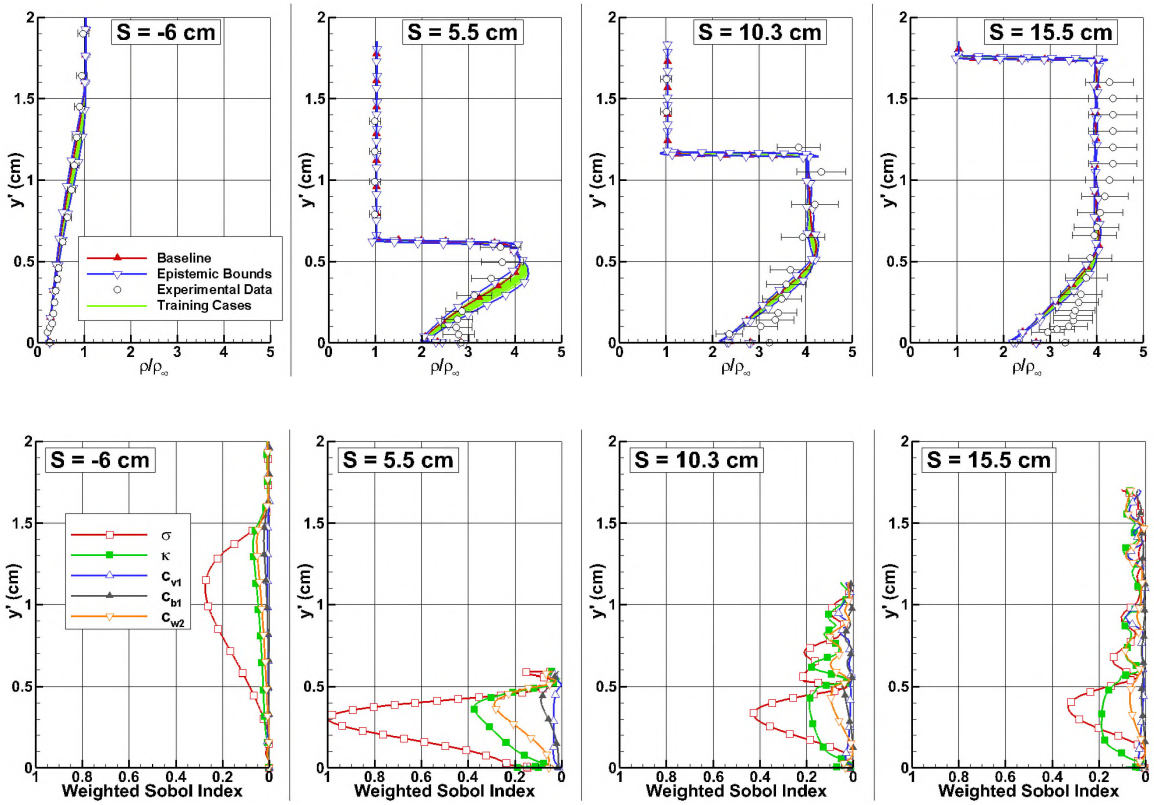

Figure 5.21. Uncertainty (top row) and sensitivity (bottom row) results for the density profiles at four stations for ASWBLI (SA model).

in Figure 5.23 transitions from under, to over, and back to underpredicting the density ratio. The largest regions of uncertainty are located inside the shear layer of the flow. The epistemic uncertainty bounds induced by the SST model constant uncertainties are the largest between the three models studied. Like the previous models, it is located inside the reattachment compression fan at S = 5.5 cm. The closure coefficient that contributes the most to the overall uncertainty in the density result for the SST model is σ_{w1} with κ contributing approximately 40% the amount of σ_{w1}.

Following the qualitative assessment of the NWSI ranking for the static density ratio at each station presented above, an effort was made for quantifying the overall uncertainty of a specific closure coefficient at each measurement station for each model. The goal

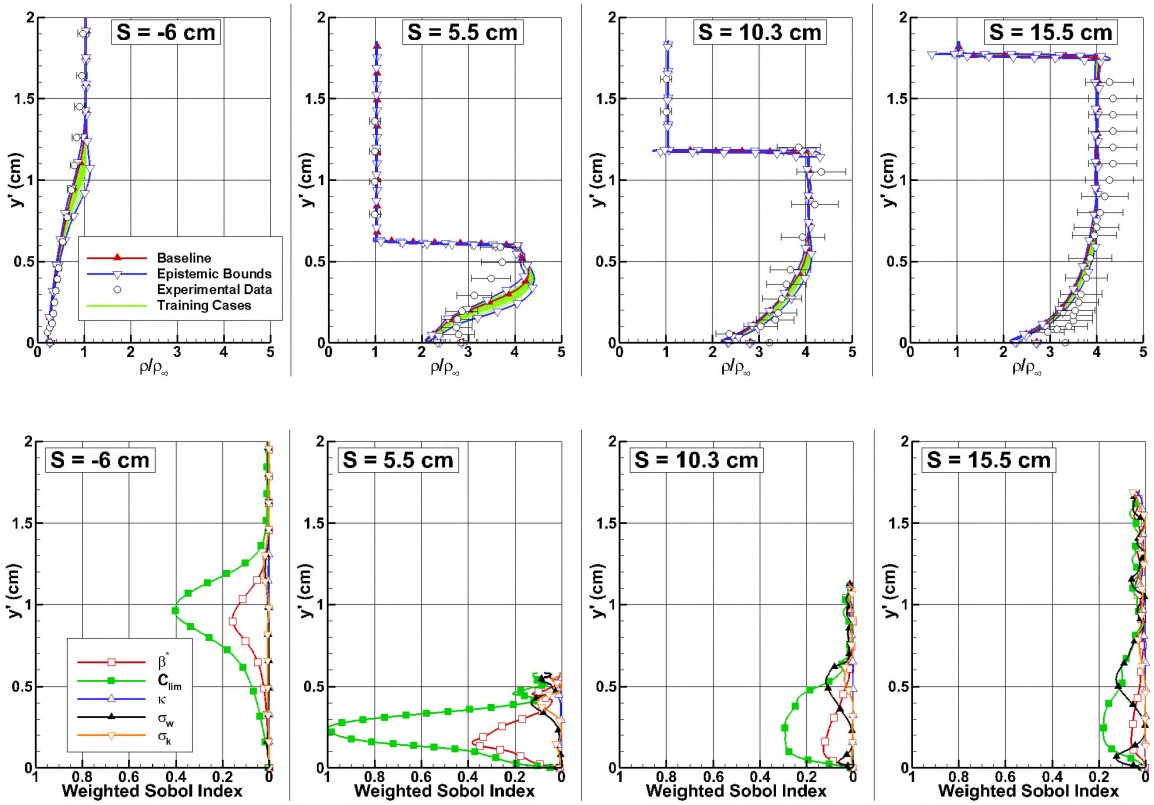

Figure 5.22. Uncertainty (top row) and sensitivity (bottom row) results for the density profiles at four stations for ASWBLI (W2006 model).

was to condense the Sobol index plot into single quantifiable value in order to rank the uncertainty contribution for each of the closure coefficients over a domain of interest. The following NIWSI analysis was performed to rank the contribution of uncertainty from each closure coefficient. In addition to density, the NIWSI distributions for the Mach number and static pressure ratio, P/P_∞, from the Erb and Hosder [49] study are also included in this section to provide a broader understanding into the closure coefficient uncertainty rankings for different flow field variables.

The distribution of NIWSIs for each QoI at each station are presented in Figure 5.24 where stations $\{1, 2, 3, 4\}$ correspond to the measurement stations at $S = \{-6.0, 5.5, 10.3, 15.5\}$ cm respectively. The ranking for the contribution of each closure coefficient to

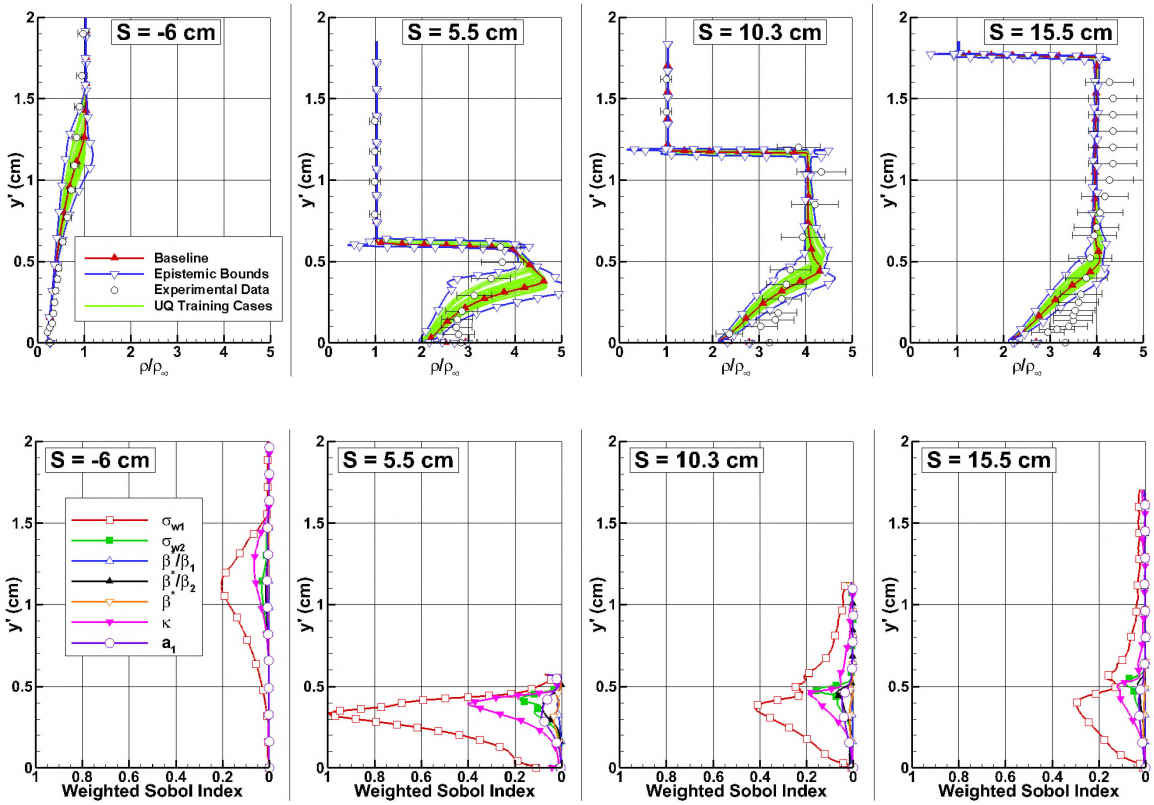

Figure 5.23. Uncertainty (top row) and sensitivity (bottom row) results for the density profiles at four stations for ASWBLI (SST model).

the overall output uncertainty can easily be determined at each measurement station by examining these plots. The SA model closure coefficients responsible for the majority of the solution uncertainty for all flow field variables are σ, κ, and c_{w2}. A comparison between the qualitative estimation of the significance of these Sobol indices performed above is in complete agreement with this quantitative assessment. The significant Sobol indices in the W2006 model are C_{lim}, β^*, and σ_w while the largest contributors to the SST model uncertainty are σ_{w1} and κ. Again, comparing the quantitative analyses of the NIWSI to the qualitative assessment performed with the profile data above shows that the original assessment on the ranking of coefficients was correct.

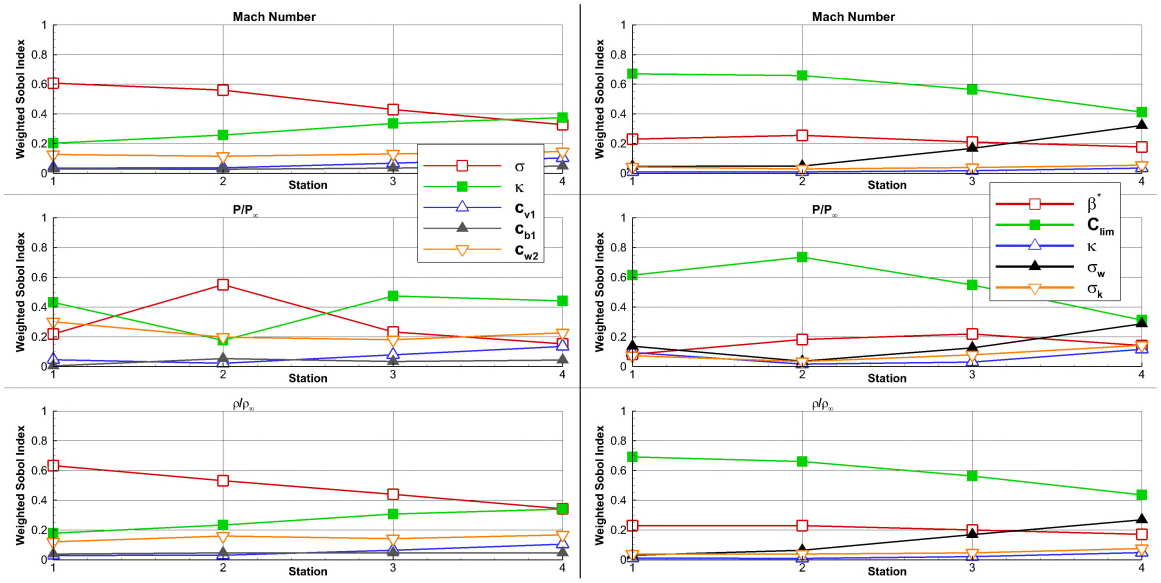

(a) SA turbulence model.

(b) W2006 turbulence model.

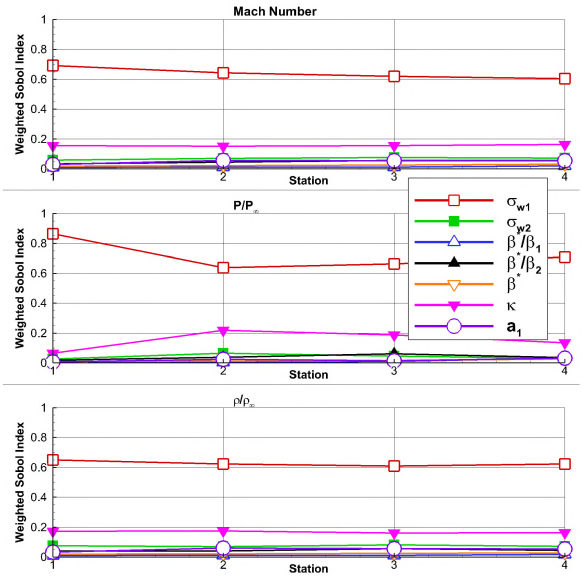

(c) SST turbulence model.

Figure 5.24. Normalized integrated weighted Sobol indices for flow field quantities of interest in the ASWBLI.

Further investigation into the flow field quantities was desired as the four experimental measurement stations do not sufficiently capture the complex physics in the separated flow region at the apex of the flare. In an effort to fully investigate the uncertainty in these

regions of interest, epistemic interval contours for each quantity of interest were created over the full flow field for $S \in \{-6, 10\}$ cm and between the wall and the freestream including the boundary layer and the shock wave.

The results for the Mach number investigation are presented in Figure 5.25. Examining these figures indicates that the SA model predicts a smaller separation bubble just upstream of the compression corner compared to the W2006 and SST models. The SST model predicts the largest separation region between the three. The uncertainties in the coefficients of each model can have a significant impact on the confidence of the solution. The SST model in particular exhibits a large epistemic bound near the edge of the boundary layer which then impacts the shock wave obtained with this model. All three models contain uncertainty at the shock-shock interaction location and continue into the slip line but is largest for the SST model. The uncertainty range in the separation region is also largest in the SST model prediction. An epistemic bound of nearly 2.5 in this region indicates a significant sensitivity of Mach number to the closure coefficient uncertainty inside the separation bubble. This uncertainty is smaller in the W2006 model ($\approx$ 1.3) and the SA model ($\approx$ 0.8) but will still impact the prediction of the Mach number in this region.

The results of the normalized pressure are presented in Figure 5.26. Similar to the Mach number, with the nominal coefficient values, the results are similar for each turbulence model except for the separation bubble size just upstream of the compression corner. The shock wave in the SST model begins slightly upstream of the W2006 model prediction which locates it slightly upstream of the SA model. The real differences are seen when the effects of the model coefficient uncertainties are studied and the epistemic boundaries are investigated. The starting location of the separation compression fan varies significantly in the SST model when compared to the SA and W2006 models. This is in direct comparison to the separation bubble size. Additionally, there is a region of large uncertainty near the wall in the reattachment compression fan region near x = 3-4 cm for all the models. This

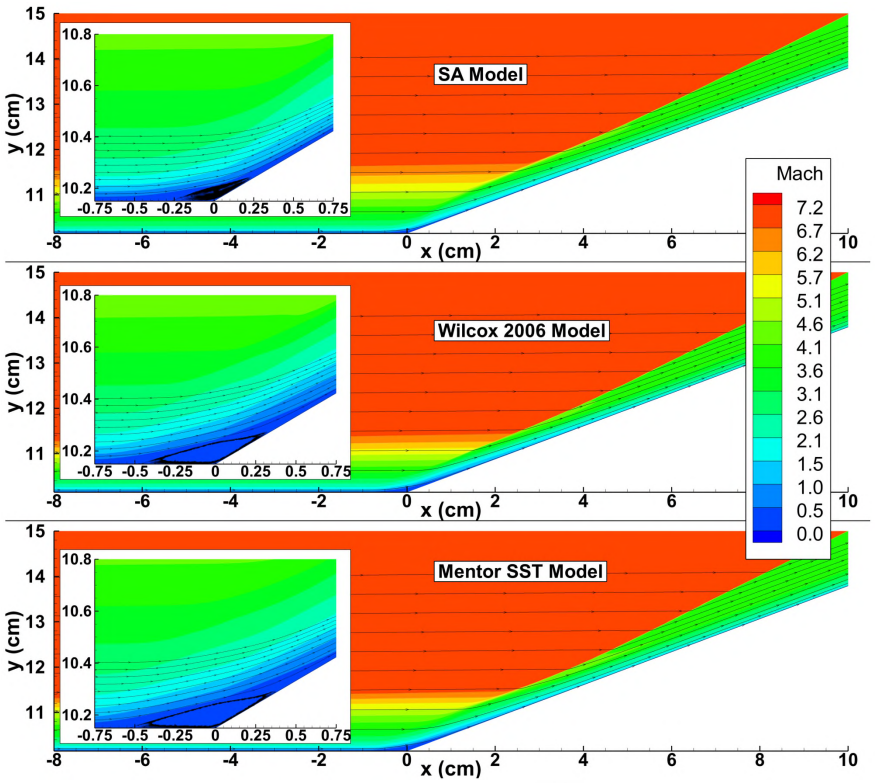

(a) Mach contours for the baseline case.

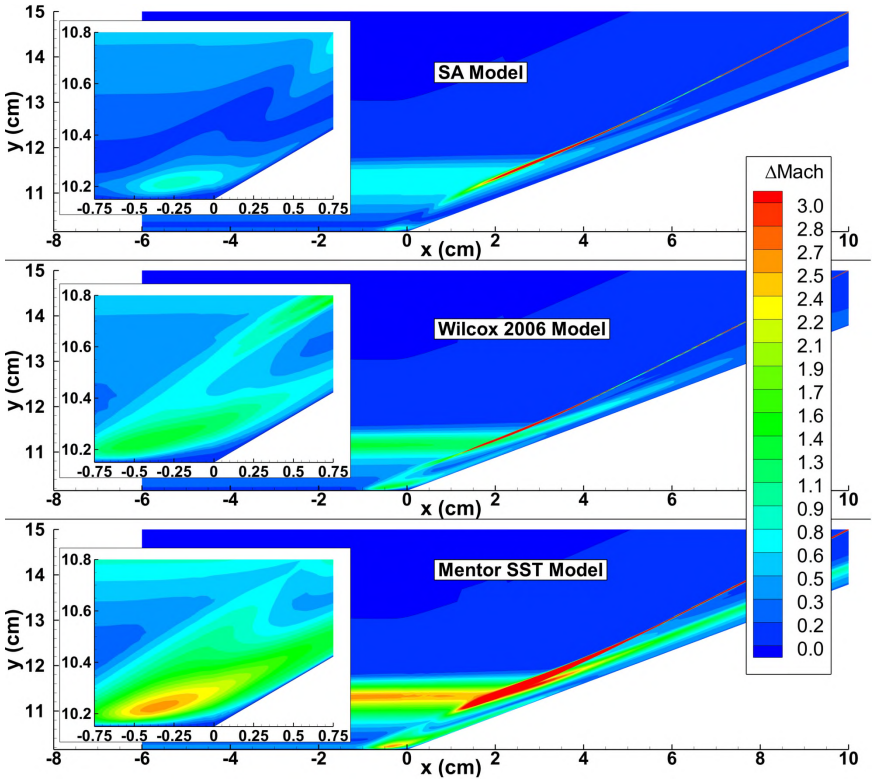

(b) Epistemic interval contours for Mach number.

Figure 5.25. Mach number uncertainty for the full flow field for ASWBLI.

region exhibits an epistemic bound nearly twice as large in the SST model when compared to the SA and W2006 models. The location of this large pocket of uncertainty corresponds to the edge of the freestream boundary layer colliding with the shock wave.

Like the two previous quantities of interest, the density solutions between the three models are similar and can be seen in Figure 5.27a, and the epistemic bound plots are shown in Figure 5.27b. Throughout much of the freestream there exists little difference between the three models. The epistemic bounds in the freestream boundary edge grow from the SA to the W2006 and are largest in the SST model. Additionally, the density uncertainty in the SST model is significantly larger for a significant region of the shock layer. This large uncertain region forms along on the slip line originating from where the incoming boundary layer impacts with the shock wave.

With the sensitivity analysis conducted over the full flow field, the Sobol indices for the closure coefficients of each turbulence model are obtained and used to calculate their individual NWSI. The NWSIs are then plotted as a function of their spatial position. For the sake of brevity, only the most significant closure coefficients for each model have been included in this particular study. Figures 5.28 - 5.33 display the NWSI of the significant closure coefficients for each quantity of interest and for each model over the full flow field.

In Figures 5.28 and 5.29 the NWSI distribution of σ and κ coefficients of the SA Model are presented, respectively. The primary location of the uncertainty in the Mach number is the edge region of the boundary layer upstream of the shock and is primarily due to σ with κ providing approximately 25% of the uncertainty as σ. Additionally, the value of σ provides the most uncertainty in the separation bubble region while exhibiting approximately 75% of the maximum uncertainty in this region. The value of σ also provides the most uncertainty in the static pressure and density ratios. The most uncertainty in P/P_∞ is in the reattachment compression fan region while the origin of the shock accounts for

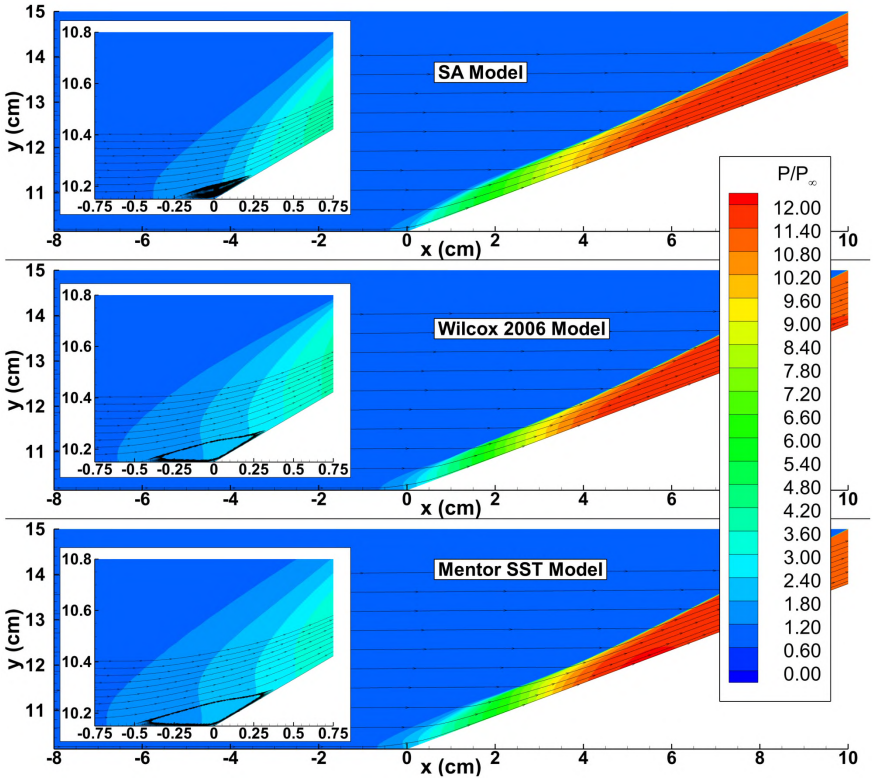

(a) Pressure contours for the baseline case.

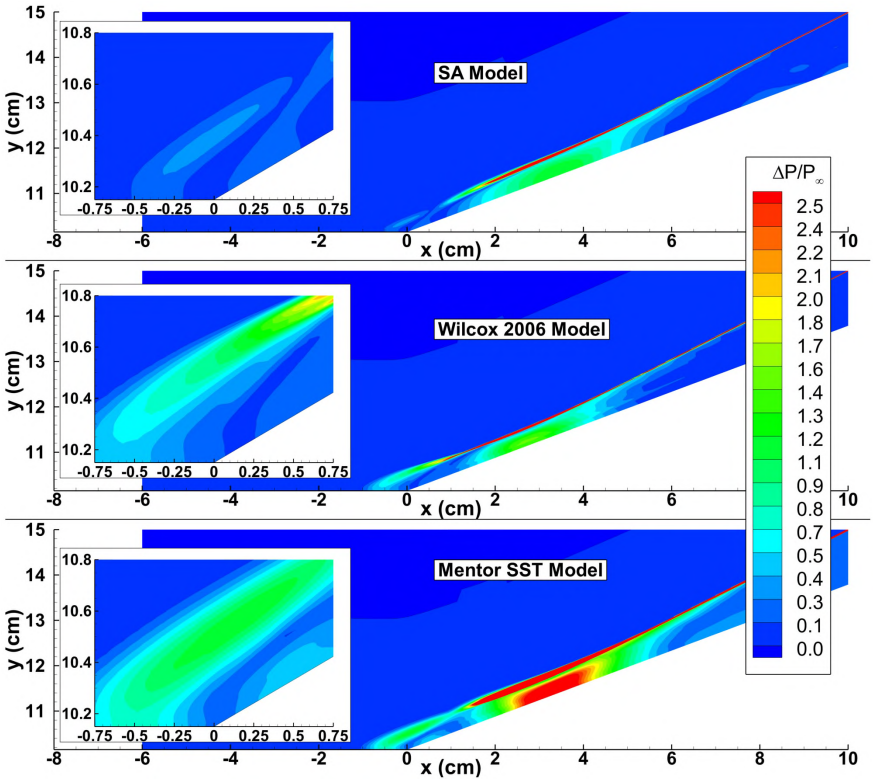

(b) Epistemic interval contours for pressure.

Figure 5.26. Pressure ratio uncertainty for the full flow field for ASWBLI.

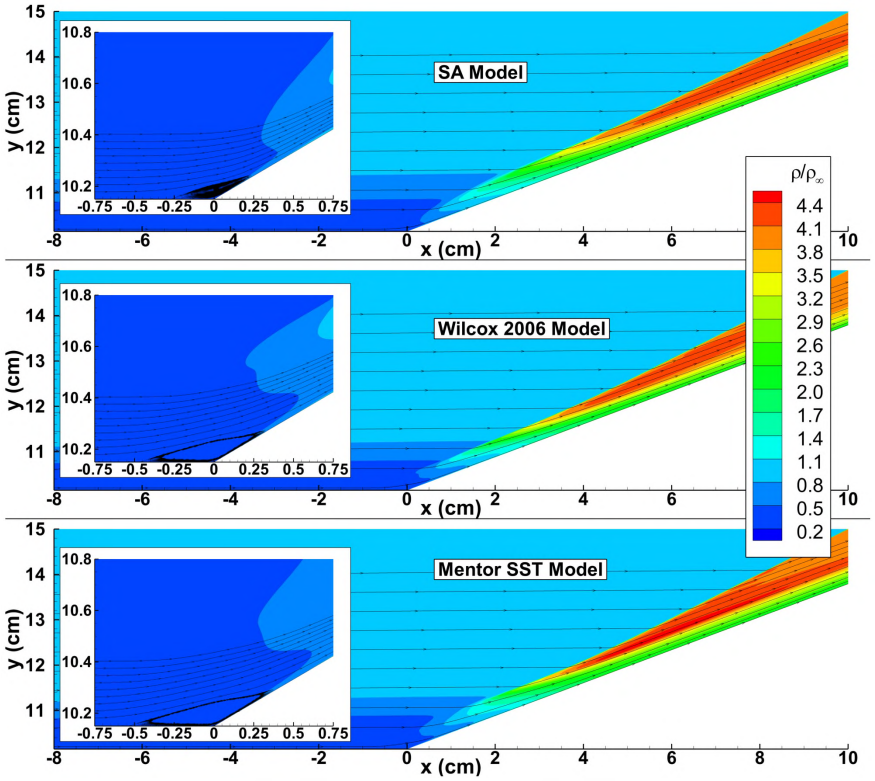

(a) Density contours for the baseline case.

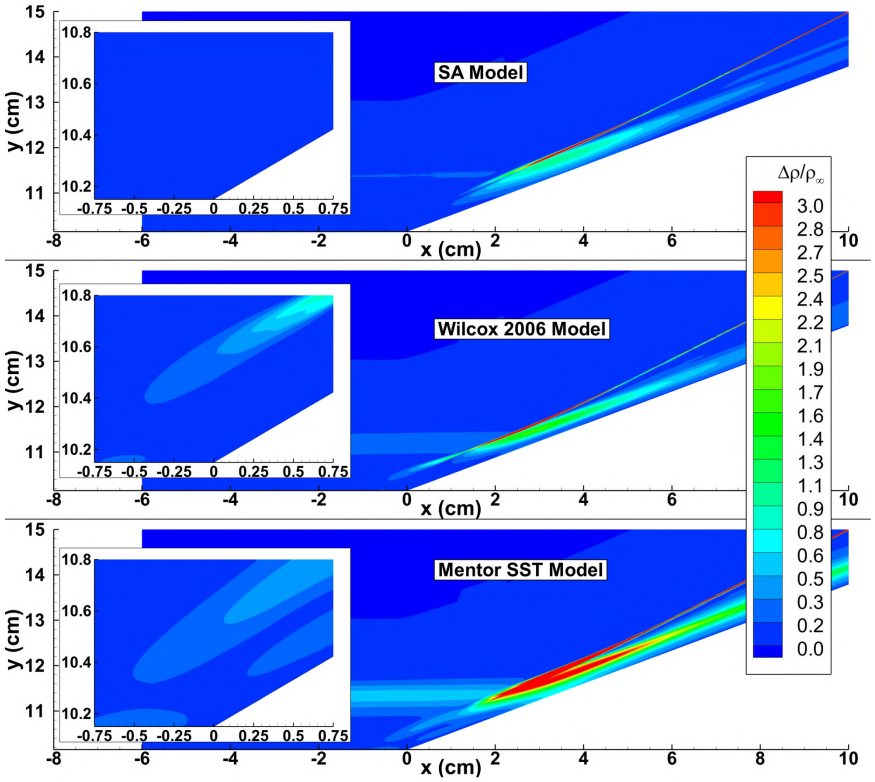

(b) Epistemic interval contours for density.

Figure 5.27. Density ratio uncertainty for the full flow field for ASWBLI.

approximately 25% of the maximum uncertainty. The most uncertainty in ρ/ρ_∞ is the location of the slip line where the model increases the value of the turbulent eddy viscosity and the diffusion of turbulence becomes significant.

In Figures 5.30 and 5.31 the NWSI for C_{lim} and β^* of the W2006 model are presented, respectively. The value of C_{lim} is significant in the Mach number prediction where it contributes nearly equal amounts of uncertainty at the boundary layer edge and separation bubble. The value of β^* provides approximately 40% the amount of uncertainty at the boundary layer edge and 30% in the separation bubble size when compared to C_{lim}. The largest amount of uncertainty in the pressure prediction comes from C_{lim} and is located in the reattachment compression fan region. The location of the separation shock contains approximately 50% of the maximum uncertainty in the pressure prediction. The value of β^* also contributes to the uncertainty at these locations but to a lesser extent. The slip line is the location of the most uncertainty in the density ratio prediction and is dominated by the value of C_{lim} with β^* providing about 25% the amount of uncertainty.

Figures 5.32 and 5.33 presents the NWSI distributions for σ_{w1} and a_1 of the SST model, respectively. The Mach number contours show that value of σ_{w1} significantly impacts the prediction of the boundary layer edge, the separation bubble, and the slip line. Figure 5.32b shows that the pressure prediction is most sensitive to the value of σ_{w1} along the reattachment compression shock. Lastly, the density prediction is most sensitive to the value of σ_{w1} along the slip line after the shock. While the value of κ was shown to be the second largest source of uncertainty in the SST model, a_1 is shown in its place due to the larger contributions it provides in the separation bubble and shock stand off location. The value of a_1 provides 30% of the maximum uncertainty in the separation bubble region (Figure 5.33a) while providing 20% of the maximum uncertainty for the shock stand off location. A study by Georgiadis et al. [51] found that the solution accuracy of shock wave

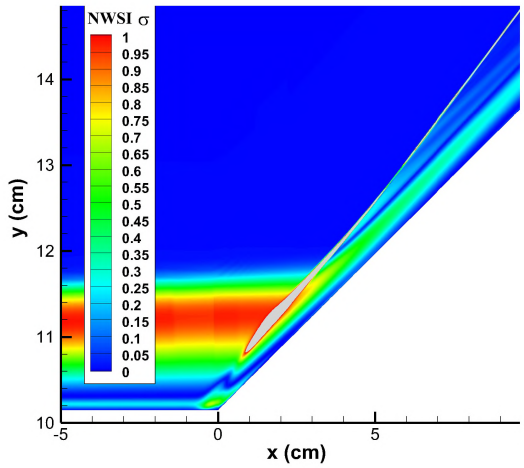

(a) Mach number.

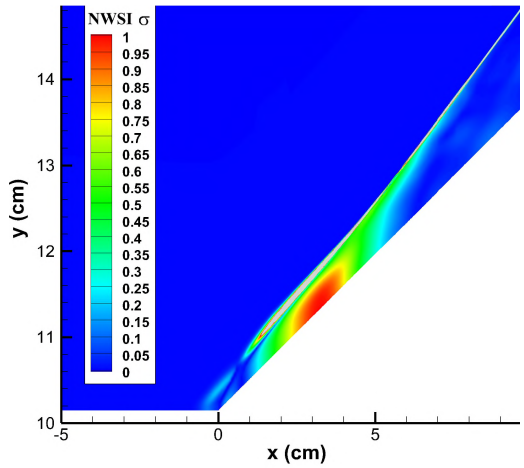

(b) P/P_∞.

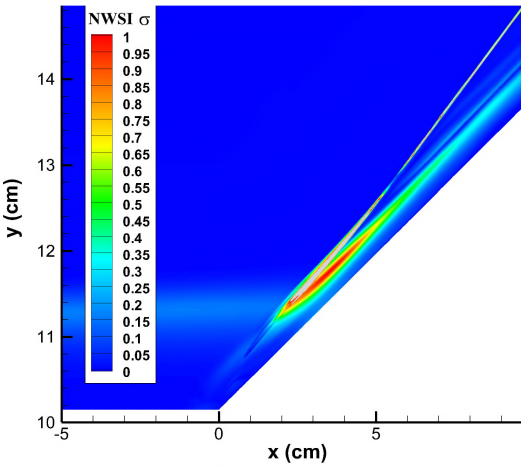

(c) ρ/ρ_∞.

Figure 5.28. NWSI for σ in SA turbulence model for the ASWBLI.

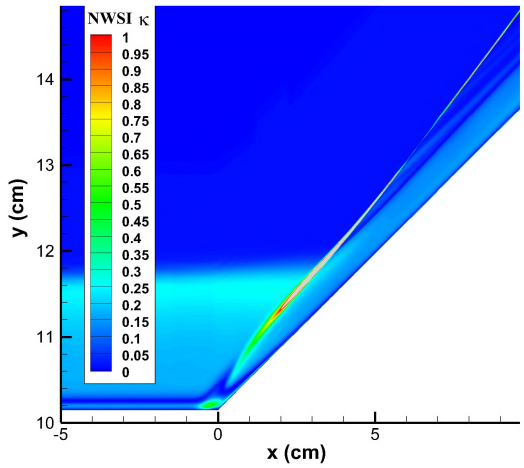

(a) Mach number.

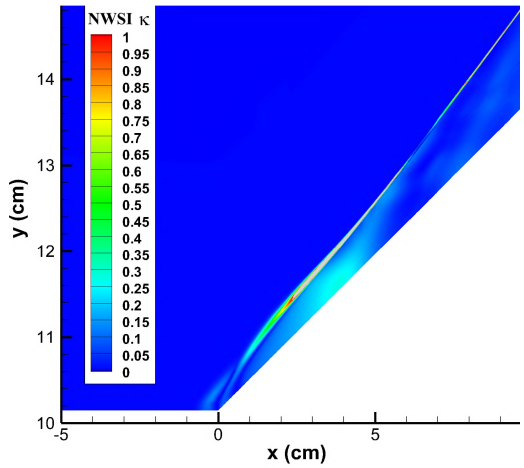

(b) P/P_∞.

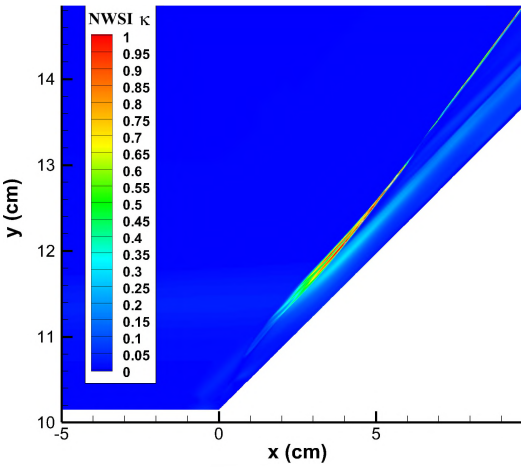

(c) ρ/ρ_∞.

Figure 5.29. NWSI for κ in SA turbulence model for the ASWBLI.

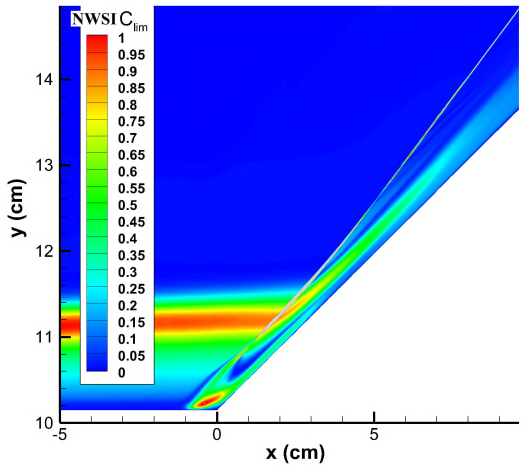

(a) Mach number.

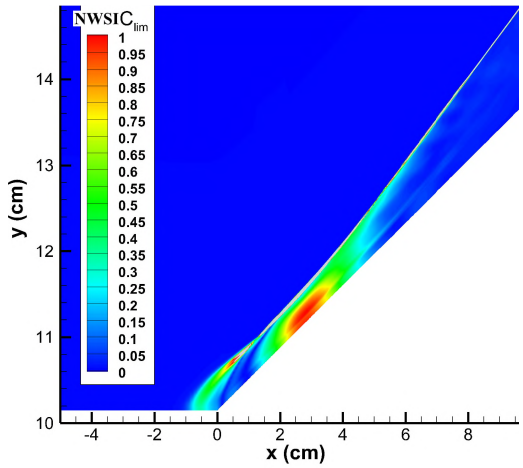

(b) P/P_∞.

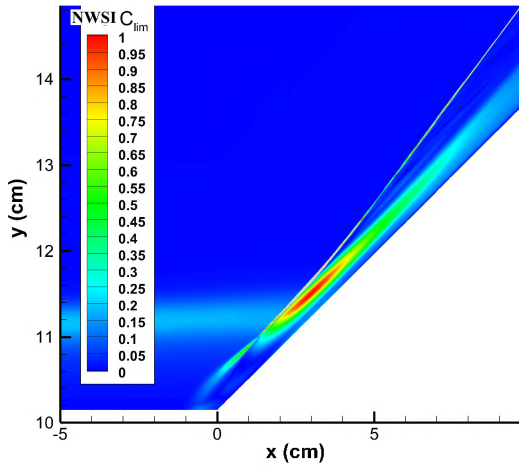

(c) ρ/ρ_∞.

Figure 5.30. NWSI for C_{lim} in W2006 turbulence model for the ASWBLI.

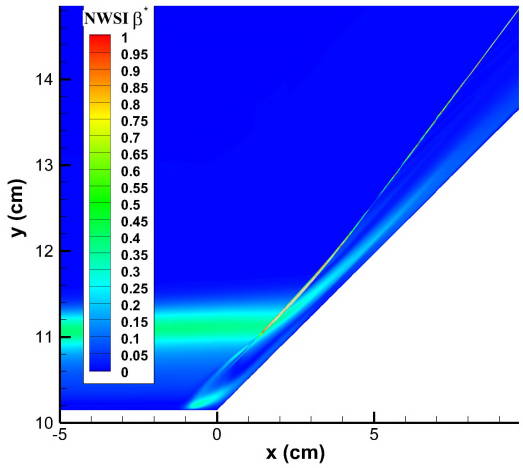

(a) Mach number.

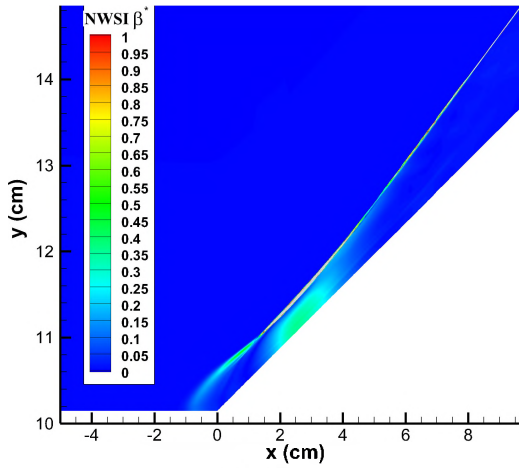

(b) P/P_∞.

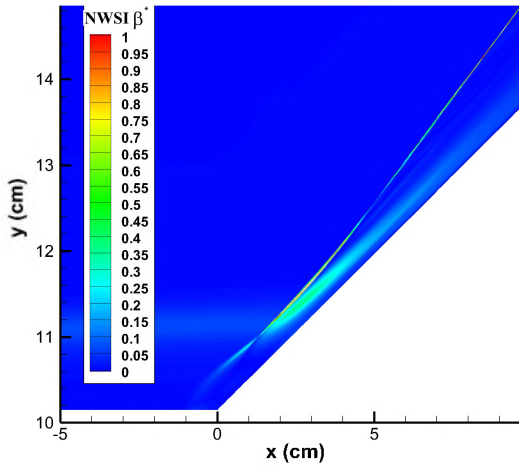

(c) ρ/ρ_∞.

Figure 5.31. NWSI for β^* in W2006 turbulence model for the ASWBLI.

boundary layer interaction flows was improved when an a_1 value that is larger than the nominal one was used. This figure shows that a_1 does play a significant role in determining the origin of the separation shock wave for such a flow regime.

5.1.3.2. Uncertainty analysis for surface quantities. This section investigates the uncertainty in surface properties of interest measured in the experiment conducted by Kussoy and Horstman [34]. These quantities include the wall pressure ratio, $P_w/P_{w,\infty}$ and the wall heat flux ratio, $Q_w/Q_{w,\infty}$. Note that the normalizing quantities, $P_{w,\infty}$ and $Q_{w,\infty}$, are the wall pressure and surface heat flux at $S = -6$ cm. An additional quantity, the skin friction coefficient, C_f, is also investigated despite not having experimental data for it. Other quantities of interest studied include the separation bubble size and the drag coefficient induced by both pressure and skin-friction. The UQ study for this section analyzes a range of flow locations encompassing the flow measurement stations investigated in the previous section. Particularly, stochastic response surfaces of the quantities of interest are obtained over the surface, $S \in \{-6, 20\}$ cm and a UQ and sensitivity study is performed on the turbulence model closure coefficients.

The first quantity of interest investigated is the wall pressure ratio, $P_w/P_{w,\infty}$. The SA results can be seen in Figure 5.34. In Figure 5.34a the SA model tends to slightly overpredict this quantity immediately downstream of the shock in the reattachment compression zone. The model then starts to underpredict this quantity near $S = 7$ cm. When one accounts for the uncertainty in the experimental data, the solution uncertainties capture the experimental data for $S \in \{2, 10\}$ cm. The NWSI plot in Figure 5.34b reveals that the coefficients contributing the most to the uncertainty are σ, κ, and c_{w2} and are most significant as the pressure rises along the reattachment compression region. The W2006 model was investigated next in Figure 5.35. In Figure 5.35a the same overprediction is observed in the wall pressure as seen in the SA model, though the W2006 model overpredicts the pressure by a larger magnitude and does not capture the experimental data despite the experimental uncertainties. Like the SA model, the uncertainty of the closure coefficients produces

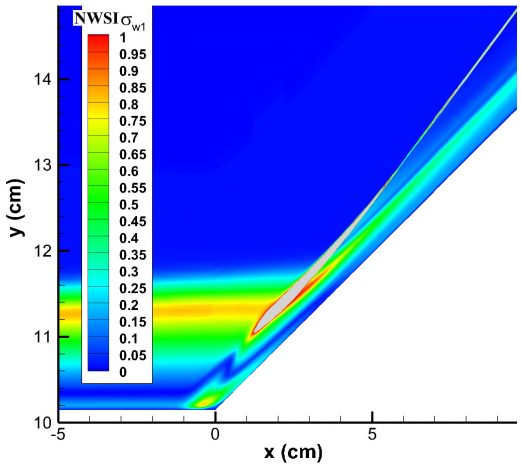

(a) Mach number.

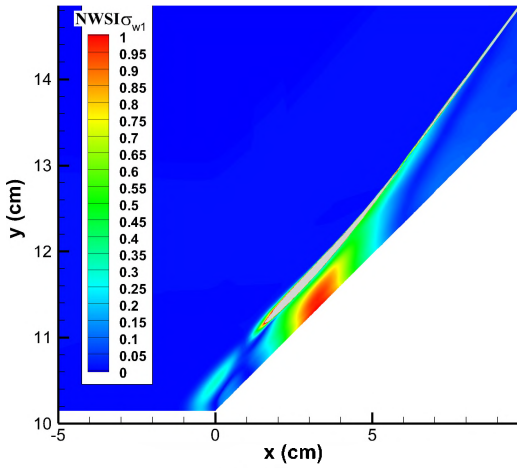

(b) P/P_{∞}.

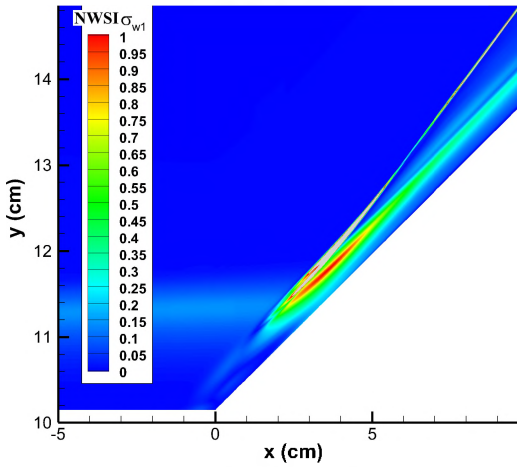

(c) ρ/ρ_{∞}.

Figure 5.32. NWSI for σ_{w1} in SST turbulence model for the ASWBLI.

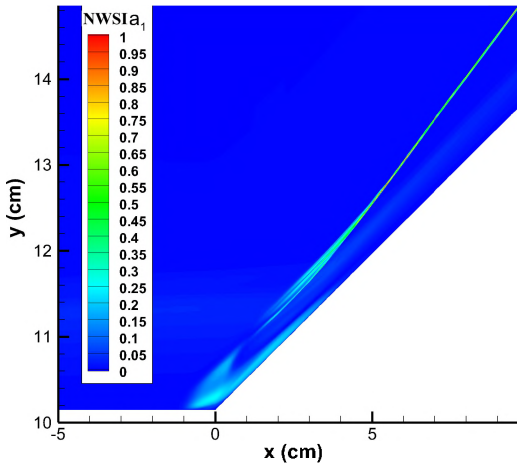

(a) Mach number.

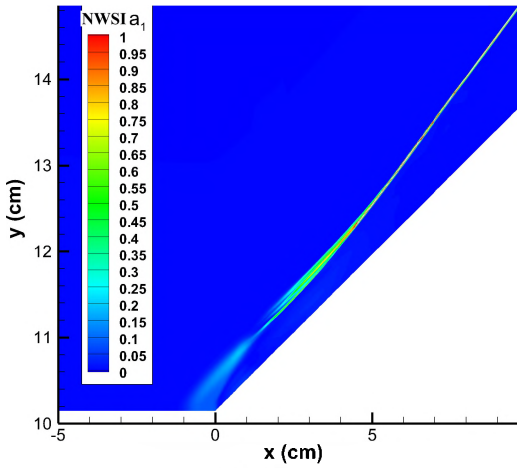

(b) P/P_∞.

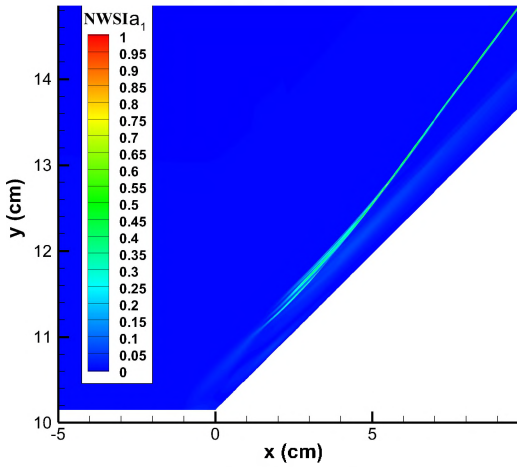

(c) ρ/ρ_∞.

Figure 5.33. NWSI for a_1 in SST turbulence model for the ASWBLI.

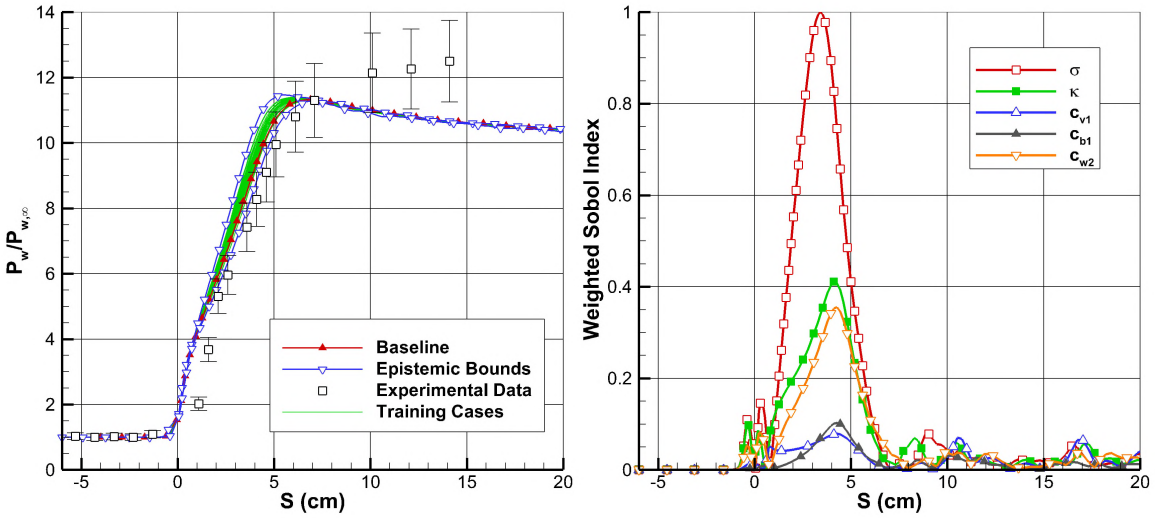

(a) $P_w/P_{w,\infty}$ distribution. (b) NWSI distribution for $P_w/P_{w,\infty}$.

Figure 5.34. Wall pressure uncertainty for ASWBLI (SA model).

results that are, on average, a larger overprediction compared to the baseline case. The NWSI plot in Figure 5.35b shows that the greatest contributors to the uncertainty are C_{lim} and β^* and are most significant along the compression fan after the shock. There is an additional spike of uncertainty inside the separation bubble location. The SST model, seen in Figure 5.36, develops the largest epistemic bound (Figure 5.36a) of the three models but has the greatest propensity to capture the experimental data. The uncertainty in the closure coefficients causes a distribution of wall pressure values with the mean close to the baseline model prediction. The closure coefficients that contribute the most to the uncertainty (Figure 5.36b) in the wall pressure value are σ_{w1} and κ which is largest in the compression fan region. Additionally, there is a spike in uncertainty inside the separation bubble where σ_{w1} is the top contributor but a_1 is also seen to be significant.

The next quantity studied is the wall heat flux ratio, $Q_w/Q_{w,\infty}$. The SA results are shown in Figure 5.37. In Figure 5.37a, the epistemic bounds of the heat flux uncertainty capture many of the experimental data points. It begins to fail near the end of the reattachment compression fan starting from S = 9.0 cm where the model significantly un-

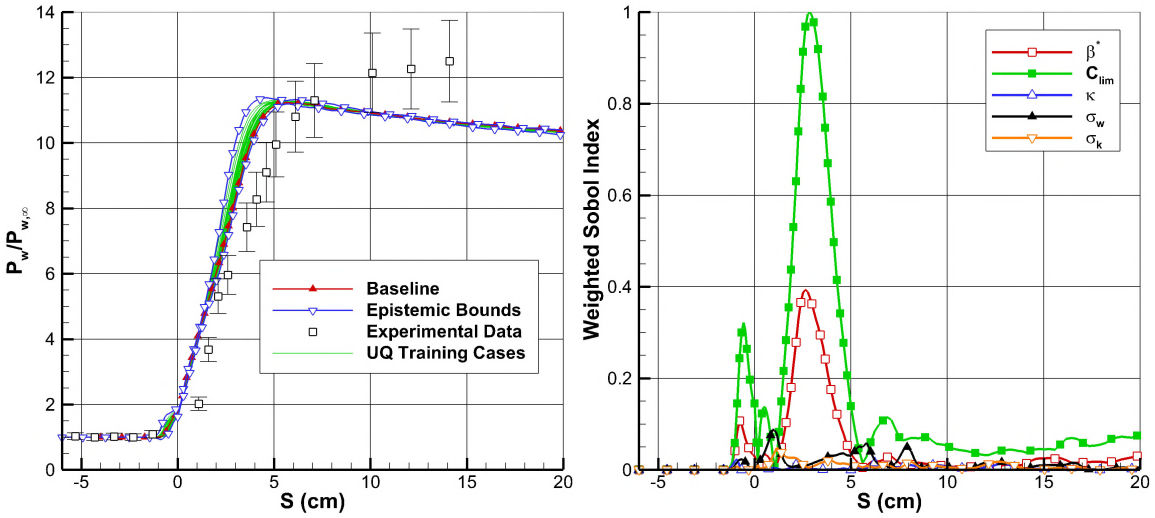

(a) $P_w/P_{w,\infty}$ distribution. (b) NWSI distribution for $P_w/P_{w,\infty}$.

Figure 5.35. Wall pressure uncertainty for ASWBLI (W2006 model).

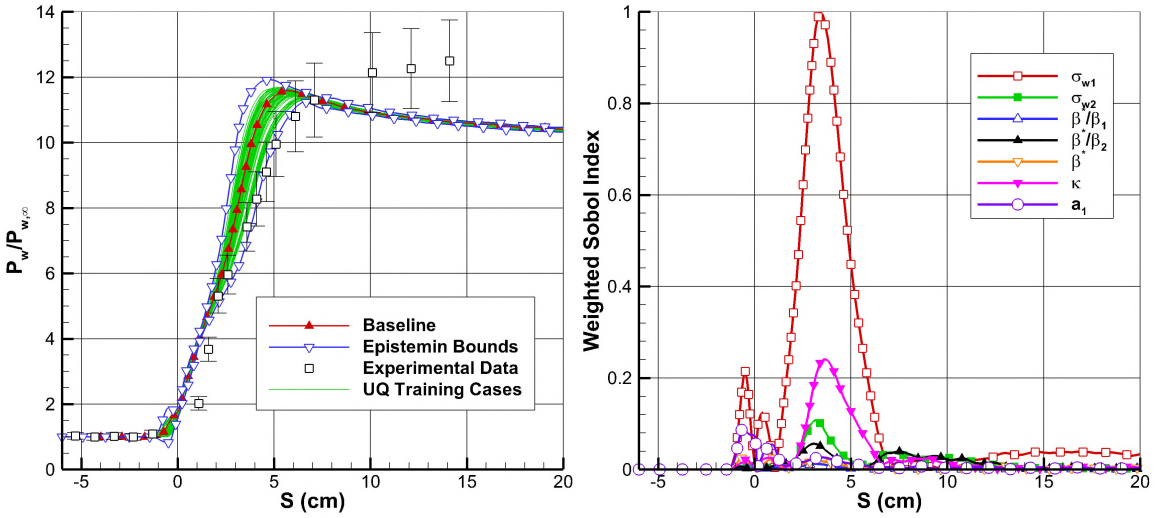

(a) $P_w/P_{w,\infty}$ distribution. (b) NWSI distribution for $P_w/P_{w,\infty}$.

Figure 5.36. Wall pressure uncertainty for ASWBLI (SST model).

derpredicts the wall heat flux. The uncertainty is dominated by σ, c_{w2}, and κ coefficients as evident from the NWSI plot in Figure 5.37b . The results from the W2006 model are seen in Figure 5.38. In Figure 5.38a, the epistemic bounds of the wall heat flux are smaller when compared to the SA model but fails to capture a majority of the experimental data.

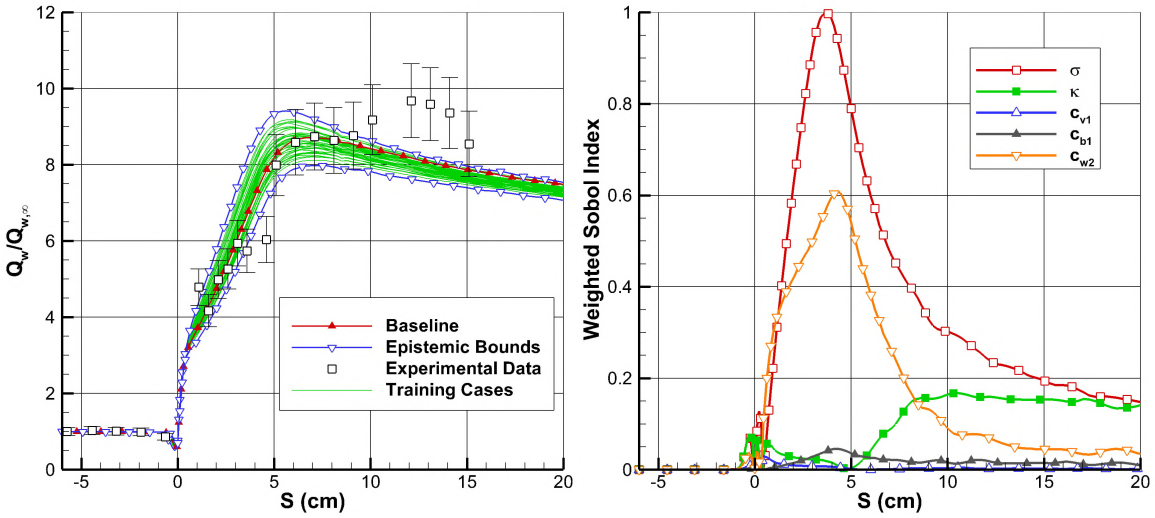

(a) $Q_w/Q_{w,\infty}$ distribution. (b) NWSI distribution for $Q_w/Q_{w,\infty}$.

Figure 5.37. Wall heat flux uncertainty for ASWBLI (SA model).

The figure also shows that the uncertainty in the closure coefficients causes the model to underpredict the wall heat flux at the start of the compression corner when compared to the baseline W2006 solution; after about S = 10 cm the model begins to underpredict the experimental data. Figure 5.38b shows that the coefficients responsible for the majority of the uncertainty are C_{lim}, β^*, σ_k, and σ_w. Lastly, the SST model results are represented in Figure 5.39. Figure 5.39a shows that the uncertainty in the SST model coefficients provide the largest epistemic bound of the wall heat flux measurement, and despite this, it still fails to capture a majority of the experimental data. The model tends to overpredict the wall heat flux at the beginning of the compression corner and displays a quite noticeable overshoot of the measurement near S = 4 cm. The uncertainty in the wall heat flux measurement is dominated by the contributions from σ_{w1} and a_1 as seen in the NWSI plots in Figure 5.39b.

The last surface quantity investigated is the skin friction coefficient, C_f. The results from the SA model are seen in Figure 5.40. Figure 5.40a shows that the solution using the standard closure coefficients is nearly the mean of the solution when accounting for output uncertainty. Also, the magnitude of the epistemic uncertainty grows downstream

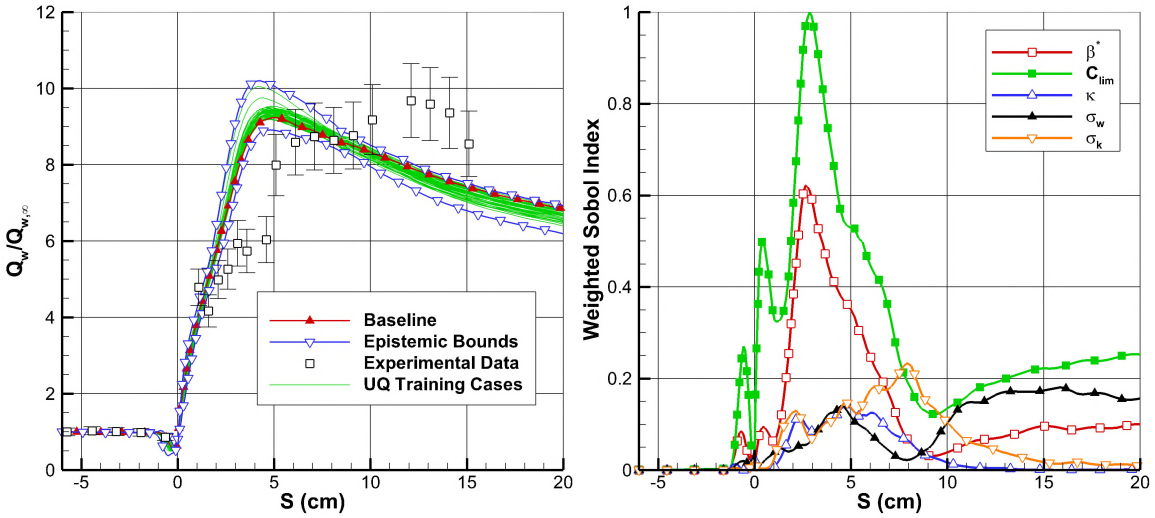

(a) $Q_w/Q_{w,\infty}$ distribution. (b) NWSI distribution for $Q_w/Q_{w,\infty}$.

Figure 5.38. Wall heat flux uncertainty for ASWBLI (W2006 model).

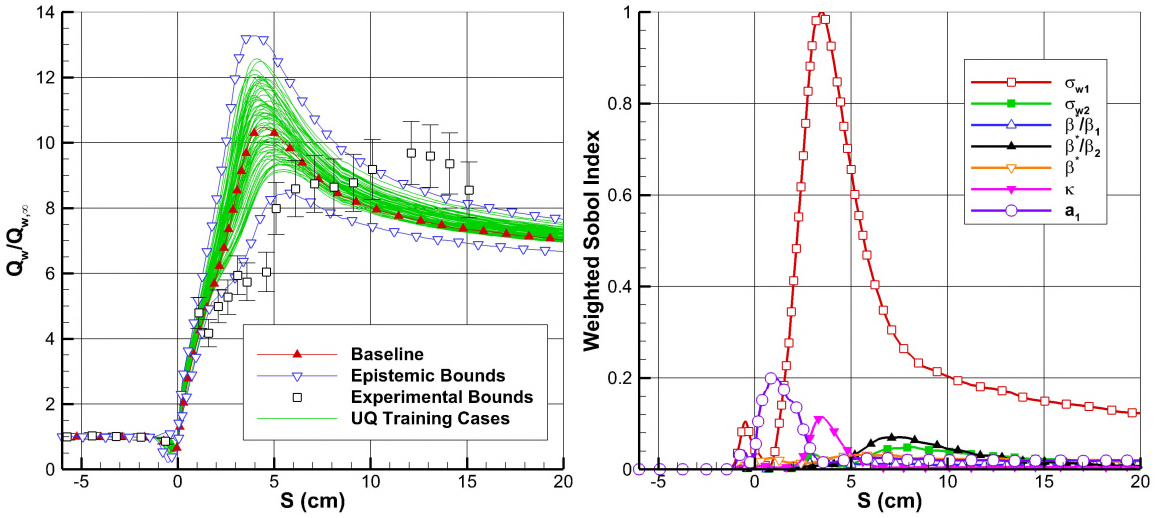

(a) $Q_w/Q_{w,\infty}$ distribution. (b) NWSI distribution for $Q_w/Q_{w,\infty}$.

Figure 5.39. Wall heat flux uncertainty for ASWBLI (SST model).

of the flair vertex. Figure 5.40b shows that the coefficients responsible for this uncertainty are κ, σ, and c_{v1}. The W2006 model is investigated next in Figure 5.41. Figure 5.41a shows that the epistemic bounds resulting from the coefficient uncertainties are tighter when compared to the SA model, and the magnitude of the uncertainty remains consistent

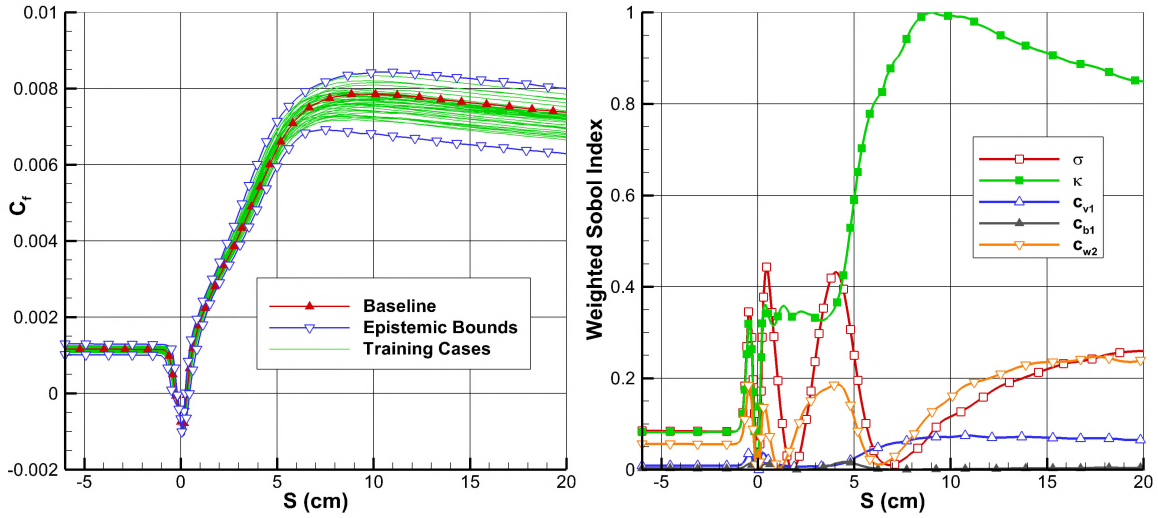

(a) C_f distribution. (b) NWSI distribution for C_f.

Figure 5.40. Skin friction uncertainty for ASWBLI (SA model).

throughout the compression ramp. In Figure 5.41b the significant coefficients involved in the skin friction uncertainties are C_{lim}, σ_{w1}, and β^*. The SST model results are given in Figure 5.42. Figure 5.42a shows that this model exhibits the largest epistemic bound between the three models but is mainly centered around the baseline case. The uncertainty in the model predictions can also be seen in both the separation and reattachment zones where the bounds are seen to widen. Figure 5.42b shows that the coefficients contributing the most to the uncertainty are σ_{w1}, a_1, and κ.

Due to the interaction of the turbulent boundary layer with a strong shock wave, a separated flow region is formed at the apex of the compression corner. As seen in the results of the uncertainty in the closure coefficients, the size of this bubble can vary from case to case and certainly from model to model. Table 5.8 shows that the SST model is the most sensitive to the value of the closure coefficients in the separation bubble size calculation. The W2006 model is slightly less sensitive while the SA model is the least. The pressure induced drag coefficient, C_{D_P}, also possesses uncertainty due to the uncertainty of the closure coefficients. Table 5.8 reveals that the SST model prediction can vary by

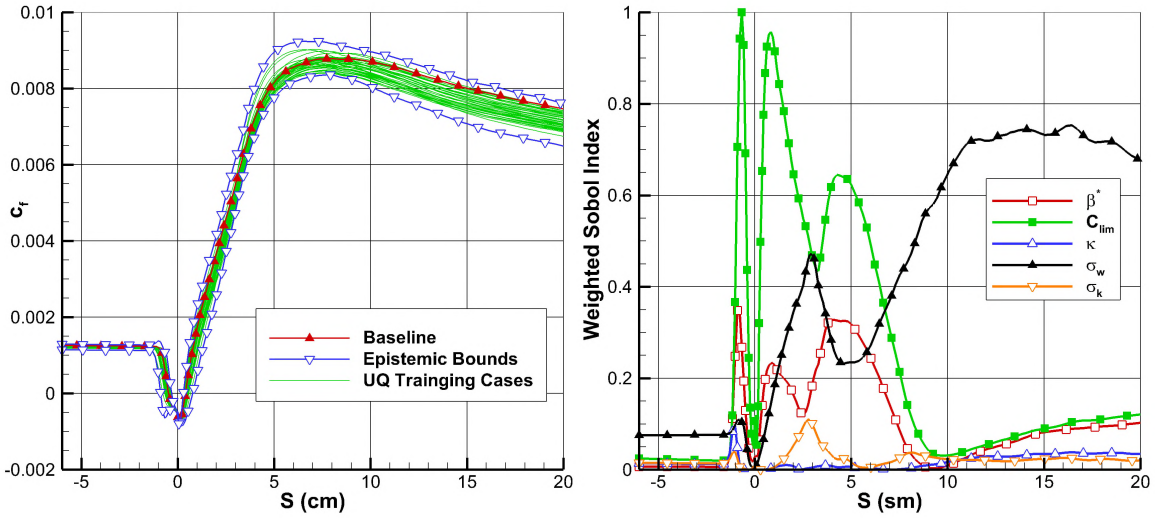

(a) C_f distribution. (b) NWSI distribution for C_f.

Figure 5.41. Skin friction uncertainty for ASWBLI (W2006 model).

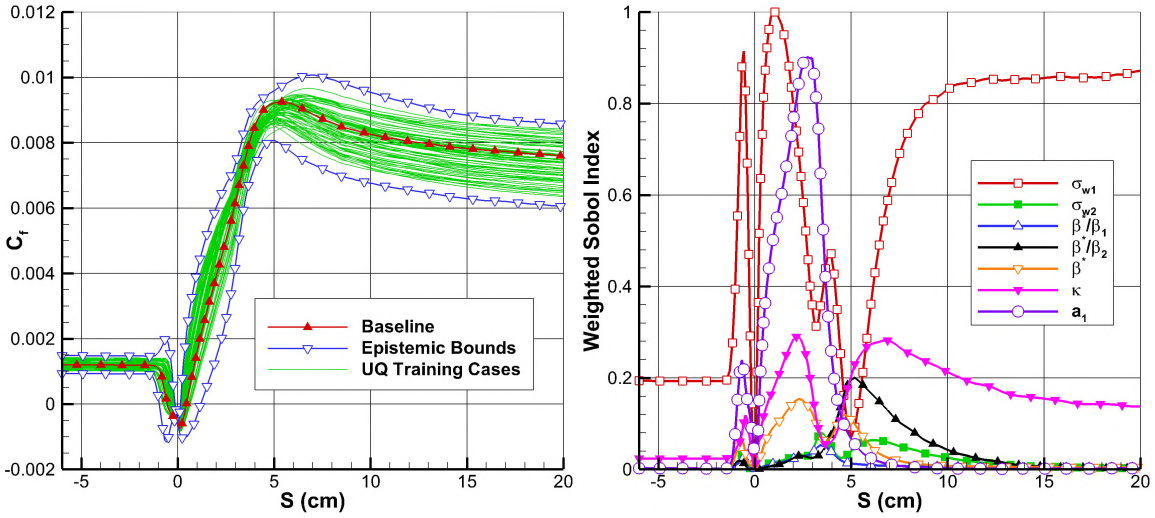

(a) C_f distribution. (b) NWSI distribution for C_f.

Figure 5.42. Skin friction uncertainty for ASWBLI (SST model).

136 drag counts while the W2006 and SA models are slightly less sensitive with only a 78 and 55 drag count variation, respectively. The drag coefficient due to skin friction, $C_{D_{sf}}$, is also influenced by the closure coefficient uncertainty with the SA, W2006, and SST models predicting an 85, 50, and 143 drag count variation, respectively.

Table 5.8. Uncertainty results for the separation bubble size and the drag coefficients for ASWBLI.

Turbulence	Separation Bubble Size			C_{D_p} (Pressure)			$C_{D_{sf}}$ (Skin Friction)		
Model	baseline	min	max	baseline	min	max	baseline	min	max
SA	0.5469	0.4120	0.8572	0.5779	0.5774	0.5828	0.0419	0.0367	0.0452
W2006	0.8179	0.6405	1.6355	0.5856	0.5837	0.5915	0.0450	0.0408	0.0458
SST	0.9379	0.1227	1.9430	0.5815	0.5735	0.5871	0.0454	0.0372	0.0515

Table 5.9. Sobol indices of closure coefficients for SA turbulence model for selected QoIs for the ASWBLI.

Closure Coefficient	$P_w/P_{w,\infty}{}^{\ddagger}$	$Q_w/Q_{w,\infty}{}^{\ddagger}$	$c_f{}^{\ddagger}$	Separation Bubble Size	C_{D_p}	$C_{D_{sf}}$
σ	$^{*}0.46178^{I}$	$^{*}0.55002^{I}$	$^{*}0.16647^{II}$	$^{*}0.42059^{I}$	$^{*}0.84658^{I}$	$^{*}0.10646^{III}$
κ	$^{*}0.22888^{II}$	$^{*}0.11957^{III}$	$^{*}0.65511^{I}$	$^{*}0.36361^{II}$	0.03229^{IV}	$^{*}0.73243^{I}$
c_{v1}	$^{*}0.06311^{IV}$	0.00641^{V}	0.04364^{IV}	0.03937^{IV}	0.01168^{V}	$^{*}0.05243^{IV}$
c_{b1}	$^{*}0.05408^{V}$	0.02499^{IV}	0.00449^{V}	0.01426^{V}	0.04844^{III}	0.00165^{V}
c_{w2}	$^{*}0.19213^{III}$	$^{*}0.29899^{II}$	$^{*}0.13027^{III}$	$^{*}0.16704^{III}$	$^{*}0.06477^{II}$	$^{*}0.11081^{II}$

‡ denotes Normalized Integrated Weighted Sobol Index
∗ denotes significant contribution to uncertainty
I-V denotes ranking of significance

The Sobol index for each closure coefficient in each model for each output quantity of interest are in Tables 5.9 through 5.11. Seen in Table 5.9, σ, κ, and c_{w2} are the major sources of uncertainty for point quantities in the SA model. Table 5.10 shows that C_{lim}, β^*, and σ_{w1} contribute the most to the uncertainty in the W2006 model. The SST model results in Table 5.11 show that σ_{w1}, κ, a_1, and σ_{w2} are among the most significant contributors to uncertainty. Included in these tables are the Normalized Integrated Weighted Sobol Indices of the surface quantities. Similar to the flow field results, a single quantitative metric was desired for ranking the contribution of each uncertain variable within the domain of interest ($S = \theta$ in Eq. 4.12). The ensuing NIWSI of each quantity is the result of integrating the Sobol index plot for $S \in \{-6, 20\}$ cm. This quantitative ranking approach agrees with the qualitative observations made earlier.

Table 5.10. Sobol indices of closure coefficients for W2006 turbulence model for selected QoIs for the ASWBLI.

Closure Coefficient	$P_w/P_{w,\infty}{}^{\ddagger}$	$Q_w/Q_{w,\infty}{}^{\ddagger}$	$c_f{}^{\ddagger}$	Separation Bubble Size	C_{D_p}	$C_{D_{sf}}$
β^*	$*0.21628^{II}$	$*0.22879^{II}$	$*0.13619^{III}$	$*0.21596^{II}$	$*0.20527^{II}$	0.04611^{II}
C_{lim}	$*0.65960^{I}$	$*0.46100^{I}$	$*0.34277^{II}$	$*0.76245^{I}$	$*0.83242^{I}$	0.04385^{III}
κ	0.01866^{V}	$*0.06551^{V}$	0.01723^{V}	0.00514^{IV}	0.01013^{IV}	0.02824^{IV}
σ_w	$*0.06912^{III}$	$*0.11997^{IV}$	$*0.47376^{I}$	$*0.05497^{III}$	0.01099^{III}	$*0.91563^{I}$
σ_k	0.03631^{IV}	$*0.12470^{III}$	0.03002^{IV}	0.00167^{V}	0.00534^{V}	0.01564^{V}

‡ denotes Normalized Integrated Weighted Sobol Index
∗ denotes significant contribution to uncertainty
I-V denotes ranking of significance

Table 5.11. Sobol indices of closure coefficients for Menter SST turbulence model for selected QoIs for the ASWBLI.

Closure Coefficient	$P_w/P_{w,\infty}{}^{\ddagger}$	$Q_w/Q_{w,\infty}{}^{\ddagger}$	$c_f{}^{\ddagger}$	Separation Bubble Size	C_{D_p}	$C_{D_{sf}}$
σ_{w1}	$*0.63356^{I}$	$*0.69152^{I}$	$*0.58168^{I}$	$*0.61817^{I}$	$*0.60871^{I}$	$*0.80136^{I}$
σ_{w2}	$*0.07759^{III}$	$*0.05226^{IV}$	0.02458^{VI}	0.01375^{V}	$*0.13254^{III}$	0.00616^{V}
β^*/β_1	0.01025^{VII}	0.01930^{VII}	0.01041^{VII}	0.00836^{VII}	0.00653^{VII}	0.00397^{VII}
β^*/β_2	$*0.06255^{IV}$	$*0.06244^{III}$	0.04597^{IV}	0.01107^{VI}	$*0.07061^{IV}$	0.00946^{III}
β^*	0.02157^{VI}	0.04687^{V}	0.03728^{V}	$*0.06336^{III}$	0.03017^{VI}	0.00453^{VI}
κ	$*0.14632^{II}$	0.03736^{VI}	$*0.15874^{II}$	$*0.05782^{IV}$	$*0.16502^{II}$	$*0.17330^{II}$
a_1	0.04816^{V}	$*0.09024^{II}$	$*0.14133^{III}$	$*0.28145^{II}$	0.04324^{V}	0.00898^{IV}

‡ denotes Normalized Integrated Weighted Sobol Index
∗ denotes significant contribution to uncertainty
I-VII denotes ranking of significance

5.2. COMPARISON OF RESULTS

In this dissertation, besides the compilation of the summary of results for each case, the comparison of the results between three cases are presented with the objective of generalizing the results and identifying the most significant coefficients that are common for each turbulence model in terms of their contribution to the output uncertainty. In this section, comparison of the results obtained for the three validation cases are presented. The scope of such comparison targets to consolidate several flow types ranging from low to high speed and from attached to separated flow represented with the validation cases investigated

in this work. While the turbulence models implemented in this dissertation are designed primarily for attached low-speed flows, it is also understood that these models are often used for the simulation of compressible flows which may include separated regions. As such, this comparison aims to analyze how the turbulence model uncertainties originating from closure coefficients compare in hypersonic (compressible) and low speed (incompressible) flows which may contain separated flow regions. Section 5.2.1 will present the comparison of results for the three canonical flow cases that were investigated in this study. Section 5.2.2 will provide a model-based explanation as to why many of the closure coefficient provide a significant degree of uncertainty to the selected QoIs. Section 5.2.3 will present a comparison between findings of this study with the results of similar studies within the same scope.

5.2.1. Comparisons of Test Cases. Several similarities are discovered while examining the uncertainty contributions of SA model closure coefficients to specific QoIs. Table 5.12 presents a list of significant closure coefficients in the SA model collected from the three comparison studies. The main contributors to the uncertainty in velocity are κ, σ, and c_{w2}. The ranking of the contributors to the skin friction coefficient uncertainty is shown to be identical between the three cases studied and are, in order, κ, σ, and c_{w2}. Similarly, the coefficients responsible for the most surface pressure uncertainty for the 2DWMH and ASWBLI cases are σ, κ, and c_{w2}. The uncertainty in drag coefficient and the separation bubble size for the 2DWMH and ASWBLI cases mainly come from coefficients κ, σ. The wall heating uncertainty for the ASWBLI is primarily due to σ and c_{w2}.

When a similar comparison is performed for the W2006 model, a set of closure coefficients are identified that contribute to the majority of solution uncertainty and is shown in Table 5.13. The uncertainty in velocity as well as the skin friction for all three flow problems stem from the variation in σ_w, C_{lim}, and β^*. The surface pressure, the drag coefficient, and separation bubble size for the 2DWMH and ASWBLI cases are most sensitive to the uncertainty in σ_w, C_{lim}, and β^*. The wall heating uncertainty for

the ASWBLI case comes primarliy from C_{lim} and β^*. These results show that the top contribution to the output uncertainty for all three flow problems and every QoI considered in the study comes from either C_{lim} or σ_w.

Lastly, the same comparison study with the results from the SST model (Table 5.14) is performed. One fact to note is that this model exhibits more variation in the contributing factors to the output uncertainty. The top contributor to the velocity uncertainty comes from β^* for the 2DZP, from a_1 for the 2DWMH, and from σ_{w1} for the ASWBLI case while κ ranks second for both the 2DWMH and ASWBLI cases. The skin friction coefficient uncertainty is shown to primarily come from β^* for the 2DZP, κ for the 2DWMH, and σ_{w1} for the ASWBLI case. The surface pressure uncertainty comes from a_1 and κ for the 2DWMH and from σ_{w1} and κ for the ASWBLI case. The top contributor to both the drag coefficient and separation bubble size uncertainty for both the 2DWMH and ASWBLI cases stem from one of the diffusion constants, σ_{w2} for the 2DWMH case and σ_{w1} for the ASWBLI case. The wall heating sensitivity for the ASWBLI case comes from the variation in the σ_{w1} value.

5.2.2. Model-Based Interpretation of the Results. When the closure coefficients that are significant to the uncertainty for each model are compared across the cases considered in this study, several similarities can be found. In fact, the results of 2DZP and 2DWMH show strong similarities with what is obtained for the ASWBLI case which is summarized in this dissertation and studied in detail by Erb and Hosder [14]. The majority of the parametric uncertainty (i.e, related to closure coefficient uncertainty) for the considered QoIs when using the SA turbulence model are found to come from the σ, κ, and c_{w2} closure coefficients. When examined, the original formulation of the model exposes the cause for why the diffusion constant, σ, and the turbulent destruction slope control coefficient, c_{w2}, are driving factors for their large contribution. Spalart and Allmaras show calibration curves for c_{b1}, c_{b2}, and c_{w2} as functions of σ in Figure 1 of Ref. [4]. The shallow slopes of c_{b1} and c_{b2} reveal that these coefficients were insensitive to the value of σ during the original calibration process. Contrarily, the figure also shows that c_{w2} and σ had nearly

a one-to-one relationship during the calibration process. Thus, any modification of the two coefficients beyond what the original dependence dictates would exceedingly alter the original constraints of the model. The Von Karman's constant, κ, is a fundamental turbulence parameter that calibrates the slope of the log layer and directly influences the shear stress in a boundary layer. Therefore, it is understood that this parameter will produce uncertainty in the predictive capabilities of a model, especially while predicting skin friction.

The significance of the diffusion constant in the SA model, σ, is also observed for its counterparts in the W2006 model (σ_w) and SST model (σ_{w1} and σ_{w2}). These coefficients influence the predicted boundary layer structure and momentum thickness, and, therefore, sensitivity of the solution is clearly affected by the uncertainty in their exact values. The rates of energy dissipation due to diffusion have an affect on the skin friction prediction which in turn affects the boundary layer velocity profile and shock formation [52]. In fact, for all three cases investigated, the diffusion parameter is shown to contribute a significant amount of parametric uncertainty in the skin friction coefficient prediction for all three turbulence models studied.

The W2006 model stress-limiter term, C_{lim}, is seen to significantly influence the prediction capabilities of the model. The stress-limiter term was specifically included in the updated model to adjust the dependence of eddy viscosity on turbulence properties especially for supersonic and hypersonic flows [41]. This new term proposes a constitutive relation between the Reynolds stresses and mean-flow properties. The solution of all three cases studied, regardless of the speed regime, are shown to be sensitive to the value of the shear stress limiter owing to the fact that it couples QoIs, such as skin friction and pressure, to the magnitude of the Reynolds stresses and turbulent production. For the particular case of hypersonic flows, Wilcox even suggests that different formulations of the stress limiter can have detrimental effects on shock-induced separation and boundary layer structure [41]. Georgiadis and Yoder [51] identified a deficiency in the SST model to accurately predict shock wave turbulent boundary layer flow. They found that the baseline SST model typically

Table 5.12. Summary of significant closure coefficients for the SA model.

	U^+, u/U_∞, Mach Number	Skin Friction	Surface Pressure	Drag Coefficient	Separation Bubble	Wall Heating
2DZP	κ, σ, c_{w2}	κ, σ, c_{w2}	-	-	-	-
2DWMH	σ, c_{w2}, κ, c_{b1}	κ, σ, c_{w2}, c_{b1}, c_{w3}	σ, κ, c_{w2}, c_{b1}	κ, σ, c_{v1}, c_{b1}, c_{v1}	σ, κ, c_{w2}, c_{b1}, c_{w3}	-
ASWBLI	σ, κ, c_{w2}	κ, σ, c_{w2}	σ, κ, c_{w2}, c_{v1}, c_{b1}	σ, κ	σ, κ, c_{w2}, c_{v1}	σ, c_{w2}, κ

Note: Closure coefficients are listed in order of significance for each QoI. The 2DZP case investigates U^+, the 2DWMH case investigates u/U_∞, and the ASWBLI case investigates Mach number.

overestimates the size of the separated flow region and proposed increasing the value of the proportionality constant (a_1), or shear stress limiter, in the SST model. In their study of a Mach 2.25 flow with an 8 degree compression corner, they found that raising the value of a_1 from the standard value of 0.31 to 0.355 results in a better prediction to the the shock-induced separation bubble size. In a study by Tan and Jin [53], modified a_1 values in the SST model were explored using a Wilcox-type stress limiter, C_{lim}, in supersonic and hypersonic flow regimes. The conclusion of their study found that an optimum stress limiter is not likely for all flow regimes and suggest that the value could be a function of the flow variables. Furthermore, Holden et al. [28] found that altering the value of C_{lim} improved agreement between the CFD predicted values and experimental measurements. In a recent paper, Erb and Hosder [50] showed that the prediction of a number of QoIs for shock wave and turbulent boundary layer flow at Mach 2.85 using the Wilcox 2006 model is most sensitive to the value of the stress limiter, C_{lim}. This conclusion is consistent with the findings of the current study. In the majority of QoIs studied in this dissertation, the Wilcox stress limiter ranks as the top contributor to the model predictions showing that the model is most sensitive to the value of C_{lim}. Furthermore, the SST model predictions of the separation bubble size and the surface QoI measurements in areas near the compression corner have a strong sensitivity to the value of a_1.

Table 5.13. Summary of significant closure coefficients for the W2006 model.

	U^+, u/U_∞, Mach Number	Skin Friction	Surface Pressure	Drag Coefficient	Separation Bubble	Wall Heating
2DZP	σ_w, C_{lim}, β^*	σ_w, C_{lim}, β^*	-	-	-	-
2DWMH	C_{lim}, σ_w, β^*	C_{lim}, σ_w, β^*	C_{lim}, β^*, σ_w	σ_w, C_{lim}, β^*	C_{lim}, β^*, σ_w	-
ASWBLI	C_{lim}, β^*, σ_w	σ_w, C_{lim}, β^*	C_{lim}, β^*, σ_w	C_{lim}, β^*, σ_w	C_{lim}, σ_w, β^*	C_{lim}, β^*, σ_k, σ_w, κ

Note: Closure coefficients are listed in order of significance for each QoI. The 2DZP case investigates U^+, the 2DWMH case investigates u/U_∞, and the ASWBLI case investigates Mach number.

Table 5.14. Summary of significant closure coefficients for the SST model.

	U^+, u/U_∞, Mach Number	Skin Friction	Surface Pressure	Drag Coefficient	Separation Bubble	Wall Heating
2DZP	β^*, σ_{w1}, β^*/β_1	β^*, σ_{w1}, β^*/β_1	-	-	-	-
2DWMH	a_1, κ, σ_{w2} σ_{w1}, β^*/β_2	κ, σ_{w2}, a_1 β^*/β_2, σ_{w1}	a_1, κ, σ_{w2} β^*/β_2, σ_{w1}	σ_{w2}, κ β^*/β_1, σ_{w1}	σ_{w2}, a_1, κ β^*/β_1, σ_{w1}	-
ASWBLI	σ_{w1}, κ, σ_{w2}	σ_{w1}, κ, a_1	σ_{w1}, κ σ_{w2}, β^*/β_2	σ_{w1}, κ σ_{w2}, β^*/β_2	σ_{w1}, a_1 β^*, κ	σ_{w1}, a_1 β^*/β_2, σ_{w2}

Note: Closure coefficients are listed in order of significance for each QoI. The 2DZP case investigates U^+, the 2DWMH case investigates u/U_∞, and the ASWBLI case investigates Mach number.

5.2.3. Comparison to Previous Relevant Work. There have been a number of previous studies conducted within the scope of this research (i.e., uncertainty and sensitivity analyses of turbulence model closure coefficients) and this section will discuss the similarities between the results of the current study and previous relevant work. The previous studies of interest include an Axisymmetric Transonic Bump (ATB) which is a validations case on the TMR, an Axisymmetric Shock Wave Boundary Layer Interaction at $M = 2.85$ which is similar to the ASWBLI case presented here but was chosen to be a part of the NASA's 40% Challenge and CFD Prediction Error Assessment Workshop 2018 (40PC), an RAE 2822 transonic airfoil (RAE2822), and a scramjet isolator (SJI).

When the results of wall pressure are analyzed, several comparisons can be made. The current ranking of the significant closure coefficients for the 2DWMH and the ASWBLI cases match with the findings of the 40PC, ATB, and RAE2822 cases. When the SA turbulence model is considered, the uncertainties in σ, κ, and c_{w2} are shown to provide the largest source of wall pressure uncertainty for all five cases. Likewise, the largest source of wall pressure uncertainty using the W2006 turbulence model is consistently C_{lim} for all five cases examined. Finally, the results from the SST model show that σ_{w1} is among the top contributors to wall pressure uncertainty (for all but the 40PC because the SST model was not used in this study).

The skin friction prediction sensitivity can also be compared between the cases. The 2DZP, 2DWMH, ASWBLI, 40PC, ATB, and SJI all show remarkable similarity with respect to the largest source of uncertainty for this QoI. For all six cases analyzed, the largest source of skin friction uncertainty for the SA turbulence model is consistently κ, σ, and c_{w2}. The W2006 uncertainty in skin friction prediction for all six cases include σ_w and C_{lim}. The sources of skin friction uncertainty in the SST model shows more variation compared to the SA and W2006 models, however, in the five cases where the SST is employed (40PC is excluded), the closure coefficient, σ_{w1}, provides the largest parametric uncertainty.

The same sort of comparison can be made with respect to the total drag coefficient uncertainty (including both pressure and viscous components). For this comparison the 2DWMH, ASWBLI, ATB, and the RAE2822 show significant similarity. The SA turbulence model prediction uncertainty for the drag coefficient results come primarily from κ and σ for all four cases. The uncertainty in drag coefficient prediction when the W2006 turbulence model is employed comes from uncertainties in σ_w, C_{lim}, and β^*. Like in the skin friction prediction comparison, the SST model shows the most variation in the largest source of uncertainty. The 2DWMH and ASWBLI both shows that σ_{w1}, κ, and σ_{w2} are among the largest sources of drag coefficient uncertainty while the ATB and RAE2822 places β^*, β^*/β_1, and β^*/β_2 among the top sources.

The size of a separation bubble can also be compared between several cases. The 2DWMH, ASWBLI, and ATB each contain a separation bubble in their simulated flow fields. The largest sources of separation bubble size uncertainty predicted with the SA turbulence model are σ, κ, and c_{w2} for all three cases. Likewise, the uncertainty for all three cases in the separation bubble size prediction using the W2006 model come from σ_w, β^*, and C_{lim}. The SST model again shows the largest variation when the most significant sources of uncertainty for this quantity are identified, but all three cases incorporate σ_{w1} and a_1 among this grouping.

Finally, when the largest source of uncertainty in velocity and Mach number is compared, similarities can also be observed. For this comparison, the 2DZP uses u^+, the 2DWMH uses u/U_∞, the ASWBLI uses Mach number, and the 40PC uses u. The common uncertainty sources for this QoI for the SA model are σ, κ, and c_{w2} for all four cases. The sources for the W2006 turbulence model include σ_w, β^*, and C_{lim}. Lastly, for the SST turbulence model, the three cases studied (40PC excluded) all share σ_{w1} as the common contributor to the uncertainty.

6. CONCLUSIONS AND FUTURE WORK

The previous section provided a detailed examination of the results obtained from the study conducted for this dissertation. This section highlights the important results and commonalities between the three case contained in this dissertation and provides suggestions for future work of this scope. Section 6.1 presents the conclusions drawn from this work. Recommendations for future are presented in Section 6.2.

6.1. CONCLUSIONS

The purpose of the studies presented in this dissertation was to show and compare the results of an uncertainty analysis study for commonly used turbulence models in Reynolds-Averaged Navier-Stokes codes due to the epistemic uncertainty in closure coefficients for a set of canonical flow problems. Sensitivity analysis was performed to rank the uncertainty contribution of each coefficient to various output quantities of interest. In this work, the effect of the epistemic uncertainties in closure coefficients on the prediction capability of the models for aerodynamic flows from low speed attached to shock wave-boundary layer interactions, which pose significant challenges in CFD and turbulence modeling research is studied. The turbulence models implemented in this study include the Spalart-Allmaras One Equation Model, the Wilcox (2006) κ-ω Two-Equation Model, and the Menter Shear-Stress Transport Two-Equation Model.

Three canonical flow problems were studied with these turbulence models: 2D Zero Pressure Gradient Flat Plate, a 2D NASA Wall Mounted Hump, and an Axisymmetric Shock Wave Boundary Layer Interaction, and all are well documented turbulence model validation cases taken the form the NASA TMR. The contributions to uncertainty from each of the closure coefficients for each model were investigated and were also compared between the three flow problems to create a set of generalized findings.

The results of the current study identify a set of closure coefficients for the SA, the W2006, and the Menter SST models that contribute most to the uncertainty in various output quantities of interest. The SA turbulence model is found to be most sensitive to the uncertainties in the diffusion constant (σ), the log layer calibration constant (κ), and the turbulent destruction constant (c_{w2}). The predictive capability of the W2006 model is most sensitive to the uncertainties in a dissipation rate constant (σ_w), the shear stress limiter (C_{lim}), and a turbulence-kinetic energy constant (β^*). Likewise, the SST turbulence model was found to be most sensitive to the diffusion constants (σ_{w1} and σ_{w2}), the log layer calibration constant (κ), and the shear stress limiter (a_1). Improved knowledge of the values of these particular closure coefficients are expected to have the largest impact on reducing the parametric uncertainty in various output quantities of interest obtained with RANS simulations for different flow problems. Therefore, the results of this study are expected to guide the efforts on improving the accuracy of RANS predictions through validation experiments and data-driven modeling approaches for various flow problems by identifying the coefficients for refinement.

6.2. FUTURE WORK

The results contained within this dissertation are expected to provide insight for the turbulence modeling research community into how the solutions uncertainties are affected by the uncertainties in the SA, W2006, and SST turbulence model closure coefficients. Experimental data collection efforts can be focused improving these turbulence models in RANS simulations. Additionally, the NWSI method presented in this study provides a mode of identifying the sources and regions with the highest degree of solution uncertainty. The results can provide experimentalist with a guide for their data collection efforts. Experimental time and equipment are expensive, so having a system in place to quantify the regions with the most solution uncertainty will allow experimentalist to efficiently allocate the available resources.

Future uncertainty quantification and sensitivity analysis studies should also be conducted. Several cases on the NASA TMR have potential to further this type of study and provide knowledge to experimentalists, researchers, and design engineers regarding the level and location of solution uncertainties. The 2D Zero Pressure Gradient High Mach Number Flat Plate Validation Case (2DZPH) is a study on high Mach number flows and turbulent heat flux, which are two important consideration for a hypersonic vehicle designer, but also includes the van Driest transformations, which are theoretical correlations for the compressible skin friction coefficient and wall variables (law of the wall estimations). The free shear flow of the Axisymmetric Hot Supersonic Jet (AHSSJ) would be an important study to understand how the turbulence model closure coefficient uncertainty effects high speed jets and turbulent heat flux. Though not on the TMR, a study on turbulence model uncertainty for chemically reacting compressible flows and combustion problems will be a valuable study for engine designers and could result in more robust designs where combustion kinetic predictions are less sensitive to turbulence model closure coefficient uncertainties.

REFERENCES

[1] 'NASA Langley Research Center turbulence modeling resource website,' http://turbmodels.larc.nasa.gov.

[2] Bose, D., Brown, J. L., Prabhu, D. K., Gnoffo, P., Johnston, C. O., and Hollis, B., 'Uncertainty assessment of hypersonic aerothermodynamics prediction capability,' Journal of Spacecraft and Rockets, 2013, **50**(1), pp. 12–18, doi:10.2514/1.A32268.

[3] Gnoffo, P. A., Berry, S. A., and Van Norman, J. W., 'Uncertainty assessments of hypersonic shock wave-turbulent boundary-layer interactions at compression corners,' Journal of Spacecraft and Rockets, 2013, **50**(1), pp. 69–95, doi:10.2514/1.A32250.

[4] Spalart, P. R. and Allmaras, S. R., 'A one-equation turbulence model for aerodynamic flows,' Recherche Aerospatiale, 1994, (1), pp. 5–21, doi:10.2514/6.1992-439.

[5] Wilcox, D. C., *Turbulence Modeling for CFD*, DCW Industries, Inc., La Cañada CA, 3 edition, 2006.

[6] Menter, F. R., 'Two-equation eddy-viscosity turbulence models for engineering applications,' AIAA Journal, 1994, **32**(8), pp. 1598–1605, doi:10.2514/3.12149.

[7] Slotnick, J., Khodadoust, A., Alonso, J., Darmofal, D., Gropp, W., Lurie, E., and Mavriplis, D., 'CFD vision 2030 study: A path to revolutionary computational aerosciences,' Technical report, NASA/CR-20140218178, March 2014.

[8] Hosder, S., Grossman, B., Haftka, R. T., Mason, W. H., and Watson, L. T., 'Quantitative relative comparison of CFD simulation uncertainties for a transonic diffuser problem,' Computers and Fluids, December 2006, **35**(10), pp. 1444–1458, doi: 10.1016/j.compfluid.2005.04.006.

[9] Hosder, S., Walters, R. W., and Balch, M., 'Point-collocation nonintrusive polynomial chaos method for stochastic computational fluid dynamics,' AIAA Journal, 2010, **48**(12), pp. 2721–2730, doi:10.2514/1.39389.

[10] Hosder, S., Walters, R., and Perez, R., 'A non-intrusive polynomial chaos method for uncertainty propagation in CFD simulations,' in '44th AIAA Aerospace Sciences Meeting and Exhibit,' Reno, NV, 2006 doi:10.2514/6.2006-891.

[11] Schaefer, J., Cary, A., Mani, M., Krakos, J., and Hosder, S., 'Grid influence on turbulence model coefficient uncertainties in transonic wall-bounded flows,' AIAA Journal, 2018, **56**(8), pp. 3123–3137, doi:10.2514/1.J056225.

[12] Schaefer, J., Hosder, S., West, T., Rumsey, C., Carlson, J.-R., and Kleb, W., 'Uncertainty quantification of turbulence model closure coefficients for transonic wall-bounded flows,' AIAA Journal, 2017, **55**(1), pp. 195–213, doi:10.2514/1.J054902.

[13] Di Stefano, M. A., Hosder, S., and Baurle, R. A., 'Effect of turbulence model uncertainty on scramjet isolator flowfield analysis,' Journal of Propulsion and Power, 2020, **36**(1), pp. 109–122, doi:10.2514/1.B37597.

[14] Erb, A. and Hosder, S., 'Analysis of turbulence model uncertainty for shock-wave/boundary-layer interaction simulations,' Journal of Spacecraft and Rockets, Accepted for publication 6 May 2020, doi:10.2514/1.A34770.

[15] West, T. K. and Hosder, S., 'Uncertainty quantification of hypersonic reentry flows with sparse sampling and stochastic expansions,' Journal of Spacecraft and Rockets, 2015, **52**(1), pp. 120–133, doi:10.2514/1.A32947.

[16] West, T. K., Johnston, C. O., and Hosder, S., 'Uncertainty and sensitivity analysis of afterbody radiative heating predictions for earth entry,' Journal of Thermophysics and Heat Transfer, 2017, **31**(2), pp. 294–306, doi:10.2514/1.T4948.

[17] Brune, A. J., Hosder, S., Edquist, K. T., and Tobin, S. A., 'Thermal protection system response uncertainty of a hypersonic inflatable aerodynamic decelerator,' Journal of Spacecraft and Rockets, 2017, **54**(1), pp. 141–154, doi:10.2514/1.A33732.

[18] Brune, A. J., West, T. K., and Hosder, S., 'Uncertainty quantification of planetary entry technologies,' Progress in Aerospace Sciences, 2019, **111**, p. 100574, ISSN 0376-0421, doi:https://doi.org/10.1016/j.paerosci.2019.100574.

[19] Godfrey, A. G. and Cliff, E. M., 'Sensitivity equations for turbulent flows,' in '39th Aerospace Sciences Meeting and Exhibit, Aerospace Sciences Meetings,' American Institute of Aeronautics and Astronautics, Reno, Nevada, January 2001 doi: 10.2514/6.2001-1060.

[20] Han, D. and Hosder, S., 'Inherent and epistemic uncertainty analysis for computational fluid dynamics simulations of synthetic jet actuators,' International Journal for Uncertainty Quantification, 2014, **4**, pp. 511–533, doi: 10.1615/Int.J.UncertaintyQuantification.2014010659.

[21] Turgeon, E., Pelletier, D., and Borggaard, J., 'Application of a sensitivity equation method to the k-epsilon model of turbulence,' in '15th AIAA Computational Fluid Dynamics Conference,' American Institute of Aeronautics and Astronautics, June 2001 doi:10.2514/6.2001-2534.

[22] Turgeon, E., Pelletier, D., and Borggaard, J., 'A general continuous sensitivity equation formulation for the k-epsilon model of turbulence,' in '15th AIAA Computational Fluid Dynamics Conference,' American Institute of Aeronautics and Astronautics, June 2001 doi:10.2514/6.2001-3000.

[23] Platteeuw, P., Loeven, G., and Bijl, H., 'Uncertainty quantification applied to the k-epsilon model of turbulence using the probabilistic collocation method,' April 2008, doi:10.2514/6.2008-2150.

[24] Dunn, M. C., Shotorban, B., and Frendi, A., 'Uncertainty quantification of turbulence model coefficients via latin hypercube sampling method,' Journal of Fluids Engineering, 2011, **133**(4), ISSN 0098-2202, doi:10.1115/1.4003762.

[25] Pope, S. B., 'Turbulent flows,' Measurement Science and Technology, 2001, **12**(11), pp. 2020–2021, doi:10.1088/0957-0233/12/11/705.

[26] Margheri, L., Meldi, M., Salvetti, M., and Sagaut, P., 'Epistemic uncertainties in rans model free coefficients,' Computers and Fluids, 2014, **102**, pp. 315 – 335, ISSN 0045-7930, doi:https://doi.org/10.1016/j.compfluid.2014.06.029.

[27] Xiao, H. and Cinnella, P., 'Quantification of model uncertainty in rans simulations: A review,' Progress in Aerospace Sciences, 2019, **108**, pp. 1 – 31, ISSN 0376-0421, doi:https://doi.org/10.1016/j.paerosci.2018.10.001.

[28] Holden, M., Wadhams, T., MacLean, M., and Mundy, E., 'Experimental studies of shock wave/turbulent boundary layer interaction in high reynolds number supersonic and hypersonic flows to evaluate the performance of CFD codes,' in '40th Fluid Dynamics Conference and Exhibit,' American Institute of Aeronautics and Astronautics, June 2010 doi:10.2514/6.2010-4468.

[29] DeBonis, J. R., Oberkampf, W. L., Wolf, R. T., Orkwis, P. D., Turner, M. G., Babinsky, H., and Benek, J. A., 'Assessment of computational fluid dynamics and experimental data for shock boundary-layer interactions,' AIAA Journal, 2012, **50**(4), pp. 891–903, doi:10.2514/1.J051341.

[30] Georgiadis, N., Rumsey, C., and Huang, G., 'Revisiting turbulence model validation for high-mach number axisymmetric compression corner flows,' in '53rd AIAA Aerospace Sciences Meeting, AIAA SciTech Forum,' American Institute of Aeronautics and Astronautics, Kissimmee, Florida, 2015 doi:10.2514/6.2015-0316.

[31] Greenblatt, D., Paschal, K. B., Yao, C.-S., Harris, J., Schaeffler, N. W., and Washburn, A. E., 'Experimental investigation of separation control part 1: Baseline and steady suction,' AIAA Journal, 2006, **44**(12), pp. 2820–2830, doi:10.2514/1.13817.

[32] Greenblatt, D., Paschal, K. B., Yao, C.-S., and Harris, J., 'Experimental investigation of separation control part 2: Zero mass-flux oscillatory blowing,' AIAA Journal, 2006, **44**(12), pp. 2831–2845, doi:10.2514/1.19324.

[33] Naughton, J. W., Viken, S. A., and Greenblatt, D., 'Skin-friction measurements on the nasa hump model,' AIAA Journal, 2006, **44**(6), pp. 1255–1265, doi:10.2514/1.14192.

[34] Kussoy, M. I. and Horstman, C. C., 'Documentation of two- and three-dimensional hypersonic shock wave boundary layer interaction flows,' Technical report, NASA TM 101075, January 1989.

[35] Biedron, R., Carlson, J., Derlaga, J., Gnoffo, P., Hammond, D., Jones, W., Kleb, B., Lee-Rausch, E., Nielsen, E., Park, M., Rumsey, C., Thomas, J., and Wood, W., 'Fun3d manual: 13.1,' Technical report, NASA/TM-2017-219580, February 2017.

[36] Toro, E. F., Spruce, M., and Speares, W., 'Restoration of the contact surface in the hll-riemann solver,' Shock Waves, 1994, **4**(1), p. 25–34, doi:10.1007/BF01414629.

[37] BALDWIN, B. and BARTH, T., 'A one-equation turbulence transport model for high reynolds number wall-bounded flows,' in '29th Aerospace Sciences Meeting,' American Institute of Aeronautics and Astronautics, January 1991 doi:10.2514/6.1991-610.

[38] Nee, V. W. and Kovasznay, L. S. G., 'Simple phenomenological theory of turbulent shear flows,' The Physics of Fluids, 1969, **12**(3), pp. 473–484, doi:10.1063/1.1692510.

[39] Schaefer, J., West, T., Hosder, S., Rumsey, C., Carlson, J., and Kleb, W., 'Uncertainty quantification of turbulence model closure coefficients for transonic wall-bounded flows,' in '22nd AIAA Computational Fluid Dynamics conference,' American Institute of Aeronautics and Astronautics, Dallas, TX, June 2015 doi:10.2514/6.2015-2461.

[40] Rumsey, C. and Spalart, P., 'Turbulence model behavior in low reynolds number regions of aerodynamic flowfields,' AIAA Journal, April 2009, doi:10.2514/1.39947.

[41] Wilcox, D. C., 'Formulation of the k-omega turbulence model revisited,' AIAA Journal, 2008, **46**(11), pp. 2823–2828, doi:10.2514/1.36541.

[42] Ghanem, R. G. and Spanos, P. D., *Stochastic Finite Elements: A Spectral Approach*, chapter 7, 14, Springer-Verlag, New York, 1991, doi:10.1007/978-1-4612-3094-6.

[43] Eldred, M. S., 'Recent advances in non-intrusive polynomial chaos and stochastic collocation methods for uncertainty analysis and design,' in '50th AIAA/ASME/ASCE/AHS/ASC Structures, Structural Dynamics, and Materials conference, Structures, Structural Dynamics, and Materials and Co-located conferences,' American Institute of Aeronautics and Astronautics, Palm Springs, California, May 2009 doi:10.2514/6.2009-2274.

[44] Hosder, S., Walters, R. W., and Balch, M., 'Efficient sampling for non-intrusive polynomial chaos applications with multiple input uncertain variables,' in '48th AIAA/ASME/ASCE/AHS/ASC Structures, Structural Dynamics, and Materials conference, Structures, Structural Dynamics, and Materials and Co-located conferences,' American Institute of Aeronautics and Astronautics, Honolulu, Hawaii, April 2007 doi:10.2514/6.2007-1939.

[45] Sudret, B., 'Global sensitivity analysis using polynomial chaos expansion,' Reliability Engineering and System Safety, 2008, **93**(7), pp. 964–979, doi: 10.1016/j.ress.2007.04.002.

[46] Crestaux, T., Maitre, O. L., and Martinez, J.-M., 'Polynomial chaos expansion for sensitivity analysis,' Reliability Engineering and System Safety, 2009, **41**(4), pp. 1161–1172, doi:10.1016/j.ress.2008.10.008.

[47] Ghaffari, S., Magin, T., and Iaccarino, G., 'Uncertainty quantification of radiative heat flux modeling for titan atmospheric entry,' in '48th AIAA Aerospace Sciences Meeting Including the New Horizons Forum and Aerospace Exposition, Aerospace Sciences Meetings,' American Institute of Aeronautics and Astronautics, Orlando, Florida, January 2010 doi:10.2514/6.2010-239.

[48] Erb, A. and Hosder, S., 'Uncertainty analysis of turbulence model closure coefficients for wall-bounded attached and separated flows,' in '19th AIAA Non-Deterministic Approaches conference, AIAA SciTech Forum,' American Institute of Aeronautics and Astronautics, Grapevine, Texas, June 2017 doi:10.2514/6.2017-1952.

[49] Erb, A. and Hosder, S., 'Uncertainty analysis of turbulence model closure coefficients for shock wave-boundary layer interaction simulations,' in '2018 AIAA Aerospace Sciences Meeting, AIAA SciTech Forum,' American Institute of Aeronautics and Astronautics, Kissimmee, Florida, January, 2018 doi:10.2514/6.2018-2077.

[50] Erb, A. and Hosder, S., 'Investigation of turbulence model uncertainty for supersonic/hypersonic shock wave-boundary layer interaction predictions,' in '22nd AIAA International Space Planes and Hypersonics Systems and Technologies Conference, AIAA SPACE Forum,' American Institute of Aeronautics and Astronautics, Orlando, FL, September 2018 doi:10.2514/6.2018-5195.

[51] Georgiadis, N. J. and Yoder, D. A., 'Recalibration of the shear stress transport model to improve calculation of shock separated flows,' in '51st AIAA Aerospace Sciences Meeting including the New Horizons Forum and Aerospace Exposition, Aerospace Sciences Meetings,' American Institute of Aeronautics and Astronautics, Grapevine (Dallas/Ft. Worth Region), Texas, January 2013 doi:10.2514/6.2013-685.

[52] Anderson, J., *Hypersonic and High-Temperature Gas Dynamics*, AIAA, Reston, VA, 2 edition, 2006.

[53] Tan, J. and Jin, J., 'Stress limiter consideration for k-omega turbulence models in shock wave/turbulent boundary-layer interactions in supersonic and hypersonic flows,' in '20th AIAA Computational Fluid Dynamics Conference, Fluid Dynamics and Co-located Conferences,' American Institute of Aeronautics and Astronautics, Honolulu, Hawaii, 2011 doi:10.2514/6.2011-3980.

VITA

Aaron Erb grew up in Edwardsville, Illinois. With the encouragement of family, friends, and co-workers, he enrolled in Lewis and Clark Community College in 2007. After graduating with an associates degree in Engineering Science in 2009, Aaron continued his undergraduate education at the Missouri University of Science and Technology. In 2012, Aaron graduated Summa Cum Laude earning a Bachelor of Science in Aerospace Engineering. Aaron continued his education at the Missouri University of Science and Technology as a Chancellor's Fellow where he earned his Doctor of Philosophy in Aerospace Engineering in May 2021. Throughout his graduate career, Aaron had the opportunity to intern at the NASA Langley Research Center where he obtained a Pathways position. After graduation, Aaron continued to work at NASA Langley Research Center in the Vehicle Analysis Branch of the Systems Analysis and Concepts Directorate.